THE RANGE OF HEAVY IONS IN SOLID MATERIALS

Thesis by

R. Darden Powers

In Partial Fulfillment of the Requirements

For the Degree of

Doctor of Philosophy

California Institute of Technology

Pasadena, California

1962

ACKNOWLEDGMENTS

The author would like to thank all the staff members of the Kellogg Radiation Laboratory for their aid and assistance throughout the work of this experiment. In particular, heartfelt appreciation is extended to Professor Ward Whaling, whose indispensable encouragement, patience, assistance, and supervision is acknowledged in no small way.

Thanks are extended to Professors Whaling, R. F. Christy, and T. Lauritsen for kindly reading all or part of this thesis prior to its inclusion in final form. I would also like to thank Dr. Jack Overley for supplying the boron targets, Dr. Thomas Noonan for several discussions on the theoretical aspects of this thesis, and Professor J. Lindhard for furnishing his unpublished data on the theory.

ABSTRACT

The range of Xe, Kr, A, Ne, and N ions in Al, Be, B, and C has been investigated for incident ion energy in the region 50-500 kev. A monoenergetic ion beam accelerated in an electrostatic accelerator strikes a thick target of the stopping material, and the penetration depth of the ions beneath the surface is determined by a momentum analysis of monoenergetic protons elastically scattered from the target and embedded atoms. A linear range-energy behavior is observed for Xe, Kr, and A ions, but dE/dR increases with ion energy for N and Ne ions. The range-energy expression of Nielsen based upon elastic nuclear collisions predicts a constant dE/dR for Xe and Kr ions which is 20 to 28 per cent above the experimental values. A more recent theory by Lindhard and Scharff which includes electron excitation of the stopping atoms fits the Xe in Be, Kr in Be, and Kr in Al experimental data to within $(^{+13}_{-7})$ per cent, but is systematically higher than the Xe in Al values by +35 per cent at 50 kev down to +2 per cent at 500 kev. For A, Ne, and N ions, where the low velocity elastic nuclear collision theory is not applicable, the Lindhard-Scharff predictions are from 0 to +15 per cent above the experimental values.

TABLE OF CONTENTS

I. INTRODUCTION

The range of heavy ions in solid materials at very low ion velocities is of interest in the understanding of radiation damage, in nuclear recoil measurements, and in experiments utilizing heavy ion accelerators. Because of the extremely small penetration depths involved ($\lesssim 10^{-4}$ cm. in solids), suitable techniques for measuring such ranges have only recently been developed.

An article by Nielsen (Nielsen, 1956) suggested a method for measuring ranges in solids in the kev energy region by elastically scattering protons or deuterons from a target blank which previously had been bombarded by the heavy ions. The method is particularly suited to this laboratory since elastic scattering techniques for measuring target composition have been extensively developed here. (Snyder, 1950; Brown, 1951; Wenzel, 1952; Bardin, 1961).

N. Bohr (Bohr, 1948) had previously laid the groundwork for a theoretical description of the stopping of heavy ions at low velocities. In 1956 Nielsen re-examined the problem and obtained a range-energy expression numerically 2/3 as large, but identical in charge and mass dependence, as Bohr's expression when the ion mass is much greater than the target atom mass.

In seeking experimental results with which to compare his theoretical predictions, Nielsen could find only a few indirect measurements. These were measurements by Mileikowsky (Mileikowsky, 1954) and Thulin (Thulin, 1955) of the straggling of heavy ions. These authors analyzed by elastic scattering and (p,α) reactions the distribution of ions embedded in targets prepared in the Stockholm

isotope separator, from which ions strike the collecting target with 45 kev of energy. These authors did not measure the depth of penetration because of uncertainties as to the condition of the target surface. Rather they measured the width of the distribution of the embedded ions due to straggling. Bohr's theory relates the width of the distribution with the depth of penetration; by using this relation Nielsen obtained ranges from the measurements of Mileikowsky and Thulin which fit the Nielsen prediction within 20 per cent. These range values, the only ones available prior to this experiment, did not provide a systematic test of the charge, mass, or energy dependence of the range-energy expression, and it was with the purpose of obtaining better experimental information that this experiment was undertaken.

The method employed in the present experiment was suggested by Nielsen's paper, but it is distinctly different in that both range and range straggling are measured independently. The method has been examined with some care and the method itself constitutes an original disclosure of this thesis as well as the range measurements obtained with it. A method similar to the one employed here, utilizing (p,γ) reactions instead of elastic scattering to detect the embedded ions, has since been reported by two groups independently: Guseva, et al. (Guseva, 1959), and Porat and Ramavataram (Porat, 1960).

Theoretical analysis of the stopping of very low velocity ions has also progressed while this experiment was under way. Lindhard and Scharff have recently furnished us a paper, prior to

publication, in which they analyze the energy loss due to elastic nuclear scattering in a manner similar to that employed by Bohr and Nielsen except that the Thomas-Fermi interaction potential is integrated numerically, whereas Bohr and Nielsen approximate the interaction potential with an expression varying as r^{-2} to obtain an integral in closed form. Lindhard and Scharff also include an additional electronic contribution to the stopping cross section which is not negligible at low velocities and which must be included in order to achieve agreement with our experimental results.

II. THEORY

II.A. Introduction.

The passage of an atom through matter involves complicated many-body interactions between the moving nucleus and its bound electrons with the nuclei and electrons of the stopping material. This formidable problem may be adequately represented by simpler approximations in certain particular cases of practical interest:

(a). In the limit of high velocity of the moving particle, all of its electrons are stripped away. Several theoretical studies (Bohr, 1913; Bethe, 1930; Bloch, 1933) of the motion of a charged particle through matter have shown that it loses its energy predominantly by inelastic encounters which excite or ionize the atoms along its path. Although these theories require an empirical constant to allow for the complexity of the electron binding in the stopping atoms, they nevertheless provide valuable insight into the stopping process. In particular, they show that as the moving particle velocity decreases, the most tightly bound inner electrons of the stopping atom will no longer take part in the stopping, and as the velocity decreases further more and more electrons will be ineffective. This approximation is therefore applicable only to ions of high velocity, and the theory predicts that for the low velocity ions of this experiment, energy loss by inelastic encounters will play only a small part.

(b). Heavy ions of velocity sufficient to lose energy by the inelastic encounters mentioned above may carry with them one or more bound electrons, and repeated capture and loss of electrons will change the net charge of the moving ion rapidly. There is no

satisfactory theory of the energy loss process in this velocity region. Knipp and Teller (Knipp, 1941) have assumed that the energy loss is still predominantly through excitation and ionization of the stopping medium, and they compute an average charge for the moving ion which they substitute in the expressions applicable to high velocity ions. Although their results fit experimental measurements surprisingly well (Northcliffe, 1960; Heckman, 1960), their theory is clearly inapplicable to atoms which are neutral for any significant fraction of the time, and their neglect of any energy loss in excitation or ionization of the moving ion is disturbing.

(c). At very low velocities, the ion will be unable to excite even the most loosely bound electrons in the stopping material, and it is at these same low velocities that the moving atom will finally acquire its full complement of electrons. The stopping process now takes place through an elastic encounter between the moving atom and the atoms in the stopping material. If the interaction can be represented by a simple two-body potential, one may calculate the rate of energy loss of the moving atom.

This section of the thesis discusses the theory applicable to the velocity region (c) above. Our discussion necessarily leans heavily on Bohr's 1948 paper--very little new has been said on this subject since then; the differences between Bohr's results and the theoretical treatment contained herein are discussed in Section II. G below. The calculations to follow are based on a classical orbit picture, the use of which is justified in Section II. B. Section II. C contains a formal derivation of the expression for dE/dR in terms

of an arbitrary interaction potential. In II. D an approximation to the screened potential is introduced to permit evaluation of an expression for dE/dR. Range and range straggling are discussed in Section II. E. Section II. F deals with the true path length in terms of the projected path length. Section II. H discusses the expected range-energy behavior outside the velocity region (c) above.

II. B. Interaction Potential. Limits of Applicability of a Classical Argument.

We consider the interaction between an atomic particle and the matter through which it penetrates. The incident particle has mass M_1, nuclear charge $e_1 = Z_1\epsilon$, initial velocity v_L, and initial energy E_L. The atoms of which the matter is composed have mass M_0, nuclear charge $e_0 = Z_0\epsilon$, and zero initial energy. In the center of mass system the problem is equivalent to that of a single particle of mass

$$M_r = \frac{M_0 M_1}{M_0 + M_1} \tag{1}$$

at a distance r from a fixed center of force. To represent the electrostatic potential in the vicinity of an atom of atomic number Z, we follow Bohr (Bohr, 1948, p. 19) in using $\frac{V(R)}{\epsilon} = Z\epsilon\, e^{-R/a} R^{-1}$ where a is the "screening parameter". The screening parameter is obtained from the Thomas-Fermi statistical model (Schiff, 1955) and has the form $a = a_B/Z^{1/3}$ where a_B is the Bohr radius $\hbar^2/\mu\epsilon^2$ of the hydrogen atom.

The total screening effect for the heavy atoms we are concerned with depends upon the presence of the electrons in the incident atom as well as in the stopping atom. We take the charge distribution for

the incident atom to be $Z_1\epsilon \exp(-R_1 Z_1^{1/3}/a_B)/R_1$, the charge distribution for the stopping atom to be $Z_0\epsilon \exp(-R_0 Z_0^{1/3}/a_B)/R_0$, and take the relative separation of the atoms to be r. It is shown in APPENDIX I that the energy of interaction between these atoms is

$$V(r) = \frac{Z_0 Z_1 \epsilon^2}{r} \frac{(Z_0^{2/3} \cdot e^{-rZ_0^{1/3}/a_B} - Z_1^{2/3} \cdot e^{-rZ_1^{1/3}/a_B})}{(Z_0^{2/3} - Z_1^{2/3})} . \quad (2)$$

By expanding the exponentials in this expression, we readily see that V(r) does not greatly differ from the approximate expression

$$V_a(r) = \frac{Z_0 Z_1 \epsilon^2 e^{-r/a}}{r} \quad (3)$$

where

$$a = a_B / \sqrt{Z_0^{2/3} + Z_1^{2/3}} . \quad (4)$$

The rather simple expression of equation 3 for the potential energy of interaction between the atoms differs from the ordinary Coulomb interaction only by the presence of the screening factor exp(-r/a).

A classical orbit approximation will be used in the following calculations and it is appropriate before going further to justify the use of this classical approximation. It is first convenient to introduce the de Broglie wave length $\lambda\!\!\!^{-}$ of the moving particle and also the Coulomb "collision diameter" b:

$$\lambda\!\!\!^{-} = \hbar/M_r v_L \qquad \text{and} \qquad b = 2Z_0 Z_1 \epsilon^2 / M_r v_L^2 . \quad (5)$$

Bohr (Bohr, 1948, pp. 27, 18) then defines the following criteria for the approximate validity of classical orbit calculations in scattering

problems:

(1). $\chi \ll b$. In the experiments described in this thesis b/χ varies between 10^2 and 10^4 so that this condition is always satisfied.

(2). The potential must be relatively constant over the dimensions of the wave packet representing the particle. The scale of the variation of the potential in equation 3 is a, hence χ must be much smaller than a: $\chi/a \ll 1$. The quantity χ/a is proportional to $1/v_L$ and for any energy greater than 0.25 ev, $\chi/a < 1$. Bohr emphasizes the fact that for the screened Coulomb potential small angle scattering through angles less than χ/a cannot be represented by the orbit approximation.

II. C. Stopping Power and Energy Straggling.

As a first step toward obtaining the range and range straggling, we would like to obtain general expressions for the total energy lost, and for the mean square deviation of the energy lost, in a section ΔR of the total path R. These expressions can then be integrated to find the range and range straggling. We begin by letting n_i be the number of collisions in path length ΔR in which an energy between T_i and $T_i + \Delta T_i$ is transferred to the stopping atom. n_i is distributed around its mean value ω_i, according to the Poisson law $P(n_i) = (\omega_i^{n_i} e^{-\omega_i})/n_i!$, which applies to any problem involving random processes depending on a large number of trials, the probability of occurrence of the process being small and constant. The trials are the collisions with the atoms along a path length ΔR which is long compared with atomic dimensions. The total energy lost by the particle in ΔR is the sum over all energy transfers, or $\Delta E = \sum_i T_i n_i$. The average value of ΔE will be given by

$$\overline{\Delta E} = \sum_i T_i \omega_i \quad . \tag{6}$$

For the mean square deviation of ΔE we have

$$\Omega^2(\Delta E) = \overline{(\Delta E - \overline{\Delta E})^2} = \sum_i T_i^2 \overline{(n_i - \omega_i)^2} = \sum_i T_i^2 \omega_i \quad , \tag{7}$$

since, for the Poisson distribution, $\overline{(n_i-\omega_i)^2} = \sum_{n_i=0}^{\infty} (n_i-\omega_i)^2(\omega_i^{n_i} e^{-\omega_i})/n_i!$ $= \omega_i$, and the cross terms average to zero. We now introduce $\omega_i = N\Delta R d\sigma_i$, where N is the number of stopping atoms/cm^3 and $d\sigma_i$ is the classical differential cross section for an energy transfer between T_i and $T_i + \Delta T_i$. Upon passing to the limit of very small energy intervals, ΔT_i, we obtain for the average energy lost in ΔR

$$\overline{\Delta E} = N\Delta R \int T d\sigma \tag{8}$$

and for the mean square energy deviation

$$\Omega^2(\Delta E) = N\Delta R \int T^2 d\sigma \ . \tag{9}$$

The energy T imparted to the stopping atom is determined from the kinematics of the motion. The differential scattering cross section is $d\sigma = 2\pi p dp$, where p is the impact parameter at which the moving particle loses energy T. The impact parameter is defined as the perpendicular distance between the force center and the initial velocity vector.

To find T, refer to fig. 1, which illustrates the determination of the laboratory velocities $\vec{v}_1$ and $\vec{v}_0$ after the collision from the center of mass velocity $\vec{v}_c = M_1 \vec{v}_{1L}/(M_1+M_0)$. It is easy to see that $y = v_0 \sin\psi = v_0 \sin[(\pi-\theta_c)/2] = v_c \sin\theta_c$. Consequently, $v_0 = 2v_c \sin(\theta_c/2)$, and as a result,

$$T = \tfrac{1}{2}M_0 v_0^2 = \tfrac{1}{2}\frac{M_0 4M_1^2 v_{1L}^2}{(M_1 + M_0)^2} \cdot \sin^2(\theta_c/2) = T_m \sin^2(\theta_c/2) \qquad (10)$$

where $$T_m = 4 M_1 M_0 E_L/(M_1+M_0)^2 \qquad (11)$$

is the maximum energy lost by the incident atom in a single encounter.

The integral in equation 8 can be evaluated if $T = T(\theta_c)$ can be expressed as a function of p. The formal solution (Massey, 1952) for the scattering angle θ_c between the asymptotes of the orbit of motion expressed as a function of p is

$$\theta_c = \pi - 2\int_0^{u_0=1/r_{min}} \frac{pdu}{\sqrt{1 - V(u)\cdot(M_0+M_1)/(M_0E_L) - p^2u^2}} , \qquad (12)$$

where $u = 1/r$ is the reciprocal of the relative separation r, V(u) is the repulsive interaction potential energy, and $u_0 = 1/r_{min}$ corresponds to the turning point in the orbit and is determined from

$$p^2/r_{min}^2 = 1 - V(r_{min})/[M_0E_L/(M_0 + M_1)] . \qquad (13)$$

Equations 10 and 12 determine T as a function of p which can be substituted in equations 8 and 9 to yield formal expressions for $\Delta E/\Delta R$ and $\Omega^2(\Delta E)$.

II. D. Approximate Interaction Potential.

The integral in equation 12 cannot be evaluated in closed form for the interaction energy $V(r) = V_a(r)$ given by equation 3. We follow Bohr in approximating $V_a(r)$ with an nth power repulsive potential energy of the form

$$V_n(r) = k_n/r^n. \qquad (14)$$

At a distance R from the center, $V_a(r)$ and $V_n(r)$ can be made to vary in the same manner by equating the logarithmic derivatives of the two functions at R to obtain

$$n = 1 + R/a \quad \text{and} \quad k_n = Z_0 Z_1 \epsilon^2 a^{n-1} [(n-1)/e]^{n-1} , \tag{15}$$

where e is the base of the natural logarithmic system. It is seen that for $R \ll a$, we have an ordinary Coulomb field, while for $R \gtrsim a$, the increased influence of the screening implies a field of the form given in equation 14 with increasing values of n.

The principal contribution to the integral in equation 12 comes from values of r in the neighborhood of r_{min}. One therefore seeks to match V_n and V_a in the neighborhood of $r = r_{min}$. Matching the potential V_n and V_a at R = a yields $V_n = k_2 r^{-2}$, which can be integrated in closed form, and which should give a good approximation to the scattering of particles for which $r_{min} \approx a$. The ratio r_{min}/a depends on p as well as on E. Let $r'_{min} = r_{min}$ for p = 0, the minimum distance of closest approach in head-on collisions. The ratio r'_{min}/a varies from ~0.1 (for 500-kev A ions or 50-kev N and Ne ions) to ~3 (for 10-kev Xe ions in Be and Al). Nielsen (Nielsen, 1956) has proposed that a potential of the form $V = k_2 r^{-2}$ should be a sufficiently good approximation provided that $0.5 < r'_{min}/a < 2$. If we adhere rigorously to these limits on r'_{min}/a, and further demand, for example, that 90 per cent of the stopping process occur within these limits, then we find that the approximate potential $k_2 r^{-2}$ should apply only to the following region of our measurements:

Xe in Al and Be	300--500 kev
Kr in Al and Be	100--500 kev
A in Be, B, and C	0-- 50 kev

None of our measurements with N and Ne ions fall within these limits on r'_{min}/a.

We now proceed to solve equation 12 for an interaction potential of the form given by equation 14 with n = 2. The upper limit, $u_0=1/r_{min}$, on the integral is readily seen from equation 13 to be $1/r_{min} = [p^2 + k_2(M_0+M_1)/(M_0E_L)]^{-\frac{1}{2}}$. With this upper limit in mind, then, the integration is quite easily performed with the result that

$$\theta_c(p) = \pi \left[1 - \frac{1}{[1 + k_2(M_0+M_1)/(p^2M_0E_L)]^{\frac{1}{2}}}\right] . \qquad (16)$$

Solving this equation in turn for the impact parameter p in terms of the scattering angle θ_c yields

$$p^2 = p_c^2 [\pi^2/(2\pi\theta_c - \theta_c^2) - 1] , \qquad (17)$$

where $$p_c^2 = k_2(M_0 + M_1)/(M_0E_L) = 2Z_1Z_0\epsilon^2a/M_rv_L^2e = ba/e, \qquad (18)$$

by use of equations 5 and 15. Since the classical differential scattering cross section is $d\sigma = 2\pi pdp$, direct substitution of equations 10, 16, and 18 into equation 8 yields the following:

$$\overline{\Delta E}/\Delta R = NT_m \int_{p=0}^{p=\infty} \sin^2(\theta_c/2)2\pi pdp = 2\pi NT_m \int_{p=0}^{p=\infty} pdp \cdot \cos^2[\pi/(2\sqrt{1+p_c^2/p^2})] . \qquad (19)$$

The result of the integration, the details of which are given in APPENDIX II, is

$$\overline{\Delta E}/\Delta R = \frac{N T_m \pi^2 p_c^2}{4} \left[-4/\pi + 2Si(\pi) - Si(2\pi) \right] , \tag{20}$$

where

$$Si(x) = \int_0^x \frac{\sin x}{x} \, dx \ . \tag{21}$$

Evaluating the sine integrals (Jahnke and Emde, 1945) and substituting for T_m and p_c^2 by use of equations 11, 5, and 18 we obtain

$$\frac{\overline{\Delta E}}{\Delta R} = N \frac{M_1}{M_0 + M_1} Z_0 Z_1 \epsilon^2 \frac{a}{e} \pi^2 (.9968) \ . \tag{22}$$

It is interesting to note that this expression is independent of the particle energy.

In order to compute the energy straggling, we substitute equations 10, 16, and 18 into equation 9 to obtain

$$\Omega^2(\Delta E) = N \Delta R T_m^2 \int_{p=0}^{p=\infty} \sin^4(\theta_c/2) 2\pi p dp = 2\pi T_m^2 N \Delta R \int_{p=0}^{p=\infty} p dp \cdot \cos^4 \left[\pi / \left(2\sqrt{1 + p_c^2/p^2}\right) \right] . \tag{23}$$

The result of the integration, the details of which are also given in APPENDIX II is

$$\begin{aligned} \Omega^2(\Delta E) &= \frac{\pi^2 N p_c^2 T_m^2 \Delta R}{4} \left[-4/\pi + 2Si(\pi) - 2Si(2\pi) + \tfrac{1}{2} Si(4\pi) \right] \\ &= \frac{\pi^2 N p_c^2 T_m^2 \Delta R}{4} (.3145) \equiv P_\nu \Delta R , \end{aligned} \tag{24}$$

where the sine integrals have been evaluated and lumped together into the numerical constant (.3145). Equation 24 gives the mean square deviation of the energy ΔE which is lost in the path length ΔR.

II.E. Range and Range Straggling.

The expression for $\Delta E/\Delta R$ in equation 22 is independent of energy and can be integrated directly to obtain for the total range

$$R(cm) = \frac{(M_0 + M_1)}{N M_1} \frac{\sqrt{Z_0^{2/3} + Z_1^{2/3}}}{Z_0 Z_1} \frac{e}{\pi^2 (.9968)} \frac{E_L}{\epsilon^2 a_B}, \qquad (25)$$

where the screening parameter given by equation 4 has been included. We obtain the final expression for the range by using the fact that $N = N_0 \rho_0 / M_0$, where ρ_0 is the target density, and by collecting the various numerical factors into a single constant as follows:

$$t(\mu gm/cm^2) \equiv R\rho_0 \times 10^6 = 0.602 \frac{\sqrt{Z_0^{2/3} + Z_1^{2/3}}}{Z_0 Z_1} \frac{M_0 (M_0 + M_1)}{M_1} E_L(kev). \qquad (26)$$

The fluctuation in ΔE which is specified by the mean square energy deviation $\Omega^2(\Delta E)$ in equation 24, will give rise to a Gaussian distribution of the values of ΔR corresponding to a fixed amount of energy loss ΔE with a mean square deviation (Bohr, 1948, p. 127) given by

$$\Omega^2(\Delta R) = \Omega^2(\Delta E) \left(\frac{\Delta R}{\Delta E}\right)^2 = \left(\frac{\Delta R}{\Delta E}\right)^2 P_\nu \frac{\Delta R}{\Delta E} \Delta E = \frac{P_\nu \Delta E}{(\Delta E / \Delta R)^3} \qquad (27)$$

where use has been made of equation 24. Upon integrating equation 27 over the entire energy range, therefore, we obtain the straggling in the total range, viz.,

$$\Omega^2(R) = \int_0^{E_L} \Omega^2(\Delta R) = \int_0^{E_L} \frac{P_\nu dE}{(dE/dR)^3} . \qquad (28)$$

Since $dE/dR = \frac{N M_1}{M_0 + M_1} \frac{Z_1 Z_0}{\sqrt{Z_0^{2/3} + Z_1^{2/3}}} \frac{\pi^2 (.9968)}{e} \epsilon^2 a_B = K$, a constant which is independent of energy, we obtain with the help of equations 11, 18, and 24

$$\Omega^2(R) = \frac{P_\nu}{E_L}\frac{1}{K^3}\int_0^{E_L=KR} E dE = \frac{1}{2}\frac{P_\nu}{E_L}\frac{R^2}{K} \quad ,$$

which is readily simplified to

$$\frac{\Omega^2(R)}{R^2} = 2\frac{(0.3145)}{(0.9968)}\frac{M_0 M_1}{(M_0+M_1)^2} \approx \frac{2}{3}\frac{M_0 M_1}{(M_0+M_1)^2} \quad , \qquad (29)$$

with the aid of equations 11, 18, 22, and 24.

II.F. True Path Length in Terms of Projected Path Length.

The true path length R can be expressed in terms of the projected path length R_p by the following relation (Bichsel, 1957):

$$R - R_p = \frac{1}{2}\sum_i \ell_i \Theta_i^2 \qquad (30)$$

where ℓ_i is the distance between the ith and (i + 1)th small angle collision, and Θ_i is the net accumulated angle between the initial beam axis and the particle velocity vector prior to the (i+1)th collision. Equation 30 can also be expressed in integral form

$$R - R_p = \frac{1}{2}\int_0^R \overline{\Theta^2(\ell)}\, d\ell, \qquad (31)$$

where $\overline{\Theta^2(\ell)}$, the mean square deviation in angle from the initial beam axis at a distance ℓ along the true path, is given by Fermi (Fermi, 1950):

$$\overline{\Theta^2(\ell)} = n(\ell)\,\overline{\theta_L^2} = \frac{n(\ell)\int_0^\ell d\ell N \int_0^{p_{max}\to\infty} \theta_L^2(p) 2\pi p dp}{n(\ell)} \quad . \qquad (32)$$

θ_L is the laboratory angle between collisions, $n(\ell)$ is the average number of collisions suffered by the moving atom in a distance ℓ along the

path, N is the number of stopping atoms/cm^3, and p is the impact parameter.

The laboratory scattering angle θ_L is expressed in terms of the center of mass scattering angle θ_c by the relation

$$\cot \theta_L = \frac{M_1}{M_0} \csc \theta_c + \cot \theta_c \ ,$$

which for $M_1 >> M_0$ becomes:

$$\theta_L \approx \frac{M_0}{M_1} \sin \theta_c \ . \tag{33}$$

Substituting equation 16 into 33 and the result into equation 32 yields

$$\overline{\Theta^2(\ell)} = 2\pi N \left(\frac{M_0}{M_1}\right)^2 \int_0^{\ell} d\ell \int_0^{p_{max} \to \infty} \sin^2 \frac{\pi}{\sqrt{1 + p_c^2/p^2}} \, pdp. \tag{34}$$

The second integral is readily evaluated along the lines of APPENDIX II, so that equation 34 becomes

$$\overline{\Theta^2(\ell)} = 2\pi N \left(\frac{M_0}{M_1}\right)^2 \int_0^{\ell} d\ell \left[\frac{\pi p_c^2}{4} \left(2 \, Si(2\pi) - Si(4\pi)\right)\right]$$

$$= \frac{\pi^2}{2} N(1.373) \left(\frac{M_0}{M_1}\right)^2 \int_0^{\ell} d\ell \, p_c^2$$

$$= \frac{\pi^2}{2} N(1.373) \left(\frac{M_0}{M_1}\right)^2 \int_{E_i(\ell=0)}^{E(\ell)} - \frac{dE}{(dE/d\ell)} \, k_2 \frac{(M_0+M_1)}{EM_0} \ ,$$

where the sine integrals have been evaluated and equation 18 has been used. E_i is the initial energy with which the ion strikes the target, and E is the energy of the ion at a distance ℓ beneath the surface. Therefore

$$\overline{\theta^2(\ell)} = \frac{-\pi^2}{2} \frac{N(1.373)}{(dE/d\ell)} \left(\frac{M_0}{M_1}\right)^2 \frac{k_2(M_0+M_1)}{M_0} \ln \frac{E}{E_i} \quad . \tag{35}$$

Substituting equation 35 into equation 31 we obtain

$$R - R_p = \frac{-\pi^2}{4} \frac{N(1.373)}{(dE/d\ell)} \left(\frac{M_0}{M_1}\right)^2 \frac{k_2(M_0+M_1)}{M_0} \int_{E_i(\ell=0)}^{E_f(\ell\to R)} \frac{-dE}{(dE/d\ell)} \ln \frac{E}{E_i}$$

$$= \frac{+\pi^2}{4} \frac{N(1.373)}{(dE/d\ell)^2} \left(\frac{M_0}{M_1}\right)^2 \frac{k_2(M_0+M_1)}{M_0} E_i \left[x \ln x - x\right]_{x=1}^{x=E_f/E_i \to 0}$$

$$= \frac{\pi^2}{4} \frac{N(1.373)}{(dE/d\ell)} \left(\frac{M_0}{M_1}\right)^2 \frac{k_2(M_0+M_1)}{M_0} R,$$

since $E_i/(dE/d\ell) = R$ and $x \ln x \to 0$ as $x \to 0$. Upon substituting for $dE/d\ell$ from equation 22 and k_2 from equation 15 we obtain for $M_1 >> M_0$:

$$R - R_p = \frac{1.373}{4(0.9968)} \frac{M_0}{M_1} R = \frac{1}{2.904} \frac{M_0}{M_1} R \ ,$$

$$\text{or} \quad \frac{R}{R_p} = 1 + \frac{1}{2.904} \frac{M_0}{M_1} \ , \quad M_1 >> M_0. \tag{36}$$

II. G. Comparison with Other Theoretical Analyses.

Bohr and his collaborators, Nielsen, Lindhard, and Scharff, have previously analyzed the energy loss by elastic scattering. Our equation 26 for the range is identical with that obtained by Nielsen (Nielsen, 1956). Lindhard and Scharff (Lindhard, 1961a) derive an expression for $(\Delta E/N\Delta R)$ which agrees with our expression 22 except for the constant (.9968), which is 1.0 in their expression. Bohr (Bohr, 1948; p. 139) derives an expression for dE/dR in the limit of $M_1/M_0 >> 1$ and $Z_1/Z_0 >> 1$

$$dE/dR \sim \pi N a_B Z_1^{2/3} Z_0 \epsilon^2$$

while our equation 22 yields, in the same limits,

$$dE/dR = \pi N a_B Z_1^{2/3} Z_0 \epsilon^2 (0.9968\ \pi/e) .$$

Bohr's expression for dE/dR above is based on an isotropic scattering approximation, $d\sigma = (\sigma/4\pi)d\omega$, where $\sigma = \pi p_c^2$. Repeating his calculation we find, again in the same limits

$$dE/dR = \pi N a_B Z_1^{2/3} Z_0 \epsilon^2 \cdot 2/e.$$

The isotropic scattering approximation thus yields a value of dE/dR about 2/3 the value obtained by using $d\sigma$ from equation 16 or 17.

The expression for $\Omega^2(R)/R^2$ given by Bohr (Bohr, 1948; p. 140) is also based on the isotropic scattering model and is exactly a factor 2 greater than expression 29 above. If $M_1 >> M_0$, it is seen from equation 11 that the particles can lose only a very small fraction of their energy in a single collision and, as a result, the values of ΔE, corresponding to a section of the range for which the average number of collisions is large, will be distributed according to the normal law of error. If $M_1 \tilde{<} M_0$, the incident particle will in almost every collision suffer a large deflection and the stopping and straggling will thereby be overshadowed by diffusion effects. Consequently, when this latter condition applies, the distribution may then deviate markedly from a Gaussian law. Bohr therefore considers only $M_1 >> M_0$ and uses for the range straggling

$$\Omega^2(R)/R^2 \approx (4/3)\cdot(M_0/M_1). \qquad (37)$$

Nielsen quotes this same expression, but Lindhard and Scharff (Lindhard, 1961a) use the same expression as our equation 29. For those cases where $M_1 >> M_0$ and where the theory as we have developed

it is applicable, we thereby expect the range to be distributed according to the normal law of error

$$W_0(R) = [1/(\sqrt{2\pi}\ \Omega_0)] \cdot e^{-(R-R_0)^2/2\Omega_0^2}, \qquad (38)$$

with most probable range R_0 given by equation 25 (or 26) and the standard deviation Ω_0 given by equation 29.

Lindhard and Scharff (Lindhard, 1961a) also make a more exact calculation of the range as a function of energy by using the potential energy $V(r) = Z_1 Z_0 \epsilon^2 \varphi_0(r/a)/r$, where $\varphi_0(r/a)$ is the Fermi function of a neutral atom. The result of their numerical integration gives a range-energy dependence fairly close to that predicted by our equation 26. Their curve predicts a greater range for the following energy region:

Xe in Be and Al:	0--~85 kev
Kr in Be and Al:	0--~35 kev
A in Be:	0--~ 5 kev

with the maximum discrepancy being ~ 30 per cent at roughly one-third the maximum energies listed. For higher energies than those listed, their curve predicts a smaller range with the maximum discrepancy being 12 per cent at 150 kev Kr in Be or 400 kev Xe in Be. The difference between Lindhard and Scharff's range-energy relation and that predicted by equation 26 may be seen in figures 11-18 in which the solid curve is given by equation 26 and the Lindhard-Scharff expression is plotted as a dotted curve.

Lindhard and Scharff (Lindhard, 1961a) have worked out the following expression based on a r^{-2} type potential for the projected path

length in terms of the true path length:

$$\frac{\bar{R}}{\bar{R}_p} = \frac{1}{4}\left[-1 - 3M_0/M_1 + (5 + M_0/M_1)\frac{1+M_0/M_1}{2\sqrt{M_0/M_1}} \cdot \arccos\frac{1-M_0/M_1}{1+M_0/M_1}\right] \quad (39)$$

$$\approx 1 + M_0/(3M_1).$$

Their result $\bar{R}/\bar{R}_p \approx (1 + M_0/3M_1)$ agrees quite well with our value in equation 36.

Lindhard and Scharff also make the statement that as far as the range straggling is concerned

$$\overline{\Omega^2(R_p)} \approx \overline{\Omega^2(R)}. \quad (40)$$

II.H. Expected Range-Energy Behavior For Velocities Outside the Region of Our Approximation.

We have listed in Section II.D the energy regions over which we expect the theory based on a $k_2 r^{-2}$ potential to be valid. For velocities which are larger than the velocities of this region the screening effects become negligible; therefore, the energy loss, $\Delta E/\Delta R$, due to nuclear collisions will have a different energy dependence which can readily be found. It is well known (Bohr, 1948, p. 6) that the relative scattering angle θ_c between the asymptotes of the hyperbolic orbit of motion in an ordinary Coulomb force field is

$$\tan(\theta_c/2) = b/(2p) \quad (41)$$

where b is the "collision diameter" (equation 5) and p the impact parameter. One readily obtains, then, for the Rutherford differential scattering

cross section

$$d\sigma = 2\pi p dp = (2\pi b^2/4)\cot(\theta_c/2)\csc^2(\theta_c/2)d\theta_c/2$$

$$= (2\pi b^2/8)\, d(\sin^2\theta_c/2) \,/\, (\sin^4\theta_c/2) = \pi(b^2/4)T_m(dT/T^2),$$

where use has been made of equation 10. Putting the latter expression into equation 8, one obtains for the stopping due to nuclear collisions in an unscreened Coulomb field

$$\overline{\Delta E}/\Delta R = \pi(b^2/4)NT_m \log(T_m/T_{min}) \qquad (42)$$

where T_{min} is the value of T corresponding to the limiting angle θ_{min} depending on the screening of the field. Thus, when the velocity of the incident particle is sufficiently high that screening effects are negligible, equation 42 describes the energy loss due to elastic scattering, and equation 22 is no longer applicable.

In order to determine roughly what value of θ_{min} corresponds to T_{min}, we first recognize that as long as the impact parameter p is small compared to the screening radius a, the deflection will occur essentially in the unscreened part of the field, but when $p \gtrsim a$ the screening effects are important and must be considered. Consequently, if we take p = a as the limiting impact parameter corresponding to T_{min}, we see from equation 41 that $\theta_{min} \sim b/a$, and that

$$\frac{\overline{\Delta E}}{\Delta R} = \frac{4\pi N Z_1^2 Z_0^2 \epsilon^4}{M_0 v_L^2} \log \frac{a M_r v_L^2}{Z_1 Z_0 \epsilon^2} \qquad (43)$$

where equations 5, 10, and 11 have been used. It is seen from this latter expression that $\overline{\Delta E}/\Delta R$ due to nuclear collisions decreases with increasing velocity. If the stopping were determined entirely by nuclear stopping

effects, then, we would expect the range to increase as a function of velocity for velocities where equation 43 is applicable.

It is at this point, however, that the problem becomes extremely difficult. As long as the velocity of the particle is such that the duration of the collision between the two interacting atoms is long compared to the periods of the electrons within the stopping atom or the moving atom, then the interaction potential between the particle and the electrons changes so slowly that the collision is essentially adiabatic, and no energy is lost to the electrons (Bohm, 1951). When the velocity of the particle increases to the point where the collision is no longer adiabatic, then energy will be lost due to electron excitation and ionization of the atoms along the path. Unfortunately, however, there is no adequate theory available for electron excitation and ionization of the stopping atoms by the penetrating atoms when the velocity of the penetrating atom is roughly the same order of magnitude as the velocity of the least tightly bound electrons within the stopping atoms. Seitz and Koehler (Seitz, 1956) obtain an approximate expression, $(\overline{\Delta E}/\Delta R)_e \propto v_L^2$, by assuming that the conduction electrons of the stopping material, which is assumed to be an ideal metal, are scattered isotropically by the moving atom. Their expression gives, for 500-kev argon atoms in beryllium, the same order of magnitude for $(\overline{\Delta E}/\Delta R)_e$ as does expression 43 for the elastic collisions at the same velocity. Fermi and Teller (Fermi, 1947) obtain an expression for the interaction between a negative meson and the electrons of a degenerate electron gas in the velocity region of interest to us. Presumably their expression would not be applicable to the case with which we are concerned because the interaction cross section between a meson and an electron would be expected

to differ from the interaction cross section between a neutral (or nearly neutral) atom and an electron. Another estimate is that of Lindhard and Scharff (Lindhard, 1961a) using the charge dependence of $\overline{\Delta E}/\Delta R$ based on a Thomas-Fermi treatment:

$$\frac{1}{N}\left(\frac{\Delta E}{\Delta R}\right)_e = \xi_\epsilon \frac{8\pi\epsilon^2 a_B Z_1 Z_0}{(Z_1^{2/3}+Z_0^{2/3})^{3/2}} \frac{v_L}{v_0} \tag{44}$$

where ξ_ϵ is of the order of 1--2, but may vary with Z_1 approximately as $\xi_\epsilon \approx Z_1^{1/6}$, and $v_0 = e^2/\hbar$. Equation 44 is predicted to be a first approximation valid for velocities v_L small compared to $Z_1^{2/3} v_0$. Expression 44 gives, for 500-kev argon atoms in beryllium, $\approx$ 2.5 times the value of $(\Delta E/\Delta R)$ given by equation 43 for the elastic nuclear collisions at the same velocity.

As the velocity of the moving atom continues to increase still further, however, it is known that the electronic collisions completely dominate the stopping process which can be described, for very high velocity particles, by the familiar Bethe-Bohr theory.

For velocities smaller than those velocities for which the theory of section II. D is expected to be valid, a different consideration applies. From expression 20 it is seen that $\overline{\Delta E}/\Delta R$ is proportional to $T_m \pi p_c^2$. By considering πp_c^2 to be roughly the total scattering cross section, it is seen with the aid of equations 11 and 18 that the dependence upon energy of $\overline{\Delta E}/\Delta R$ is lost in the theory of section II. D because of the presence of the factor E_L in the denominator of πp_c^2. When, as is pointed out by Bohr (Bohr, 1948, p. 49), the velocity is very low and the screening is great, the total cross section is of the same order of

magnitude as the gas kinetic cross section, which is energy independent, and $\Delta E/\Delta R$ is then proportional to the energy. Thus, a logarithmic range-energy curve would be expected at these velocities.

III. EXPERIMENTAL METHOD AND ANALYSIS OF DATA

III, A. Equipment and Vacuum Conditions. Ion Bombardment Procedure.

The method used in the experiment is very simple. It amounts to bombarding a thick smooth target with heavy ions at a predetermined energy and then using a proton beam as a probe to determine how far the ions penetrate beneath the surface of the target. The 600-kev electrostatic generator, used to accelerate the heavy ions and the protons, has been described in detail by Wenzel (Wenzel, 1952), so that only a brief description pertinent to the present experiment will be given.

The generator was fitted with four metallic gas bottles and a four-way valve so that one could manually switch from heavy ions to protons while the generator was running. The heavy ions and protons were produced in a conventional radio-frequency ion source (Moak, 1951) mounted at the upper end of the accelerating column. A strong deflecting cross-field magnet, with field perpendicular to the direction of the ion or proton beam and capable of bending 500-kev xenon ions through $\sim 3^{\circ}$, was used to select the desired singly-charged mass component of the beam after acceleration. This particular component of the beam was rendered monoenergetic by a 90° electrostatic analyzer of 30.25 inch mean radius and 1/16 inch entrance and exit slits. The analyzer was calibrated against the $F^{19}(p,\alpha\gamma)O^{16}$ resonance at 340.5 ± 0.3 kev (Bondelid, 1959).

After the target was bombarded by the heavy ions, protons were then elastically scattered from the target-plus-embedded atom configu-

ration. The scattered protons were analyzed in momentum by means of a double focusing magnetic spectrometer with the following specifications:

Mean equilibrium particle orbit	8"
Collector slit width	1/32"
Momentum resolution $P/\Delta P$	800
Scattering geometry	Incident beam horizontal, scattered beam 14.5° below horizontal

The spectrometer was calibrated against the previously calibrated electrostatic analyzer energy scale by observing the distribution of protons elastically scattered at a given angle from targets of known composition. The number of protons scattered into the spectrometer for a fixed incident charge upon the target was determined with a CsI scintillation counter.

The charge incident upon the target during the ion bombardment or the proton scattering was fixed by allowing the target current to charge a condenser to a predetermined voltage. When this voltage was reached, a trigger circuit operated relays which (1) energized a solenoid-operated beam shutter to cut off the ion or proton beam and (2) stopped the counters after each proton counting cycle.

If the proton scattering cross section is essentially Rutherford, then it is to be expected that a much greater concentration of nitrogen atoms would be required in the target because of its low atomic number than, say, xenon atoms in order to see either of these impurities in the proton scattering. It is desirable to keep the impurity concentration as small as possible, yet at the same time, have its presence distinctly

manifested in the target. Different ion beam currents and different total concentrations of charge were tried until the optimum concentrations of embedded impurity atoms were found. The actual beam currents and ion concentrations used throughout the experiment are summarized in Table I.

The time required for a suitable ion bombardment varied from one minute to two hours. At 50 kev it was extremely difficult to obtain an ion beam, and although the total charge deposited was comparatively small in the case of xenon ions, for example, the time consumed in such a bombardment varied from thirty minutes to an hour. At higher energies where better ion beams could be obtained, the time consumed was, of course, much less. The experimental procedure was to make the ion beam spot as diffuse as possible over as wide an area as possible, and then to trim the proton beam down to 1/32" x 1/32" to 3/64" x 3/64" and strike the surface previously bombarded by the ions.

The target chamber was fitted with two liquid nitrogen cold traps, one immediately surrounding the target and the other at the target chamber-diffusion pump junction, for the purpose of keeping the diffusion pump oil condensation upon the target at a minimum. Because of the large ion bombardments and also because of the occasionally large proton bombardments required to obtain sufficient data to calculate the range, the pump oil condensation on the target surface proved to be a serious factor. The condensation could have been minimized by heating the target electrically, but presumably this would have caused the embedded atoms to diffuse throughout the target, and would therefore have introduced a more serious problem than the surface contamination itself.

The electrical heating method, therefore, was not used and the data were corrected accordingly for the presence of the surface contamination.

III, B. Targets.

The targets bombarded by the heavy ions in this experiment were beryllium, carbon, aluminum, boron 10, and natural boron. The beryllium targets used throughout the experiment were made from strips of beryllium metal 1/16" x 1/4" x 6" obtained from the Beryllium Corporation of Hazleton, Pa. The manufacturer's specifications on these beryllium targets indicated a beryllium purity in excess of 98.6 per cent with the principal impurities being oxygen, aluminum, and iron. The aluminum targets used in the nitrogen ion bombardments were made from 1/16" x 3/8" strips of Ducommun aluminum alloy 6061 with aluminum purity greater than 96 per cent, and the principal impurities being iron, copper, manganese, silicon, and magnesium. The aluminum targets used in the xenon and krypton ion bombardments were made from 1/16" x 3/8" strips of Ducommun aluminum alloy EC 1100 with aluminum purity greater than 99 per cent. The carbon targets were made by machining 1/16" thick disks from a 3/8" diameter graphite spectroscopic electrode obtained from the National Carbon Company. The boron targets were obtained from J. C. Overley of this laboratory, and were made by depositing boron layers on a 25/32" diameter, 0.010" thick polished tungsten disk by the thermal decomposition of diborane (Overley, 1961).

Strips of beryllium and aluminum approximately 1 1/4" long were smoothed down with 600A silicon carbide grit paper. The strips were

then carefully washed with distilled water to insure that none of the silicon carbide grit remained on the surface of the strip, and were next polished with 2/0 grit emery polishing paper. Another washing and polishing cycle using 4/0 grit emery polishing paper followed, and the polishing process was completed by polishing the strips with a cloth saturated in red rouge polishing compound and kerosene. The targets were then washed several times in alcohol and distilled water and were examined under a microscope to insure that no surface scratches were present. The carbon disks were polished as smoothly as possible with 2/0 and 4/0 grit emery polishing paper, but it was not possible to maintain a microscopically smooth surface because of the softness of the graphite.

The target purities were checked by the elastic scattering of protons from the targets. The proton scattering was assumed to be Rutherford, and the results of the scattering are indicated in Table II.

The impurities listed in the table are in reasonable agreement with the manufacturer's specifications. The one exception was that of the aluminum alloy 6061 where the combined impurities of silicon and magnesium were listed at ~1.5 per cent by the manufacturer. These impurities were not seen in the elastic scattering momentum profiles, and if the impurities actually were present, it is felt that their effect on the range measurements would be negligible since the mass numbers of these impurities are very close to the mass number of aluminum itself.

The impurities listed in Table II are small, and consequently the effect of the impurities upon the range measurements is also small; nevertheless, the small systematic deviation introduced by these impurities was considered in all the measurements.

III, C. Method of Analyzing Experimental Data.

The procedure for surface analysis by proton scattering has been described previously by Rubin (Rubin, 1959) and by Brown, et al. (Brown, 1951). The measurements of the present experiment are concerned with the location in the target of a known impurity, and the analytical procedure for determining this location must be carried out on a slightly different basis.

The essential features of the proton scattering are illustrated in fig. 2. A monoenergetic proton beam of initial energy E_{10} enters the target at angle θ_1 with respect to the surface normal and penetrates to a perpendicular distance S beneath the surface. The protons are then elastically scattered from the target atoms and emerge from the target with energy E_{20} and at an angle θ_2 with respect to the surface normal. Since the incident proton beam loses energy at the rate $_p(\frac{dE}{dx})_1$, where $_p(\frac{dE}{dx})_1$ is a variable monotonic function of the energy along the path x, we can write the incident energy at a given distance S beneath the surface as:

$$E_{1S} = E_{10} - \int_{E_{1S}(x=S/\cos\theta_1)}^{E_{10}(x=0)} {}_p(\frac{dE}{dx})_1 \, dx . \qquad (45)$$

The protons are scattered through an angle θ_L in elastic collisions with the target nuclei. We denote by M_1 and M_0 the proton mass and target atom mass, respectively. If E_{1S} and E_{2S} are the proton energies immediately before and after the scattering, respectively, then $E_{2S} = \alpha(\theta_L, M_0, M_1)E_{1S}$, where conservation of energy and momentum re-

quires that

$$\alpha^{1/2} = \left[\frac{M_1 \cos\theta_L}{M_1+M_0} + \sqrt{\left(\frac{M_1 \cos\theta_L}{M_1+M_0}\right)^2 + \frac{M_0-M_1}{M_0+M_1}} \right] . \qquad (46)$$

The energy E_{2S} of the scattered protons at the distance S beneath the surface is related to the energy E_{20} with which the protons emerge from the target by:

$$E_{2S} = E_{20} + \int_{E_{20}(x=0)}^{E_{2S}(x=S/\cos\theta_2)} p\left(\frac{dE}{dx}\right)_2 dx. \qquad (47)$$

Combining equations 45 and 47 by means of the relation $E_{2S}=\alpha(\theta_L, M_0, M_1)E_{1S}$ one obtains

$$E_{20} = \alpha E_{10} - \alpha \int_{S/\cos\theta_1}^{0} p\left(\frac{dE}{dx}\right)_1 dx - \int_{0}^{S/\cos\theta_2} p\left(\frac{dE}{dx}\right)_2 dx, \qquad (48)$$

which is a relation among the initial bombarding proton energy E_{10}, the emergent energy E_{20} of the scattered protons from the target, and the depth S at which the scattering nuclei are located. The integrals can be evaluated numerically if the target composition is uniform. In practice, however, the integrands are evaluated at some intermediate energy E_p between the end point energies. The actual determination of the intermediate energy will be discussed later. (See Section III. D).

In the procedure followed in this experiment, E_{20} is fixed by the magnetic spectrometer. All the angles are fixed, and E_{10} is varied in

order to discover those particular values, E_{10}', for which counts are observed in the scintillation counter at the detector end of the spectrometer. Each such value E_{10}' determines by equations 46 and 48 a relation between the mass of the scattering nucleus M_0 and the depth S of the scattering nucleus beneath the surface of the target. Neither M_0 nor S is determined explicitly without further information, but in practice the target composition and expected contaminants are known, and furthermore, thin layers of contamination are almost always surface layers with S = 0. Atoms distributed in the target over a range of S lead to a continuum of E_{10}'. A typical experimental result is indicated in fig. 3 where the number of counts observed in the scintillation counter for a fixed incident proton charge upon the target is plotted as a function of E_{10}. Such curves in the following discussion will be referred to as momentum profiles for the target. Scattered protons which are detected at E_{10} = 322, 354, and 377 kev can be identified with the aid of equations 46 and 48 with S = 0 and with M_0 = 28, 16, and 12, respectively. It is expected that there are surface layers of silicon, oxygen, and carbon which come from the diffusion pump oil. The continuum beginning at E_{10} = 415 kev marks a distribution of nuclei with mass nine beginning at S = 0 and extending into the target.

Figure 4 gives the results of elastic scattering of protons from a clean beryllium target which had been previously bombarded by 300 kev krypton ions. The three peaks at 320, 350, and 375 kev can again be identified with S = 0 and with M_0 = 28, 16, and 12, respectively, as before. The broad peak at E_{10} = 334 kev could be identified with S = 0 and mass M_0 = 21.2; however, this peak was not observed when protons were scattered from beryllium before the krypton bombardment. Hence

it is reasonable to identify this group with mass 83.8, and equation 48 then determines the distance S at which these ions are embedded in the beryllium. The breadth of the distribution indicates that the krypton is distributed over a region of S values as a result of straggling.

It is necessary to obtain two momentum profiles for each ion bombardment; one from a clean target of the stopping material and another after the target has been bombarded with the ion at some predetermined energy. By subtracting the two profiles from each other, one can obtain the distribution of the embedded atom inside the target as a function of the distance S by use of equations 46 and 48. The peak is taken to be the probable range, and the energies corresponding to the half-maximum points on the embedded atom peak in the momentum spectra are used to calculate two other penetration depths, the difference of which is considered to be the range straggling in the experiment.

An example of the distribution of the embedded atoms in the target as obtained by subtracting the clean target profile from the bombarded target profile is given in fig. 5. The indicated error bars on the ordinates are probable errors in the counting statistics. A smooth curve was drawn by eye through the observed points. The uncertainty in the energies of the maximum and half-maximum points resulting from the uncertainty in the actual shape of the curve drawn through the observed points is indicated. These uncertainties in the energies were assigned on the basis of several attempts to draw any reasonable curve, other than the one given, through the observed points.

Figure 4 also indicates that there are instances when the maximum of the broad peak may be coincident with one of the surface contaminant peaks, and consequently, a greater uncertainty in the distance

S corresponding to the energy E_{10}' at the peak will result. This superposition can be eliminated by simply changing the angles θ_L, θ_1, and θ_2 of fig. 2. For example, if one desires to shift the broad peak to the right (relative to the contaminant peaks) in fig. 4, he can readily do this by decreasing the lab angle θ_L and increasing the target orientation angles θ_1 and θ_2. On the other hand, since α has the property of increasing towards unity with decreasing θ_L, it is to be expected that the relative separation between the surface contaminant peaks will decrease with decreasing θ_L. One may therefore choose to compromise between the relative separation of the contaminant peaks and the location of the broad peak relative to the contaminant peaks. Because it was usually not obvious beforehand where the broad peak would be located, the laboratory angle θ_L was always fixed at 129° or 130° throughout all the measurements.

III. D. Calculation of Range for A, Kr, and Xe Ions.

We now evaluate the integrands of equation 48 at the intermediate energies $E_p^{(1)}$ and $E_p^{(2)}$ for the first and second integral, respectively, and find that

$$E_{20} = \alpha E_{10} - \frac{S}{\cos\theta_1}\left[\alpha \left(\frac{dE}{dx}\right)_p\Big|_{E_p^{(1)}} + \frac{\cos\theta_1}{\cos\theta_2}\left(\frac{dE}{dx}\right)_p\Big|_{E_p^{(2)}}\right] \quad (49)$$

If we define the proton stopping cross section $\epsilon_p(E) = (dE/Ndx)_p$, where N is the number of stopping atoms per cm^3, we can solve equation 49 to obtain

$$t(gm/cm^2) \equiv \rho_0 S = \frac{(\alpha E_{10} - E_{20}) M_0 \cos\theta_1}{[\alpha_p \epsilon(E_p^{(1)}) + \frac{\cos\theta_1}{\cos\theta_2} p \epsilon(E_p^{(2)})] N_o} \quad . \tag{50}$$

ρ_0 is the density in gm/cm^3 of the stopping substance, $N_o = 6.025 \times 10^{23}$ is Avogadro's number, and M_0 is the gram atomic weight of the stopping atoms. If the concentration of the embedded impurity atoms is negligible, then the density, stopping atom mass, and proton stopping cross sections are simply those of the target which was bombarded by the ions. If the embedded atom concentration is not negligible, then a different procedure than the one outlined in this section must be given (see Section III. G). We calculate the range by using E_{10} at the maximum of the peak in fig. 4 or fig. 5 and using $\alpha(\theta_L, M_1, M_0^I) \equiv \alpha_I$ for the embedded atom. The proton energies, E_{10} and E_{20}, must be corrected for the energy lost in the surface contaminant layers, but we shall assume for the present discussion that this has already been done, and that E_{10} and E_{20} are the corrected proton energies.

Chilton, Cooper, and Harris (Chilton, 1954) have worked out the intermediate energy E_p at which the stopping cross sections should be evaluated. By assuming that $-_p(dE/dx) = kE^{-\gamma}$, where γ and k are constants over the energy region of interest, they obtain the expression

$$E_p = E_a\{1 + \frac{(\gamma-1)}{24} (\frac{\Delta E}{E_a})^2 + ...\} \quad , \tag{51}$$

where E_a is the average $(E_i+E_f)/2$ of the initial and final energies, and ΔE is the difference $E_i - E_f$ of the initial and final energies. Although the γ's are slightly different in the present experiment for the various tar-

gets bombarded by A, Kr, and Xe in the energy region of interest, the individual γ's are very nearly constant over the small energy intervals used in the range calculations. The most extreme case, that of 500-kev argon ions in beryllium, indicated a difference of less than 0.2 kev between E_a and E_p. Since the stopping cross section curves (Whaling, 1958) can be read in the vicinity of 300 kev only to within $\sim \pm 2$ kev, the difference in E_a and E_p is negligible, and E_a was used in all the computations.

To obtain E_a, we eliminate S from equations 45 and 47 and solve for E_{1S}. This gives

$$E_{1S} = \frac{\frac{\cos\theta_1}{\cos\theta_2} E_{10} + E_{20} \frac{{}_p\epsilon(E_p^{(1)})}{{}_p\epsilon(E_p^{(2)})}}{\frac{\cos\theta_1}{\cos\theta_2} + \alpha_I \frac{{}_p\epsilon(E_p^{(1)})}{{}_p\epsilon(E_p^{(2)})}} \quad . \tag{52}$$

We evaluate ${}_p\epsilon(E_p^{(1)})$ at E_{10} and ${}_p\epsilon(E_p^{(2)})$ at E_{20} to find a zero order $E_{1S}^{(0)}$. Since $E_{2S} = \alpha_I E_{1S}$, we can readily find first order average energies $[(E_{10}+E_{1S}^{(0)})/2]$ and $[(E_{20}+E_{2S}^{(0)})/2]$. These average energies are then used in expression 52 to obtain better values for E_{1S} and E_{2S}, and the iterative procedure is continued until E_{1S} and E_{2S} remain constant. Once the energies $E_p^{(1)}$ and $E_p^{(2)}$ are known, the range is given by equation 50.

An alternate procedure for calculating the range which presumably would eliminate all uncertainties in evaluating the integrals of equation 48 may be described as follows. One obtains a range-energy curve for protons in the target material. The graph should be sufficiently

accurate that range differences can be read to within 0.1 μ gm/cm^2 and energies to within 0.2 kev. One chooses arbitrarily any energy $E_{1S}^{(0)}$ such that $E_{20} < E_{1S}^{(0)} < E_{10}$, and then reads the range difference $t(E_{10})-t(E_{1S}^{(0)})$ from the graph. The quantity $[t(E_{10})-t(E_{1S}^{(0)})]\cos\theta_1$ represents our first estimate of the penetration depth. The range

$$t(\alpha_I E_{1S}^{(0)}) - \frac{\cos\theta_1}{\cos\theta_2}\,[t(E_{10}) - t(E_{1S}^{(0)})] \equiv t(E_{20}^{(0)})$$

is next obtained, and if the energy corresponding to $t(E_{20}^{(0)})$ is E_{20}, then the range difference $[t(E_{10}) - t(E_{1S}^{(0)})]\cos\theta_1$ is the desired penetration depth. If the energy corresponding to $t(E_{20}^{(0)})$ is not E_{20}, one picks a better $E_{1S}^{(0)}$ and repeats the process. The procedure is continued until an $E_{1S}^{(0)}$ is found such that the energy corresponding to $t(E_{20}^{(0)})$ is precisely E_{20}. This alternate procedure of calculating the range was used as a check on the argon and krypton in beryllium measurements by the previous method. Unfortunately, the proton range-energy curve which was used gave range differences only to within $\pm$ 0.2μgm/cm^2. The penetration depths calculated by the alternate procedure agreed with those calculated by the previous method within the same accuracy, viz., $\pm$ 0.2μgm/cm^2.

III. E. Range Straggling for A, Kr, and Xe Ions.

In the present experiment we are arbitrarily defining the range straggling as the full width at half maximum of the distribution of impurity atoms as obtained from the momentum profiles. It is to be expected that the observed width is broader than the "true" width as a result of the following sources which produce a lack of resolution in the results: variation in proton beam voltage, finite proton beam spot size

upon the target, finite exit slit size, variation of scattered proton energy with angle over the spectrometer entrance aperture, and proton energy straggling in the target.

Let us assume that the above finite sources of resolution, except for the proton straggling, combine in such a way that the resultant instrumental spread in energy of the observed protons is gaussian in shape (see Brown, 1951). Then the slope of the leading edge of the continuum distribution in the momentum profile, evaluated at the midpoint of the rise of the step, is $1/(\sqrt{2\pi}\sigma)$, where σ is the standard deviation of the distribution of energies.

The variation of scattered proton energy with angle over the entrance aperture of the spectrometer is reflected as a variation in the incident proton energy by means of the relation $\delta E_{1S}^{T} = -\frac{1}{\alpha_T^2}\frac{\partial \alpha_T}{\partial \theta_L} E_{2S}^{T}\delta\theta_L$ as is readily obtained by differentiating $E_{1S}^{T} = E_{2S}^{T}/\alpha_T(\theta_L, M_0^T, M_1)$. The spectrometer entrance aperture, $\delta\theta_L$, is obtained from Overley's calibration (Overley, 1961), and is approximately 4.2° at $\theta_L = 130^{\circ}$. If we assume that the distribution of energies arising from $\partial E_{1S}^{T}/\partial\theta_L$ is rectangular, then the mean square deviation of these energies is $(1/12)(\delta E_{1S}^{T})^2$. Since we are interested, however, in obtaining the effect of the instrumental width on the impurity atom distribution, we can subtract out the variance of the $\partial E_{1S}^{T}/\partial\theta_L$ distribution for the target atoms at the surface and add to the result the variance for the impurity atoms $(1/12)(\delta E_{1S}^{I})^2$ inside the target. This gives, as our estimate of the instrumental spread of energies:

$$\sigma_{inst}^2 = \sigma^2 - \frac{1}{12}(\delta E_{10}^{T})^2 + \frac{1}{12}(\delta E_{1S}^{I})^2. \qquad (53)$$

As an estimate of the mean square energy deviation due to proton straggling in the target thickness $N\Delta R$ and atomic number Z_0, we use (Bohr, 1948, p. 95), $\sigma_B^2 = 4\pi e^4 N Z_0 \Delta R$. The incident proton straggling over the path $\Delta R = S/\cos\theta_1$ is reduced by a factor $\alpha = (dE_2/dE_1)$ in the scattering event and added to the straggling over the emergent path $S/\cos\theta_2$ to find the total deviation in E_{20} given by

$$\sigma_B^2(E_{20}) = \alpha^2 \sigma_B^2 (S/\cos\theta_1) + \sigma_B^2 (S/\cos\theta_2) \quad .$$

Expressed in terms of E_{10} we find

$$\sigma^2(E_{10})_{\text{prot. stragg.}} = 4\pi e^4 N Z_0 S \left[\frac{p^{\epsilon}(E_{10})}{p^{\epsilon}(E_{20})} \frac{p^{\epsilon}(E_{2S})}{p^{\epsilon}(E_{1S})} \frac{1}{\alpha}\right]^2 \cdot \left[\frac{\alpha^2}{\cos\theta_1} + \frac{1}{\cos\theta_2}\right] . \tag{54}$$

The Bohr value σ_B^2 should represent a good approximation for substances of comparatively small atomic number in which case all the atomic electrons should contribute to the proton stopping and straggling. This conclusion is borne out by the experimental results of Madsen and Venkateswarlu (Madsen, 1948) for proton straggling in beryllium and mica foils. The results of Reynolds (Reynolds, 1953) indicate that the proton straggling in xenon and krypton is of the same order of magnitude as the Bohr value; the results of Brown, et al. (Brown, 1951) indicate that the root mean square deviation of the proton straggling in beryllium is 30 per cent greater than the Bohr value.

An attempt was made to fit one of the observed impurity atom distributions by folding a gaussian of variable width (to allow for the change in proton straggling as a function of depth beneath the surface) into a gaussian of fixed width. The results of the numerical calculation indicated that one could fit the side of the distribution toward the surface with a gaussian of known width, or could approximately fit the side of

the distribution away from the surface with a gaussian of different width, but could not simultaneously fit both sides with a single gaussian of fixed width by the folding process. This is not surprising since it is difficult to say definitely from the experimental results what the true shape of the impurity atom distributions inside the target should be. The xenon curves indicated an asymmetrical distribution with the side away from the surface being broader than the side toward the surface. Several of the krypton curves indicated the same type of asymmetry, but the remainder of the curves appeared to be approximately symmetrical in shape. The majority of the argon curves appeared to be symmetrical, although some were peaked slightly toward the surface, and even a few slightly peaked away from the surface.

The procedure adopted for estimating the true width was to fit one side of the observed distribution of impurity atoms with a gaussian of one width and the other side of the distribution with a gaussian of different width. As an estimate of the "average" proton straggling on the side of the distribution toward the surface, the penetration depth corresponding to the lower half maximum of the observed distribution was first calculated with equation 50, and the result used in equation 54 to calculate a $\sigma^2_{\text{prot. straggl.}}\Big|_{\text{lower half}}$. Then the "true half width" of this part of the distribution is given by:

$$W^{\text{lower half}}_{\text{corrected}} = \sqrt{2\ln 2}\sqrt{\frac{(W^{\text{lower half}}_{\text{observed}})^2}{2\ln 2} - \sigma^2_{\text{inst.}} - \sigma^2_{\text{prot. stragg.}}\Big|_{\text{lower half}}} \qquad (55)$$

where $W^{\text{lower half}}_{\text{observed}}$ is the difference of energies corresponding to the maximum and lower half maximum of the observed distribution. A similar procedure yields for the "true half width" of the side away from the surface

$$W^{\text{upper half}}_{\text{corrected}} = \sqrt{2\ln 2}\sqrt{\frac{(W^{\text{upper half}}_{\text{observed}})^2}{2\ln 2} - \sigma^2_{\text{inst}} - \sigma^2_{\text{prot stragg}}}\Bigg|_{\text{upper half}} . \tag{56}$$

One then takes the energy corresponding to the maximum of the peak, subtracts $W^{\text{lower half}}_{\text{corrected}}$ from it, and calculates the corresponding penetration depth, t(lower half max), by use of equation 50. One also calculates a t(upper half max) by adding $W^{\text{upper half}}_{\text{corrected}}$ to the energy corresponding to the maximum of the peak and using the resulting energy in equation 50. The difference, t(upper half max) - t(lower half max), then gives an appropriate measure of the ion range straggling in the target.

The effect of the instrumental and proton straggling corrections on the ion straggling depends, of course, upon the relative magnitude of $W^{\text{upper half}}_{\text{observed}}$ and $W^{\text{lower half}}_{\text{observed}}$ in comparison to σ_{inst} and $\sigma_{\text{prot stragg}}$. It was found that the ion straggling correction, (i.e., t_{stragg}(uncorrected) - t_{stragg}(corrected)) varied from 0.7 to 2.9 μgm/cm^2 (or 7.8% to 40% of t_{stragg}(uncorrected)) for the 50-kev ions, to 0.9 to 1.8 μgm/cm^2 (or 3.1% to 7.4% of t_{stragg}(uncorrected)) for the 500-kev ions.

III. F. Interference Between Protons Scattered from Embedded Atoms and Target Atoms.

The magnetic spectrometer used in this experiment accepts scattered protons lying in the energy interval E_{20}-dE_{20} to E_{20}. This energy interval, dE_{20}, corresponds to a target lamina of thickness dS, which presents a target of thickness $dS/\cos\theta_1$ to the incident proton beam. The relation between $dS/\cos\theta_1$ and dE_{20} for a target of uniform composition is given by equation AIII4, and that for a target of continuously varying composition is given by equation AIII10. It is readily seen from this lat-

ter equation that, for a fixed dE_{20}, $dS/\cos\theta_1$ is reduced by the presence of the embedded impurity atoms as a result of the increased proton stopping cross section per target atom. Since the scattering yield is proportional to $dS/\cos\theta_1$, one anticipates a dip in the momentum profile when the protons scatter from target atoms in the region where the embedded atoms exist. The penetration depth of the ion in the target and the range straggling can be obtained from this dip in precisely the same manner as from the peak.

An example of a profile where both peak and dip are present is shown in fig. 6. The dashed profile is obtained by protons elastically scattered from a clean beryllium target; the solid line profile is obtained by scattering from a beryllium-plus-nitrogen target. The qualitative features of analysis are similar to those described previously. The displacement of the beryllium step in the beryllium-plus-nitrogen profile is attributed to the increased proton energy required to penetrate the surface layers of carbon and silicon built up during the long ionic bombardment (see Table I).

If $\alpha(\theta_L, M_0^T, M_1)$ is approximately equal to $\alpha(\theta_L, M_0^I, M_1)$, or if the embedded atoms are distributed over a broad region of the target as a result of range straggling, then the peak and dip will overlap each other. The former condition applies to nitrogen in carbon and to neon in carbon where $\alpha(129^\circ, C, p)/\alpha(129^\circ, N, p) = 0.962$ and $\alpha(129^\circ, C, p)/\alpha(129^\circ, Ne, p) = 0.900$, respectively, and the latter condition applies to nitrogen in aluminum. For these three cases where the peaks and dips interfere, the true peaks and dips can be calculated from the observed peaks and dips with the aid of the thick target yield formulas given in Appendix III.

A reasonable check on the use of these formulas in such calculations is to compare the shape of the distribution predicted by formula AIII5 with that obtained experimentally from a target of known composition. Elastic scattering of protons from copper is known to be Rutherford (Bader, 1956) except for a multiplicative electron screening factor (Wenzel, 1952) of magnitude $(1 - 32.6Z_{Cu}/E_{1S}(ev))$. A target of electrolytic copper was made by polishing successively with 2/0 emery polishing paper, 4/0 emery polishing paper, 1550AB polishing alumina no. 1, 1551AB alpha polishing alumina no. 2, and 1552AB gamma polishing alumina no. 3, with careful washing between each abrasive. The scattering yield from this target is illustrated in fig. 7 and is compared with the predicted yield of formula AIII5 (solid curve). The results of this test seem to indicate that the experimental points fall about 3 per cent above the predicted curve at the high energy end of the curve. This 3 per cent discrepancy may be due, at least partially, to the $\pm$ 3 per cent uncertainty in the proton stopping cross sections of copper (Bader, 1956). Protons were also elastically scattered from a target made by evaporating copper on a clean microscope slide, and the scattering yield was about 1.5 per cent higher than the yield of fig. 7 at E_{10} = 310 kev; this indicated that the polished target surface was comparable in smoothness to that of the evaporated target surface.

In order to use the formulas of Appendix III, it is necessary to know the proton scattering cross sections, $d\sigma/d\Omega$, for the embedded atoms and also for the target atoms. The scattering cross sections for the target atoms, carbon and aluminum, are readily obtained from the clean target profiles. The proton scattering cross section for N^{14} is

essentially Rutherford except at the 278 kev resonance (Pixley, 1957); the width of this resonance is only 1.7 kev, and is therefore considerably less than the broad width due to nitrogen ion straggling. The scattering cross section for Ne^{20} at these energies is not known, and we have assumed it to be Rutherford. The quantity $CV\Omega_L/zeR_c$ was determined by elastic scattering of protons from copper with the assumed Rutherford-plus-electron screening correction behavior mentioned previously.

The "unscrambling" procedure will be described for nitrogen in aluminum, where the dip occurs to the left of the peak; however, the procedure is completely analogous for nitrogen and neon in carbon, where the dip occurs to the right of the peak. For nitrogen in aluminum, there exists a small energy region of non-interference due to the difference of $\alpha(\theta_L, N, p)$ and $\alpha(\theta_L, Al, p)$. One picks an energy E_{10}^T close to the left hand edge of the dip and calculates an E_{1S}^T with equation 52. Using this E_{1S}^T and ν = "T" in equation AIII11, then, one calculates (n_T^S/n_I^S) with the aid of the observed clean target profile and equation AIII5. An E_{10}^I is then obtained from equation 50 by equating the penetration depth S as determined from the parameters $\alpha(\theta_L, Al, p)$, E_{10}^T, and E_{1S}^T associated with target atom scattering to the depth S as determined from the parameters $\alpha(\theta_L, N, p)$, E_{10}^I, E_{1S}^I associated with impurity atom scattering. An E_{1S}^I is then found from equation 52 and the result used along with E_{2S}^I and (n_T^S/n_I^S) in equation AIII11 (now with ν = "I") to determine the predicted yield from the embedded atoms. This procedure gives one point on the reconstructed dip, and the scattering yield so determined from the reconstructed dip is used to calculate additional points on the peak. This procedure is continued until the true dip and peak are obtained. Figure 8 shows the peak-dip reconstruction for 296.2 kev nitrogen in aluminum. The fact that the calculated peak joins the observed

curve within the accuracy of the observed points lends support to the validity of the method. It is seen that the penetration depth and range straggling are greater using the reconstructed data than they would be if the uncorrected data were used.

It is pointed out in Appendix III that the use of equation AIII11 applies only to those combinations of ion and target where $_p(dE/dx)^I/_p(dE/dx)^T$ is independent of energy. Let us assume that $-_p(dE/dx) = k/E^\gamma$ throughout the region of proton energies used in the target where the embedded atoms are present. Then

$$_p(dE/dx)^I/_p(dE/dx)^T = (k_I/k_T)E^{\gamma_T-\gamma_I},$$

and the difference, $\gamma_T-\gamma_I$, gives a measure of the dependence upon energy of $_p(dE/dx)^I/_p(dE/dx)^T$. Table III lists the proton energy region used in the neon and nitrogen range calculations and also gives the difference, $\gamma_T-\gamma_I$, for various ions and targets as obtained from Whaling's compilation (Whaling, 1958). Formula AIII11 is applicable only to nitrogen in carbon, and should be least applicable for nitrogen in aluminum. The target with the greatest concentration of impurity atoms (that of 296.2 kev nitrogen in aluminum) was selected and divided into five regions, and a calculation similar to the above ones, but based upon equation AIII8 rather than AIII11, was carried out. The result of the calculation indicated that the maximum of the reconstructed peak was about 15 counts less than that obtained by using formula AIII11. This discrepancy is of negligible significance as far as the maximum and half-maximum points of the reconstructed dip are concerned; therefore, formula AIII11 was used in all the peak-dip reconstruction calculations.

III. G. Effect of Embedded Atoms on the Range Measurements. The Range of N and Ne Ions.

After prolonged bombardment the concentration of foreign atoms embedded in the target may reach significant values, as shown in column four of Table I, and it is necessary to consider what effect, if any, atoms deposited at the beginning of the ion bombardment have upon the ions which penetrate this region at the end of the bombardment. A preliminary qualitative investigation of this question is shown in fig. 9 which shows the proton scattering from a Be target which had been bombarded with various amounts of 300.7 kev Kr ions. The maximum concentration of Kr ion reached in each bombardment is shown in the figure, expressed as an effective molecular composition. Protons scattered from the lesser concentrations (those used to determine range values) indicate that the embedded ions have no effect greater than the experimental uncertainty. Concentrations of more than 1 Kr atom for ~ 30 Be atoms do introduce a noticeable shift in the peak. Similar experiments with argon atoms embedded in beryllium demonstrated that argon atom concentrations of $Be_{21}A$, two times as great as those used in measuring the argon range, produced no detectable shift in the proton scattering peak. The high concentrations reached in the measurements of N and Ne ion ranges have led us to go through the following analysis which permits an estimate of the difference between the range in the pure target and the range in the mixture of target plus embedded atoms, if dE/dx for both ion and proton in the embedded atom material is known.

Let us assume that the range-energy behavior of the ion in target atoms, in embedded atoms, and in a mixture of target and embedded atoms can be described by the following:

$$
\begin{aligned}
{}_{I}t_{I} &\equiv \rho_{I}\,{}_{I}R_{I} = f_{1}\,(Z_{I}, M_{0}^{I}) \cdot g(E) \\
{}_{I}t_{T} &\equiv \rho_{T} \cdot {}_{I}R_{T} = f_{2}(Z_{I}, M_{0}^{I}; Z_{T}, M_{0}^{T}) \cdot g(E) \\
{}_{I}t_{mix} &\equiv \rho_{mix} \cdot {}_{I}R_{mix} = f_{3}(Z_{I}, M_{0}^{I}; Z_{T}, M_{0}^{T}) \cdot g(E)
\end{aligned}
\tag{57}
$$

where ${}_{I}t_{y}$ and ${}_{I}R_{y}$ refer to the range in $\mu gm/cm^{2}$ and centimeters, respectively, of the ion in substance y; ρ_{y} is the density of substance y; g(E) is the energy dependence of the range-energy curves; and f_{1}, f_{2}, and f_{3} represent the charge and mass dependence for the three cases. Since the stopping of the ion in the mixture, ${}_{I}(dE/dx)_{mix}$, is related to the stopping of the ion in the target atoms and in the embedded atoms by the relation ${}_{I}(dE/dx)_{mix} = {}_{I}(dE/dx)_{T} + {}_{I}(dE/dx)_{I}$, we find by differentiating equations 57 that ${}_{I}(dE/dx)_{I} = \rho_{I}/(f_{1}g'(E))$, etc., and, as a result

$$
\frac{1}{{}_{I}R_{mix}} = \frac{1}{{}_{I}R_{T}} + \frac{1}{{}_{I}R_{I}} \quad . \tag{58}
$$

Now $\rho_{T} = n_{T}M_{0}^{T}/N_{o}$, $\rho_{I} = n_{I}M_{0}^{I}/N_{o}$, and $\rho_{mix} = n_{T}M_{0}^{T}/N_{o} + n_{I}M_{0}^{I}/N_{o}$, where n_{T} and n_{I} are the number of target and impurity atoms, respectively, per unit volume, N_{o} is Avogadro's number, and M_{0} is the gram atomic weight. Equation 58 can, therefore, be written in the form:

$$
{}_{I}t_{T} = {}_{I}t_{mix}\left[\frac{1 + (n_{I}M_{0}^{I}/n_{T}M_{0}^{T}) \cdot ({}_{I}t_{T}/{}_{I}t_{I})}{1 + (n_{I}M_{0}^{I}/n_{T}M_{0}^{T})}\right] \tag{59}
$$

which enables one to find the desired range of the ion in the target material if the ion range in the mixture is known and if the ratio ${}_{I}t_{T}/{}_{I}t_{I}$ and impurity concentration n_{I} are known.

Let us divide the target into two regions: (1) a region extending from the surface up to the left-hand edge of the peak (or dip), and (2) a region extending from the left-hand edge of the peak (or dip) up to the maximum of the peak (or minimum of the dip). This division is illustrated in fig. 10. The first region contains only target atoms, and its thickness, ${}_{I}t_{T}^{(1)}$, can readily be calculated by using the energy at the left-hand edge of the peak, $E_{10}^{(1)}$, along with the target atom proton stopping cross sections in equation 50.

Calculation of the thickness, ${}_{I}t_{T}^{(2)}$, of the second region is somewhat more involved. The first ions which come to rest in this region see no impurity atoms, whereas those ions at the end of the bombardment see the full concentration of embedded atoms. We have essentially found, therefore, at least as far as the second region is concerned, the range of the ions in a mixture of target atoms and impurity atoms, where the impurity concentration is one-half the concentration at the end of the ion bombardment. Consequently, we use $n_I = \frac{1}{2}(n_I)_{final}$ in expression 59.

The incident protons of energy E_{10}^{Max}, corresponding to the maximum of the peak, enter the target and are slowed down until they reach the beginning of region 2 with an energy

$$E_1^a = E_{10}^{Max} - {}_{p}\epsilon_{T}(E_p^{(1)})N_{oI}{}_{I}t_{T}^{(1)}/(\cos\theta_1 M_0^T)$$

where $E_p^{(1)}$ is given by equation 51. The protons enter a region of monotonically increasing impurity atom concentration and penetrate beneath the surface until they scatter from impurity atoms on the layer of greatest impurity concentration. The scattered protons encounter a monotonically decreasing impurity atom concentration until they arrive at the region 1 - region 2 interface with an energy

$$E_3 = E_{20} + {}_p\epsilon\,(E_p^{(2)}) N_{oI} {}^{t}{}_{T}^{(1)}\,(1/\cos\theta_2 M_0^T)\,,$$

where $E_p^{(2)}$ is obtained from equation 51. The ratio $(n_I/n_T)_{max}$, at the maximum of the peak, can readily be calculated by the formulas of Appendix III by the method indicated in the previous section. Since the impurity atom concentration is a monotonic function of the depth in region 2 as a result of the way region 2 was defined, it is reasonable to approximate the continuously changing impurity atom concentration by a uniform concentration of amount $\frac{1}{2}(n_I/n_T)_{max}$. The range in the mixture (in region 2) is then found from equation 48:

$$I^{t}{}_{mix}^{(2)} \equiv (\rho_T+\rho_I)\cdot {}_I R_{mix} = (n_T M_0^T/N_o)\cdot [1+\tfrac{1}{2}(n_I/n_T)_{final}\cdot (M_0^I/M_0^T)]\cdot {}_I R_{mix}$$

$$= \frac{(\alpha_I E_1^a - E_3)\cos\theta_1 M_0^T [1+\frac{1}{2}(n_I/n_T)_{final}\cdot (M_0^I/M_0^T)]}{\left\{\alpha_I[{}_p\epsilon_T(E_p^{(1)}) + \frac{1}{2}(n_I/n_T)_{max}\cdot {}_p\epsilon_I(E_p^{(1)})] + \frac{\cos\theta_1}{\cos\theta_2}[{}_p\epsilon_T(E_p^{(2)}) + \frac{1}{2}(n_I/n_T)_{max}\cdot {}_p\epsilon_I(E_p^{(2)})]\right\} N_o} \qquad (60)$$

where the intermediate energies, $E_p^{(1)}$ and $E_p^{(2)}$, are close to the average energies as is shown in Appendix IV. The average energies, $E_a^{(1)}$ and $E_a^{(2)}$, were therefore used in equation 60. Since we are using $(n_I/n_T) = \frac{1}{2}(n_I/n_T)_{final}$ in equation 59 and are using $(n_I/n_T)_{final} = \frac{1}{2}(n_I/n_T)_{max}$, we obtain, by putting equation 60 into 59, the range of the ion in target atoms for region 2:

$$I^{t}{}_{T}^{(2)} = \frac{(\alpha_I E_1^a - E_3)\cos\theta_1 M_0^T\cdot [1+\frac{1}{4}(n_I/n_T)_{max}\cdot (M_0^I/M_0^T)\cdot ({}_I t_T/{}_I t_I)]}{\left\{\alpha_I[{}_p\epsilon_T(E_p^{(1)}) + \frac{1}{2}(n_I/n_T)_{max}\cdot {}_p\epsilon_I(E_p^{(1)})] + \frac{\cos\theta_1}{\cos\theta_2}[{}_p\epsilon_T(E_p^{(2)}) + \frac{1}{2}(n_I/n_T)_{max}\cdot {}_p\epsilon_I(E_p^{(2)})]\right\} N_o} \qquad (61)$$

If the range is found from the minimum of the dip rather than the maxi-

mum of the peak, then α_I is replaced by α_T in equation 61, and the appropriate corresponding energies are used. The ratio ${}_I t_T / {}_I t_I$ of ion ranges in target and impurity material is not known. We estimated this ratio for N and Ne ions in various materials using our uncorrected range measurements for these ions in C, Be, and Al and extrapolating to the other ion target material by means of the theoretical dependence of the range on Z_0 and M_0 (see equation 26). We must emphasize again that the theoretical expression describes the projected range only when $M_1 >> M_0$. Our experimental results for N and Ne ions indicate that in the velocity region of this experiment, the Z_0 and M_0 dependence of the range expression still fits fairly well and justifies the use of the theoretical expression in estimating ${}_{Ne} t_{Be} / {}_{Ne} t_{Ne}$ and ${}_{Ne} t_C / {}_{Ne} t_{Ne}$.

The final range, then, is the sum ${}_I t_T^{(1)} + {}_I t_T^{(2)}$ of the penetration depths for the two regions. By this detailed analysis, the neon ranges were decreased by a maximum of 1.8 per cent and the nitrogen ranges by a maximum of 7.7 per cent, with the largest numerical change being 8.6 μ gm/cm^2 for 296.2 kev N ions in Al. All other measurements were unaffected, in accord with the behavior as anticipated from Table I and the prefatory remarks of this section.

III. H. Range Straggling for N and Ne Ions.

To determine the range straggling for N and Ne ions, the target is divided into 3 regions: (1) a region extending from the surface up to the left-hand edge of the peak, (2) a region extending from the left-hand edge of the peak to the lower half maximum of the peak, and (3) a region extending from the lower half maximum of the peak to the upper

half maximum of the peak. The thickness of the first layer, ${}_{I}t_{T}^{(1)}$, is the same as that obtained in the previous section. The energy E_3 is also the same as that of the previous section since the spectrometer is fixed, and the energy

$$(E_1^a)^{LHM} = E_{10}^{LHM} - {}_{p}\epsilon_{T}(E_p^{(1)})N_{oI}{}_{I}t_{T}^{(1)}/(\cos\theta_1 M_0^T)$$

is readily obtained from the lower half maximum energy, E_{10}^{LHM}, of the momentum profile. As far as the second region is concerned, we are interested only in the energy lost by the protons moving through the region; therefore, rather than calculating a ${}_{I}t_{T}^{(2)}\Big|^{LHM}$, we instead calculate a ${}_{I}R_{mix}^{(2)}\Big|^{LHM}$ from equation 60 by using $(E_1^a)^{LHM}$, E_3, the appropriate proton stopping cross sections, and by replacing $(n_I/n_T)_{max}$ by $\frac{1}{2}(n_I/n_T)_{max}$ throughout the equation. The replacement of $(n_I/n_T)_{max}$ by $\frac{1}{2}(n_I/n_T)_{max}$ is made to account for the decreased impurity concentration in region 2. If the energy at the upper half maximum of the peak as obtained from the profile is E_{10}^{UHM}, then the incident proton energy at the region 2 - region 3 interface is

$$E_1^b = E_{10}^{UHM} - {}_{p}\epsilon_{T}(E_p'^{(1)})N_{oI}{}_{I}t_{T}^{(1)}/(\cos\theta_1 M_0^T) - [{}_{p}\epsilon_{T}(E_p''^{(1)}) +$$

$$\tfrac{1}{4}(n_I/n_T)_{max}\,{}_{p}\epsilon_{I}(E_p''^{(1)})]\,[n_T{}_{I}R_{mix}^{(2)}\Big|^{LHM}/\cos\theta_1] \quad ,$$

where $E_p'^{(1)}$ and $E_p''^{(1)}$ are the appropriate intermediate energies in region 1 and region 2, respectively. In a similar manner, the proton energy with which the scattered protons leave the region 2 - region 3 interface is

$$E_3^b = E_3 + [{}_{p}\epsilon_{T}(E_p''^{(2)}) + \tfrac{1}{4}(n_I/n_T)_{max}\,{}_{p}\epsilon_{I}(E_p''^{(2)})]\;n_T R_{mix}^{(2)}\Big|^{LHM}/\cos\theta_2 \,.$$

The range straggling, t_{stragg}, for the ion is then determined by replacing E_1^a by E_1^b, replacing E_3 by E_3^b, and replacing $(n_I/n_T)_{max}$ by $\frac{3}{2}(n_I/n_T)_{max}$ along with the appropriate stopping cross sections in equation 61. The replacement of $(n_I/n_T)_{max}$ by $\frac{3}{2}(n_I/n_T)_{max}$ is made to account for the increased impurity atom concentration in region 3.

Before the range straggling can be calculated, however, it is necessary to calculate the instrumental and proton straggling effects upon the width of the observed distribution of impurity atoms. This is done in the same manner as was done for the A, Kr, and Xe measurements.

By dividing the target into three regions, the neon range straggling was decreased by a maximum of 8.2 per cent from a "one region" range straggling calculation neglecting the presence of the impurity atoms. The nitrogen range straggling was decreased by a maximum of 19.3 per cent, with the largest numerical change for either ion being 14.7 μ gm/cm^2 for 296.2 kev N ions in Al. By including the instrumental and proton straggling widths, the region 1-2-3 method range straggling values were further decreased by a maximum of 4.7 per cent for neon ions and 11.0 per cent for nitrogen ions, with the largest numerical change being 5.2 μ gm/cm^2 for 400 kev N ions in Al.

III. I. Surface Layer Corrections for Proton and Ion Energies.

The unavoidable deposition of contamination on the surface of the target during the ion and proton bombardment can influence our measurements in two ways. First, the incident ions lose energy in the contamination layer and strike the target with energy less than the bom-

barding energy. Second, the protons lose energy in going through this layer twice, and the observations must be corrected to take this into account. The fact that the layer thickness increases during the course of the measurement further complicates the analysis. Both the thickness and composition of the layer at any time, as well as the stopping cross sections for protons and heavy ions in the contamination material, must be known in order to correct our results for the effect of this surface layer. Not all of this information is known, and it is necessary to make the following assumptions in order to estimate the effect of the surface layer on our measurements.

(1) The composition of the layer is determined from the relative yields of protons elastically scattered from the C, O, and Si components on the assumption that the scattering follows the Rutherford formula. The relative yields are given by the areas under the component peaks in the profile such as the one shown in fig. 4. It is assumed that the yield from component x of atomic number Z_x is proportional to $n_x Z_x^2/E_{10}^2(x)$, where n_x is the number/cm^3 of x atoms, and $E_{10}(x)$ is the bombarding energy at which scattering from the x component is detected. The ratios n_O/n_C and n_{Si}/n_C are determined in this way.

(2) The energy loss $_p\Delta E$ of protons passing through the layer causes the midpoint $E_{10}(T)$ of the target step in fig. 4 to be displaced from the position $E'_{10}(T)$ which would be observed in the absence of any contamination layer. The energy $E'_{10}(T)$ can be computed from the energy of the protons scattered by C, O, and Si, which are not displaced, and the dynamics of the scattering event. The energy at which scattering from C, O, and Si occurs is not necessarily the maximum of the respective peaks in the profile, and the proper energy position on the peak

is determined by trying various points (1/2 maximum, 3/4 maximum, etc.) on each peak until a value is found which leads to the same scattered energy for each peak. Once $E_{10}(T) - E'_{10}(T)$ is known, the calculation of ${}_p\Delta E$ is straightforward. The largest individual numerical corrections of this type occurred in the 400 kev N in Be measurement, and were ${}_p\Delta E_{10} = 2.6$ kev for the incident protons and ${}_p\Delta E_{20} = 3.8$ kev for the scattered protons; the corresponding surface layer thickness was 5.8 per cent of the ion penetration depth beneath the surface. In the lowest energy xenon in beryllium measurement, however, where ${}_p\Delta E_{10} = 1.5$ kev and ${}_p\Delta E_{20} = 1.8$ kev, the thickness of the layer for protons was almost 80 per cent of the ion penetration depth beneath the beryllium surface.

(3) The energy loss ${}_I\Delta E$ of heavy ions passing through a layer in which protons lose energy ${}_p\Delta E$ is given by the following relation which follows directly from the definition of the stopping cross section:

$$\frac{{}_p\Delta E}{{}_I\Delta E} = \frac{{}_p\epsilon_C + (n_0/n_C)\,{}_p\epsilon_0 + (n_{Si}/n_C)\,{}_p\epsilon_{Si}}{{}_I\epsilon_C + (n_0/n_C)\,{}_I\epsilon_0 + (n_{Si}/n_C)\,{}_I\epsilon_{Si}} \qquad (62)$$

where ϵ_x is the stopping cross section in material x and the left subscript refers to a moving proton or heavy ion. The number ratios are obtained in (1) above. The proton stopping cross sections are known, or can be estimated within a few per cent. In order to determine the stopping cross sections ${}_I\epsilon$ for the heavy ions, it is important to remember that we are concerned with the energy lost in the surface layer of thickness ΔR, i.e., we wish to know the stopping cross sections as determined from the projected ranges. The stopping cross sections for the

heavy ions in carbon, ${}_{I}\epsilon_{C}$, are obtained directly by differentiating the experimental projected range-energy curves. The values of ${}_{I}\epsilon_{O}$ and ${}_{I}\epsilon_{Si}$ for A, Kr, and Xe ions are obtained as follows: (a) obtain ${}_{I}\epsilon_{Be}^{experimental}$ from the experimental data; (b) estimate ${}_{I}\epsilon_{Be}^{theory}$ and ${}_{I}\epsilon_{O}^{theory}$ with the theory of Section II. D; (c) estimate the projection corrections $P_{Be} = {}_{I}t_{Be}^{proj}/{}_{I}t_{Be}^{theory}$ and $P_{O} = {}_{I}t_{O}^{proj}/{}_{I}t_{O}^{theory}$ using equation 36; and (d) combine to obtain

$$ {}_{I}\epsilon_{O}^{predicted} = \frac{{}_{I}\epsilon_{O}^{theory}}{{}_{I}\epsilon_{Be}^{theory}} \frac{P_{Be}}{P_{O}} {}_{I}\epsilon_{Be}^{experimental} . $$

A similar expression is obtained for ${}_{I}\epsilon_{Si}^{predicted}$.

For N and Ne ions, it is anticipated from Section II. D that neither the theory of Section II nor the projection corrections based upon this theory is applicable. No projection corrections were made for these ions because it is not known how much of the stopping is due to elastic scattering from the surface layer atoms and how much is due to ionization and excitation of the surface layer atoms. A fair estimate of ${}_{I}\epsilon_{Si}$ and ${}_{I}\epsilon_{O}$ should be obtained, however, by extrapolating the measured values using the theoretical charge and mass dependence of Section II. D.

(4) The proton energy loss ${}_{p}\Delta E$ was measured after a known charge density Q of ions and protons had been deposited on the target. It is assumed that ${}_{p}\Delta E$ is proportional to Q to compute the thickness of the layer for other amounts of bombardment. Our observations of the variation of ${}_{p}\Delta E$ with Q are consistent with this assumption.

(5) For the energy lost by the ions in the surface layer, it is reasonable to use one-half the final thickness of the layer since when

the ion bombardment begins there is no surface layer. The appropriate $_{p}\Delta E$ to use in equation 62 to calculate $_{I}\Delta E$ is obtained from (4) above using the ion charge density Q' at the end of the ion bombardment. The most noticeable ion beam energy corrections of this type were for the low energy ($\approx$ 50 kev) ions, being 17 kev for Xe in Be, 5.2 kev for A in B^{10}, 4.8 kev for Ne in Be, 4.1 kev for Kr in Be, and 3.2 for N in Al. The corrections on all other combinations of ions, energies and targets were < 4 per cent, and were generally less than 2 per cent.

IV. ERRORS

Errors in the range and range straggling measurements arise from a number of sources and are best illustrated by referring to Tables IV - VII where the individual errors are listed along with the contribution of each error to the total probable error. The case given in Table IV is that of krypton in beryllium, but these results are typical of all the Kr, A, and Xe measurements. The values listed are for the 50- and 500-kev measurements, and, although the values at the intermediate energies may fluctuate somewhat about these values, there is generally a decreasing per cent of error with increasing ion energy. The effect of each error is obtained by independently varying the appropriate parameter in expression 50. By far the largest source of error is the location of the energy E_{10} at the maximum of the peak due to (1) statistical fluctuations in counting the scattered protons, (2) the intrinsic breadth of the peaks themselves, and (3) the finite resolution of the incident proton beam energy. The error designated spectrometer drift is assigned on the following basis: during many of the measurements protons were scattered from a clean copper target and also from a fresh spot on the beryllium target (or appropriate target) and comparison then made between the spectrometer energies so obtained from the midpoints of the two steps. The two proton scatterings were made at different times during the course of the experiment, and should therefore give an indication as to how much the spectrometer drifted during the elapsed time interval. The results of the scatterings also give an upper limit on the drifting of the electrostatic analyzer due to temperature or other effects, since, if the analyzer scale was displaced (and the spec-

trometer did not drift), the copper step would likewise be displaced from the beryllium step. (We are assuming, of course, that both analyzer and spectrometer did not simultaneously drift in such a manner that one effect would cancel the other.) The uncertainty of the electrostatic analyzer calibration itself has little effect on the range measurement since E_{20} is calibrated against the E_{10} scale, so that, according to equation 50, the range is roughly proportional to the electrostatic analyzer constant. The remaining errors are listed in Table IV. The largest of these errors is in the proton stopping cross sections and is ± 3 per cent. Although the presence of the impurity atoms in the target presumably would alter the range measurements, we have shown in fig. 9 and in the discussion of Section III. G that the presence of the impurity atoms is negligible insofar as the Kr, Xe, and A measurements are concerned.

Table V lists the errors in the 50- and 500-kev Kr in Be range straggling measurements. The location of the energies at the lower and upper half maximum points on the peak generally constitutes the largest source of error. The uncertainty in σ_{inst} arises from the uncertainty in determining the slope of the target atom step in the profile. An uncertainty in $\sigma_{prot\ stragg}$ of, perhaps, at least 30 per cent is expected on the basis of the measurements of Brown, et al., (Brown, 1951). For those measurements where the total energy lost by the protons in the target is $< \sim 20$ kev, a larger uncertainty in $\sigma_{prot\ stragg}$ is assigned because the proton straggling is then not expected to be gaussian. The results of fig. 9 seem to indicate that the ion straggling increases with increasing ion bombardment

time. The width at half maximum of the peaks is the same within about 5 per cent for the 30 μcoul and 70 μcoul ion bombardments, but appears to be about 15 per cent higher for the 450 and 150 μcoul bombardments. The widths at half maximum of the peaks in the A in Be tests were the same within about 5 per cent. An uncertainty of ~5 per cent was therefore assigned to the straggling on the basis of these tests. The proton stopping cross sections in Table V are uncertain to within 3 per cent, and the remaining sources as listed in Table IV contribute less than 1.5 per cent to the final straggling error.

Table VI gives a list of the errors in the 50- and 500-kev N in Be measurements. These errors are typical of all N and Ne range measurements. The errors in the Table, except for the last four, arise from the same sources as previously mentioned in the Kr in Be measurements. It is seen from the Table that although a liberal uncertainty has been assigned to each of the additional four sources, the net effect on the overall error is quite small.

Table VII gives the errors in the 50- and 500-kev N in Be range straggling measurements. The assigned errors are similar to those in Table V for Kr in Be except for $(n_I/n_T)_{max}$, I^tT/I^tI, and the factor "$\frac{1}{2}$" used in estimating the impurity concentration the incoming atoms see. It is seen that the uncertainties in these three parameters give a considerably larger uncertainty in the range straggling than in the actual range itself (Table VI). Once again it may be mentioned that these error assignments are typical of the assignments given to the other N and Ne straggling measurements.

The ion energies before correction for the surface layer were nominally assigned an uncertainty of less than one per cent. The uncertainty is quite likely much less than this, but occasionally the entrance slit to the analyzer was opened to ~3/16" in an attempt to get a better ion beam spot on the target blank. The surface correction itself is usually uncertain to about 60 per cent. The largest contribution to this uncertainty is the factor "$\frac{1}{2}$" used in estimating the surface layer thickness: an uncertainty of $\pm$ 50 per cent has been assigned to this factor on the basis that the surface layer thickness may not have increased uniformly as a function of time of ion bombardment. Other sources of error in the surface correction are: (1) uncertainty in $_I(dE/dx)_{\text{surface layer}}$ ($\pm$ 15--20 per cent for N in Be); and (2) uncertainty in the thickness of the layer resulting from the uncertainty in locating the midpoint of the target step in the profile immediately following the ion bombardment (7--16 per cent for N in Be). The uncertainties in the ion energies even after correction for the surface layer are still considerably less than the relative uncertainties in the range and range straggling measurements at these energies.

In Section III one must estimate dE/dR for the bombarding ion in the surface impurity layer and also estimate the range $_It_I$ in the embedded ions. We have consistently used a measured value of dE/dR in a target material multiplied by the ratio

$$(dE/dR)_{\text{unknown}} \; / \; (dE/dR)_{\text{target}}$$

obtained from Nielsen's theory. In view of our conclusion that the recent theory of Lindhard-Scharff more accurately describes the

stopping process than the Nielsen theory, one may ask whether errors have been introduced which might be removed by evaluating the ratio above from the Lindhard-Scharff theory. The two theories yield values of the ratio that differ by as much as 25 per cent. However, it can be seen from the previous paragraph that uncertainties in these corrections are always larger than 50 per cent. Even had the Lindhard-Scharff expression been available to us when these calculations were carried out, the difficulty of using numerical results instead of the analytical expression would suggest the use of Nielsen's theory as a good approximation for estimating these small corrections. It should be noted that electronic stopping, which is neglected in Nielsen's theory, is included in our value of dE/dR computed from the experiment.

Remarks similar to those of the preceding paragraph apply to the estimate ${}_{I}t_{I}$ used in the N and Ne measurements. The two theories yield values of ${}_{N}t_{N}/{}_{N}t_{C}$ and ${}_{Ne}t_{Ne}/{}_{Ne}t_{C}$ that differ by as much as 9 per cent, which is well within the assigned uncertainties in the ratios of $\pm$ 20 per cent.

V. RESULTS AND CONCLUSIONS

V.A. Comparison of Experimental Results with Theory.

The ranges and range straggling measured in this experiment are presented in Table VIII and in figs. 11-31. Qualitatively, the results indicate a linear range-energy dependence for Xe, Kr, and A ions in the target materials used in the experiment. The Ne and N range measurements indicate that $(dE/\rho dR)$ increases as a function of energy.

Comparison is made between the experimental ranges and the Bohr-Nielsen expression for the range (equation 26) over the energy region indicated in Section II.D for which a r^{-2} interaction potential would be expected to apply. In order to make a legitimate comparison between theory and experiment, however, it is necessary to consider the difference between the true path length and projected path length. Equation 36 relating R_p to R is used to modify equation 26 for the range, so that $t_p = t/(1 + \frac{1}{2.904}\frac{M_0}{M_1})$ is the value that is plotted as the heavy solid line for the "theoretical range" in figs. 11-18 for the Xe, Kr, and A ions. It is noticed that although a constant $(dE/\rho dR)$ is obtained experimentally and predicted theoretically, all the experimental ranges fall about 20 per cent below the theoretical predictions.

There were two major approximations used in Section II to obtain equation 26, and one would hope that by eliminating these approximations, better agreement with the experiment might be obtained. The first of these approximations is the use of $a = a_B/Z^{1/3}$ in the potential $V(r)/\epsilon = Z\epsilon e^{-R/a} R^{-1}$ for an atom of atomic number Z; a better approximation (Schiff, 1955) is $a = 0.885a_B/Z^{1/3}$. If a_B is replaced

by 0.885 a_B throughout, it is seen from equation 25 that the range is now increased by 11.5 per cent.

If one uses the potential energy given by equation 2 rather than the one given by equation 3 and approximates equation 2 by $V_2(r)=k_2/r^2$ as in Section II.D, one would again hope to obtain better agreement with experiment. The numerical calculation based upon this procedure for the case of Kr in Be, however, yields a range 10 per cent higher than that of equation 25 or 26. Thus, neither of these attempts to refine the theoretical expression brings about better agreement with the experiment.

Although it would also be desirable to make a comparison between the experimental range straggling results and the theoretical range straggling predicted by equation 29 for the r^{-2} potential, no rigorous comparison can, of course, be made since no treatment has been given for the projected range straggling $\Omega^2(R_p)$ in terms of $\Omega^2(R)$ along the path. It is pointed out at the end of Section II.G that Lindhard and Scharff (Lindhard, 1961a) state that $\Omega^2(R_p) \approx \Omega^2(R)$. The full width at half maximum predicted by the theory, $2\sqrt{2\ln 2\Omega^2(R)}$, is plotted as the heavy solid line in figs. 24-31 over the region of applicability of a r^{-2} potential. Fair agreement is obtained between theory and experiment. Any discrepancy may be due to: (1) the difference between $\Omega^2(R_p)$ and $\Omega^2(R)$, and/or (2) any contribution to dE/dx from electronic stopping, since range straggling from electron collisions would be negligible compared to that from nuclear collisions.

The range-energy relation of Lindhard and Scharff (Lindhard, 1961a) has been multiplied by the projection correction of equation 39 and plotted as dotted curves in figs. 11-18 for Xe, Kr, and A ions.

Although their projection correction (equation 39) applies only to a r^{-2} interaction potential, we have included it in the range-energy curve since the experimental measurements are projected range measurements. It is seen from figs. 11-18 that better agreement with the experiment is obtained by the Lindhard-Scharff expression than from expression 26; however, the theoretical ranges still appear to be systematically higher than the experimental ranges. The discrepancy may be due to energy loss of the ions to electrons in the stopping medium, since Lindhard and Scharff specifically state that the increased reduction in range due to energy loss to electrons may be of the order of 20 per cent.

An estimate of the electronic contribution to the stopping $(dE/dR)_{electronic}$ at low velocities can be made with the aid of equation 44 by setting $\xi_\epsilon = Z_1^{1/6}$ as suggested by Lindhard and Scharff (Lindhard, 1961a). The total energy loss is then

$$(dE/dR)_{total} = (dE/dR)_{electron} + (dE/dR)_{nuclear} ,$$

and the range is obtained by numerical integration of the resulting expression. For $(dE/dR)_{nuclear}$ we have used the values obtained by differentiating the range-energy curve of Lindhard and Scharff (Lindhard, 1961a).

Lindhard and Scharff's published curve, however, applies to only a small portion of the velocity region of this experiment, but Professor Lindhard has kindly furnished us with unpublished results (Lindhard, 1961b) which cover a considerably greater velocity region. The unpublished results include the electron stopping from equation 44.

The ranges obtained from the unpublished data are plotted as the dashed curves in figs. 11-22. The projection correction of equation 39 is once again included for Xe, Kr, and A ions, but is not included for Ne and N ions. It is seen that the agreement between experiment and Lindhard and Scharff's theory including electron excitation is generally quite good. Their latest estimate for the range appears to be better than equation 26, which neglects electron excitation.

It is also of interest to make a plot of dE/NdR vs. energy for neon and nitrogen ions for energies higher than those given by Lindhard and Scharff's unpublished data. These plots are indicated in fig. 32 and fig. 33. The solid curve, which represents the linear sum of the electronic and nuclear effects based on equations 44 and 43, respectively, is compared to the experimental stopping cross sections. The agreement between the theory and experiment appears to be fairly good.

V.B. Comparison with Other Experimental Results.

There are very few measurements of the range of heavy ions in solids in the kev energy region. Harvey's recent summary (Harvey, 1960) of low velocity ion ranges includes only one measurement in solids and two in gases with which we can make comparison.

Davies, et al., (Davies, 1960a, b; 1961a, b) have measured the range of 2- 50 kev Cs^{137}, Rb^{86}, and Na^{24} singly charged ions in Al. Their method is to bombard an Al target with radioactive alkali metal ions, and then determine the penetration depth by removing by electrolytic methods successive uniform layers of metal from the target and measuring the amount of radioactivity in each layer. Their

anodizing technique enables them to remove layers as thin as 1 $\mu gm/cm^2$. Their results give a linear range-energy curve for Cs^{137} and Na^{24} ions; for Rb^{86} ions they give only one range value--30 kev Rb^{86} in Al.

For 50 kev Cs^{137} in Al, they obtain a projected range of 9.5 $\mu gm/cm^2$. Our range for Xe^{131} in Al at 50 kev is 4.3 $\mu gm/cm^2$. Their value is as far above, as ours is below, the Lindhard-Scharff prediction including electron excitation and projection correction. For 30 kev Rb^{86} in Al, they obtain a projected range of 6.6 $\mu gm/cm^2$, which is 30 per cent larger than the Lindhard-Scharff prediction including projection correction and electron excitation.

A comparison of the ranges in solids and gases is of interest because of Lassen's observation (Lassen, 1951) that the range of fission fragments is shorter in solids than in gases. The results of Baulch and Duncan (Baulch, 1957) and of Valyocsik (Valyocsik, 1959) are given in Table IX. The measurements of Baulch appear to be in reasonable accord with the Lindhard-Scharff prediction, although at these low velocities, there is not too much difference between experiment and the prediction of equation 26. The Lindhard-Scharff prediction appears to be better than equation 26 for the Ra^{224} recoil measurements of Valyocsik, and is definitely better than equation 26 for the Th^{226} recoil measurements. The Th^{226} recoils are at a velocity comparable to the velocity of many of the ions of our experiment (420 kev Xe, 270 Kev Kr, and 130 kev A ions), and it is interesting that Valyocsik observes the same discrepancy between experiment and equation 26 that we do, and that good agreement between experiment and the Lindhard-Scharff theory is obtained. On the basis of this comparison we do not find evidence for significant difference between the stopping process in gases and solids.

APPENDIX I

INTERACTION ENERGY BETWEEN TWO ATOMS EACH DESCRIBED BY BOHR-TYPE POTENTIALS

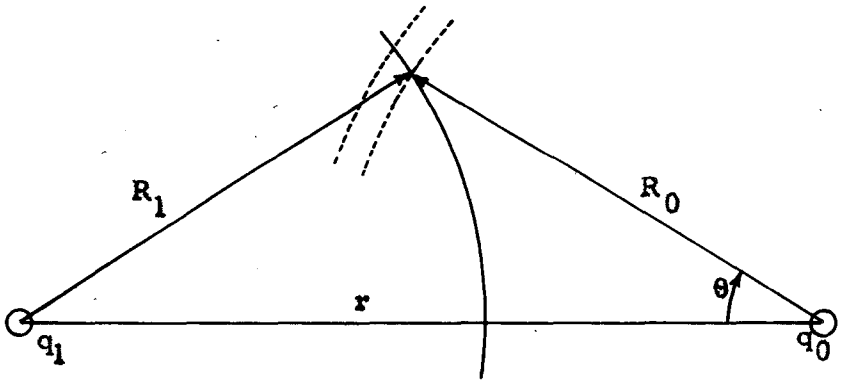

Let us take the potential of one charge distribution to be $\phi_1(R_1) = Z_1\epsilon R_1^{-1} \exp(-R_1 Z_1^{1/3}/a_B)$ and that of the second charge distribution to be $\phi_0(R_0) = Z_0\epsilon R_0^{-1}\exp(-R_0 Z_0^{1/3}/a_B)$. By Gauss' flux theorem we find the charge enclosed within a sphere of radius R_0 about the second charge distribution to be $q_0' = Z_0\epsilon\,(1+R_0 Z_0^{1/3}/a_B)\cdot\exp(-R_0 Z_0^{1/3}/a_B)$. The charge between a shell of radius R_0 and $R_0 + dR_0$ is then

$$\frac{dq_0'}{dR_0}\,dR_0 = -\,Z_0\epsilon R_0\left(\frac{Z_0^{1/3}}{a_B}\right)^2 e^{-R_0 Z_0^{1/3}/a_B}\cdot dR_0 \ ,$$

so that the charge density ρ_0' in a shell of radius R_0 and thickness dR_0 is

$$\rho_0' = \frac{dq_0'}{4\pi R_0^2\,dR_0} = -\,\frac{Z_0\epsilon}{4\pi R_0}\left(\frac{Z_0^{1/3}}{a_B}\right)^2 e^{-R_0 Z_0^{1/3}/a_B} \ .$$

The charge density ρ_0' is <u>negative</u> and is due to the electronic cloud surrounding the nucleus of the second atom. The total energy of interaction between the two atoms is then

$$V(r) = \int_{\theta=0}^{\theta=\pi} \int_{R_0=0}^{R_0=\infty} \frac{Z_1 \epsilon \, e^{-R_1 Z_1^{1/3}/a_B}}{R_1} \; x$$

$$x \left[\frac{-Z_0 \epsilon}{4\pi R_0} \left[\frac{Z_0^{1/3}}{a_B} \right]^2 e^{-R_0 Z_0^{1/3}/a_B} \right] 2\pi R_0^2 \sin\theta d\theta dR_0 \qquad \text{(AII)}$$

$$+ \frac{Z_1 \epsilon \, e^{-r Z_1^{1/3}/a_B}}{r} \quad (Z_0 \epsilon) \equiv V_-(r) + V_+(r)$$

where the second term gives the interaction energy between $\phi_1(R_1)$ and the positive nuclear charge $Z_0\epsilon$ at $R_1 = r$.

The integral in equation AII can be simplified by using $R_1^2 = R_0^2 + r^2 - 2R_0 r\cos\theta$ and replacing the θ variable by R_1 to obtain

$$V_-(r) = \frac{-Z_0 Z_1 \epsilon^2}{2r} \left[\frac{Z_0^{1/3}}{a_B} \right]^2 \left[\int_{R_0=0}^{R_0=r} \int_{R_1=r-R_0}^{R_1=r+R_0} e^{-R_1 Z_1^{1/3}/a_B} e^{-R_0 Z_0^{1/3}/a_B} dR_1 dR_0 \right. \qquad \text{(AI2)}$$

$$\left. + \int_{R_0=r}^{R_0=\infty} \int_{R_1=R_0-r}^{R_1=R_0+r} e^{-R_1 Z_1^{1/3}/a_B} e^{-R_0 Z_0^{1/3}/a_B} dR_1 dR_0 \right].$$

The integration is straightforward and yields

$$V_-(r) = \frac{+Z_1 Z_0 \epsilon}{r} \frac{Z_0^{2/3}}{Z_0^{2/3} - Z_1^{2/3}} \left[e^{-r Z_0^{1/3}/a_B} - e^{-r Z_1^{1/3}/a_B} \right] . \qquad \text{(AI3)}$$

Upon adding $V_+(r) = Z_0 Z_1 \epsilon^2 r^{-1} e^{-rZ_1^{1/3}/a_B}$ to equation AI 3 we obtain the final result

$$V(r) = V_-(r) + V_+(r)$$

$$= \frac{Z_1 Z_0 \epsilon^2}{r} \left[\frac{Z_0^{2/3} e^{-rZ_0^{1/3}/a_B} - Z_1^{2/3} e^{-rZ_1^{1/3}/a_B}}{Z_0^{2/3} - Z_1^{2/3}} \right], \qquad \text{(AI 4)}$$

which is the same as equation 2 in the text.

APPENDIX II

EVALUATION OF INTEGRALS INVOLVED IN DETERMINING $\overline{\Delta E}/\Delta R$ AND $\Omega^2(\Delta E)$

In order to evaluate the integral in equation 19, (see text) we make the substitution

$$x = \frac{\pi}{2\sqrt{1+p_c^2/p^2}} \tag{AII1}$$

and obtain

$$\int_0^\infty pdp \cos^2 \frac{\pi}{2\sqrt{1+p_c^2/p^2}} = 4\pi^2 p_c^2 \int_0^{\frac{\pi}{2}} \frac{x \cos^2 x dx}{(\pi^2 - 4x^2)^2} . \tag{AII2}$$

By decomposing $\frac{x}{(\pi^2 - 4x^2)^2} = \frac{x}{(\pi-2x)^2(\pi+2x)^2}$ into partial fractions, we obtain

$$4\pi^2 p_c^2 \int_0^{\frac{\pi}{2}} \frac{x \cos^2 x dx}{(\pi^2 - 4x^2)^2} = 4\pi^2 p_c^2 \int_0^{\frac{\pi}{2}} \left[\frac{\cos^2 x dx}{8\pi(\pi-2x)^2} - \frac{\cos^2 x dx}{8\pi(\pi+2x)^2} \right]. \tag{AII3}$$

Substituting $2y = \pi - 2x$ in the first term and $2y = \pi + 2x$ in the second term of equation AII 3, we obtain:

$$4\pi^2 p_c^2 \int_0^{\frac{\pi}{2}} \left[\frac{\cos^2 x dx}{8\pi(\pi-2x)^2} - \frac{\cos^2 x dx}{8\pi(\pi+2x)^2} \right] = \frac{4\pi^2 p_c^2}{32\pi} \left[\int_0^{\frac{\pi}{2}} \frac{\sin^2 y dy}{y^2} - \int_{\frac{\pi}{2}}^{\pi} \frac{\sin^2 y dy}{y^2} \right]. \tag{AII4}$$

The integral $\int_a^b \frac{\sin^2 y dy}{y^2}$ can be readily integrated by parts by the substitutions $u = \sin^2 y$ and $dv = dy/y^2$ to obtain

$$\int_a^b \frac{\sin^2 y dy}{y^2} = - \frac{\sin^2 y}{y} \Bigg|_a^b + Si(2b) - Si(2a), \tag{AII5}$$

where $\mathrm{Si}(x) = \int_0^x \frac{\sin x}{x}\,dx$. Using equation AII5 in AII4 we find, therefore, for the integral of equation AII2:

$$\int_0^\infty pdp\,\frac{\cos^2\pi}{2\sqrt{1+p_c^2/p^2}} = \frac{4\pi^2p_c^2}{32\pi}\left[-\frac{\sin^2 y}{y}\Bigg|_0^{\frac{\pi}{2}} + \mathrm{Si}(\pi) - \mathrm{Si}(0) + \frac{\sin^2 y}{y}\Bigg|_{\frac{\pi}{2}}^{\pi} - \mathrm{Si}(2\pi) + \mathrm{Si}(\pi)\right]$$

$$= \frac{\pi p_c^2}{8}\left[\frac{-4}{\pi} + 2\,\mathrm{Si}(\pi) - \mathrm{Si}(2\pi)\right], \qquad \text{(AII6)}$$

which, when substituted in equation 19 yields

$$\frac{\overline{\Delta E}}{\Delta R} = \frac{NT_m\pi^2p_c^2}{4}\left[\frac{-4}{\pi} + 2\mathrm{Si}(\pi) - \mathrm{Si}(2\pi)\right],$$

which is identical with equation 20 and is the desired result for $\overline{\Delta E}/\Delta R$.

To evaluate the integral in equation 23 for the energy straggling $\Omega^2(\Delta E)$, we make the substitution AIII along with the same decomposition into partial fractions as above to obtain:

$$\int_{p=0}^{p=\infty} pdp\,\cos^4\left[\frac{\pi}{2\sqrt{1+p_c^2/p^2}}\right] = 4\pi^2p_c^2\int_0^{\frac{\pi}{2}}\frac{x\cos^4 x\,dx}{(\pi^2-4x^2)^2}$$

$$= 4\pi^2p_c^2\int_0^{\frac{\pi}{2}}\left[\frac{\cos^4 x\,dx}{8\pi(\pi-2x)^2} - \frac{\cos^4 x\,dx}{8\pi(\pi+2x)^2}\right]$$

$$= \frac{4\pi^2p_c^2}{32\pi}\left[\int_0^{\frac{\pi}{2}}\frac{\sin^4 y\,dy}{y^2} - \int_{\frac{\pi}{2}}^{\pi}\frac{\sin^4 y\,dy}{y^2}\right], \qquad \text{(AII7)}$$

where the substitutions $2y = \pi - 2x$ in the first term and $2y = \pi + 2x$ in the second term of the second line were made as in the previous case. Now since $\sin^4 y = \sin^2 y\,(1-\cos^2 y) = \sin^2 y - \frac{\sin^2 2y}{4}$, we obtain in AII 7, along with the aid of equation AII 5:

$$\int_0^\infty \frac{p\,dp}{2\sqrt{1+p_c^2/p^2}}\cos^4\pi = \frac{4\pi^2 p_c^2}{32\pi}\left[\int_0^{\frac{\pi}{2}} \frac{\sin^2 y\,dy}{y^2} - \int_0^{\frac{\pi}{2}} \frac{\sin^2 2y\,dy}{4y^2}\right.$$

$$\left. - \int_{\frac{\pi}{2}}^{\pi} \frac{\sin^2 y\,dy}{y^2} + \int_{\frac{\pi}{2}}^{\pi} \frac{\sin^2 2y\,dy}{4y^2}\right]$$

$$= \frac{4\pi^2 p_c^2}{32\pi}\left[-\frac{\sin^2 y}{y}\Bigg|_0^{\frac{\pi}{2}} + \mathrm{Si}(\pi) - \mathrm{Si}(0)\right.$$

$$+ \frac{1}{2}\frac{\sin^2 y}{y}\Bigg|_0^{\pi} - \frac{1}{2}\mathrm{Si}(2\pi) + \frac{1}{2}\mathrm{Si}(0)$$

$$+ \frac{\sin^2 y}{y}\Bigg|_{\frac{\pi}{2}}^{\pi} - \mathrm{Si}(2\pi) + \mathrm{Si}(\pi)$$

$$\left. - \frac{1}{2}\frac{\sin^2 y}{y}\Bigg|_{\pi}^{2\pi} + \frac{1}{2}\mathrm{Si}(4\pi) - \frac{1}{2}\mathrm{Si}(2\pi)\right]$$

$$= \frac{\pi p_c^2}{8}\left[\frac{-4}{\pi} + 2\,\mathrm{Si}(\pi) - 2\,\mathrm{Si}(2\pi) + \frac{1}{2}\mathrm{Si}(4\pi)\right], \qquad \text{(AII 8)}$$

which, when substituted in equation 23 yields

$$\Omega^2(\Delta E) = \frac{\pi^2 N p_c^2 T_m^2 \Delta R}{4}\left[\frac{-4}{\pi} + 2\,\mathrm{Si}(\pi) - 2\,\mathrm{Si}(2\pi) + \frac{1}{2}\mathrm{Si}(4\pi)\right],$$

which is identical with equation 24 and is the desired result for $\Omega^2(\Delta E)$.

APPENDIX III

THICK TARGET SCATTERING YIELD FORMULAS

A. Target of Uniform Composition.

The scattering yield from a target of thickness dS is given by

$$N^k = N_{inc} \left[\frac{d\sigma}{d\Omega}(E_{1S},\ \theta_L)\right]_L^k \Omega_L n_k dS, \qquad \text{(AIII1)}$$

where N^k is the number of particles scattered at energy E_{1S} and laboratory angle θ_L into solid angle Ω_L for N_{inc} particles incident upon the target. The laboratory differential scattering cross section is

$$\left[\frac{d\sigma}{d\Omega}(E_{1S},\ \theta_L)\right]_L^k ,$$

and n_k is the number of type k scattering nuclei per unit volume. The magnetic spectrometer used in the experiment accepts particles whose energy lies in the region $E_{20} - dE_{20}$ to E_{20}, where $2E_{20}/dE_{20} \equiv R_c \sim 800$ is the known momentum resolution of the spectrometer. This spread in energies dE_{20} corresponds to a target lamina of thickness dS which presents a target of thickness $dS/\cos\theta_1$ to the incident proton beam. We desire to find the relation between $dS/\cos\theta_1$ and $dE_{20} = 2E_{20}/R_c$.

In order to do this we keep the incident particle energy E_{10} constant, increase the penetration depth beneath the surface of the target to $S + dS$, and calculate the corresponding decrease in energy dE_{20} at the spectrometer. This is illustrated in fig. 2. Particles scattered at C have an energy E_{2S} immediately after scattering and emerge from the target at A with energy E_{20}. Particles scattered at D have an energy $E_{2S} - \alpha_p (dE/dx)_{E_{1S}} \cdot (dS/\cos\theta_1)$ and emerge from the target at H with energy $E_{20} - dE_{20}$. Since ACDG is a parallelogram, the length HG is equal to $dS/\cos\theta_2$ and, as a result, the particle energy lost in

this length is ${}_p(dE/dx)_{E_{20}} \cdot (dS/\cos\theta_2)$; therefore, the particle energy at G is $E_{20} - dE_{20} + {}_p(dE/dx)_{E_{20}} \cdot (dS/\cos\theta_2)$. Since we are assuming for the moment that the target composition is uniform, the dashed parallel lines represent lines of equal energy. For example, the energy E_{20} at A is the same as that at F, and the scattered energy

$$E_{2S} - \alpha\, {}_p(dE/dx)_{E_{1S}} \cdot (dS/\cos\theta_1)$$

at D is the same as that at B. Therefore, the total energy lost by the particles in going from B to A is the same as that in going from D to F. The particle energy lost in $\overline{BC}$ is ${}_p(dE/dx)_{E_{2S}} \cdot (\overline{BC})$, which, since the energy at B is the same as that at D, is also equal to

$$\alpha\, {}_p(dE/dx)_{E_{1S}} \cdot (dS/\cos\theta_1) \quad .$$

Therefore,

$$(\overline{BC}) = \alpha\, {}_p(dE/dx)_{E_{1S}} \cdot (dS/\cos\theta_1) \Big/ {}_p(dE/dx)_{E_{2S}} . \qquad \text{(AIII 2)}$$

For a uniform target, however, $\overline{BC} = \overline{FG}$, and consequently the energy lost in $\overline{GF}$, to first order, is

$$(\Delta E)_{\overline{GF}} = {}_p(dE/dx)_{E_{20}} \cdot (\overline{GF}) = {}_p(dE/dx)_{E_{20}} \cdot (\overline{BC})$$

$$= \alpha \frac{{}_p(dE/dx)_{E_{20}}}{{}_p(dE/dx)_{E_{2S}}} \cdot p \left(\frac{dE}{dx}\right)_{E_{1S}} \cdot \frac{dS}{\cos\theta_1} . \qquad \text{(AIII 3)}$$

But since the energy at F is E_{20} and that at G is $E_{20} - dE_{20} + {}_p(dE/dx)_{E_{20}} \cdot (dS/\cos\theta_2)$, it follows from equation AIII 3 that

$$(\Delta E)_{GF} = E_{20} - [E_{20} - dE_{20} + {}_p(dE/dx)_{E_{20}} \cdot (dS/\cos\theta_2)]$$

$$= \frac{\alpha_p(\frac{dE}{dx})_{E_{20}} \cdot {}_p(\frac{dE}{dx})_{E_{1S}} \cdot \frac{dS}{\cos\theta_1}}{{}_p(\frac{dE}{dx})_{E_{2S}}} ,$$

and, as a result,

$$dS/\cos\theta_1 = dE_{20} \cdot \frac{{}_p(dE/dx)_{E_{2S}}}{{}_p(dE/dx)_{E_{20}}} \cdot \frac{1}{[\alpha_p(dE/dx)_{E_{1S}} + \frac{\cos\theta_1}{\cos\theta_2} \cdot {}_p(dE/dx)_{E_{2S}}]} . \quad \text{(AIII4)}$$

We have obtained, therefore, the relation between the energy dE_{20} over which the spectrometer accepts scattered particles and the effective target thickness $dS/\cos\theta_1$, inside the target and parallel to the incident beam, which corresponds to dE_{20}. The thick target scattering yield from atoms of type k in a homogeneous target is then:

$$N^k = (\frac{d\sigma}{d\Omega}(E_{1S}, \theta_L))^k_L \Omega_L \frac{2E_{20}}{R_c} \frac{CV}{ez} \times$$

$$\times \frac{1}{[\alpha_k \, {}_p\epsilon(E_{1S}) + \frac{\cos\theta_1}{\cos\theta_2} \, {}_p\epsilon(E_{2S})]} \cdot \frac{{}_p\epsilon(E_{2S})}{{}_p\epsilon(E_{20})} , \quad \text{(AIII5)}$$

where $CV/ez = N_{inc}$ is the number of particles incident upon the target during each counting operation; ${}_p\epsilon(E) = (1/n_k) \cdot \sum_j n_j \epsilon_j(E)$ is the total stopping cross section per scattering nucleus of type k, ϵ_j is the atomic stopping cross section of substance j, and n_j is the number of type j atoms per unit volume; and the remaining quantities were previously

defined in connection with equation AIII1. The scattering yield formula AIII5 was first derived in this form by Wenzel (Wenzel, 1952) by differentiating equation 47, Section III.C, with respect to $dS/\cos\theta_1$. Equation AIII5 above agrees with the expressions of Rubin (Rubin, 1959) and of Brown, et al., (Brown, 1951) for S very nearly equal to zero, i.e., for surface observations.

B. Targets of Non-uniform Composition.

For a target of continuously varying composition, we approximate the actual physical situation by dividing the target into ℓ layers of uniform composition. The composition varies from layer to layer, and the width of each layer is S/ℓ centimeters. The spread in energy of the particles coming from the last layer is then given by equation AIII4, viz.,

$$dE_{2(S-S/\ell)} = \frac{{}_p(\frac{dE}{dx})^{(S)}_{E_{2(S-S/\ell)}}}{{}_p(\frac{dE}{dx})^{(S)}_{E_{2S}}} \cdot \left[\alpha_p(\frac{dE}{dx})^{(S)}_{E_{1S}} + \frac{\cos\theta_1}{\cos\theta_2}\, {}_p(\frac{dE}{dx})^{(S)}_{E_{2S}} \right] \cdot \frac{dS}{\cos\theta_1} , \quad \text{(AIII6)}$$

where ${}_p(\frac{dE}{dx})^{(S)}$ refers to the rate of particle energy loss in the layer between S and $S-S/\ell$. In order to find the spread in energy $dE_{2(S-2S/\ell)}$ of the particles coming from the next-to-last layer we refer to the following diagram:

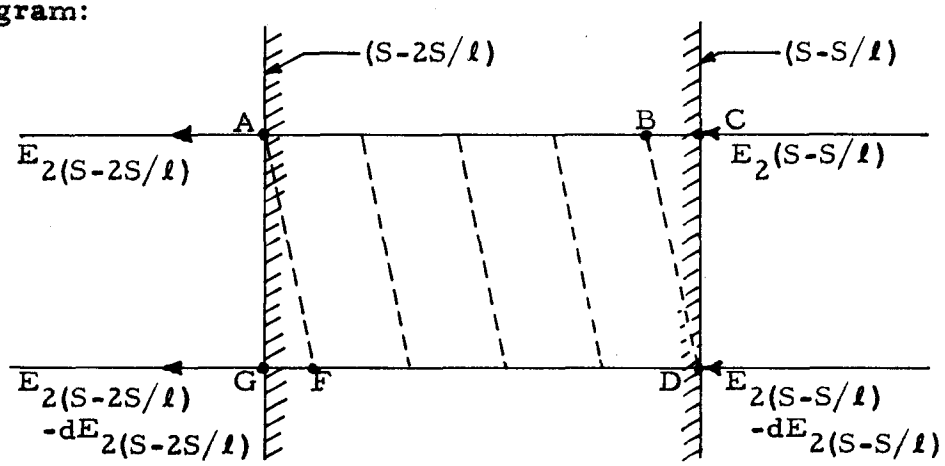

The particles entering the next-to-last layer at $S-S/\ell$ with energy $E_{2(S-S/\ell)}$ leave this layer with energy $E_{2(S-2S/\ell)}$, whereas those entering with energy $E_{2(S-S/\ell)} - dE_{2(S-S/\ell)}$ leave with energy $E_{2(S-2S/\ell)} - dE_{2(S-2S/\ell)}$. As in fig. 2 the dashed slanted lines represent lines of equal energy, so that the energy lost in $\overline{AB}$ is the same as that in $\overline{FD}$. Consequently, the energy lost in $\overline{BC}$ is $dE_{2(S-S/\ell)} = p\left(\frac{dE}{dx}\right)^{(S-S/\ell)}_{E_{2(S-S/\ell)}} \cdot (\overline{BC})$, and that lost in $\overline{FG}$ is $dE_{2(S-2S/\ell)} = p\left(\frac{dE}{dx}\right)^{(S-S/\ell)}_{E_{2(S-2S/\ell)}} \cdot (\overline{FG})$. Since $\overline{FG} = \overline{BC}$, it follows that

$$dE_{2(S-2S/\ell)} = \frac{p\left(\frac{dE}{dx}\right)^{(S-S/\ell)}_{E_{2(S-2S/\ell)}}}{p\left(\frac{dE}{dx}\right)^{(S-S/\ell)}_{E_{2(S-S/\ell)}}} \cdot \frac{p\left(\frac{dE}{dx}\right)^{(S)}_{E_{2(S-S/\ell)}}}{p\left(\frac{dE}{dx}\right)^{(S)}_{E_{2S}}} \times$$

$$\times \left[\alpha \; p\left(\frac{dE}{dx}\right)^{(S)}_{E_{1S}} + \frac{\cos\theta_1}{\cos\theta_2} \; p\left(\frac{dE}{dx}\right)^{(S)}_{E_{2S}} \right] \cdot \frac{dS}{\cos\theta_1} , \qquad \text{(AIII7)}$$

where use has been made of equation AIII6. Each succeeding layer will contribute a factor of the form

$$p\left(\frac{dE}{dx}\right)^{(S-\mu S/\ell)}_{E_{2[S-(\mu+1)S/\ell]}} \Bigg/ p\left(\frac{dE}{dx}\right)^{(S-\mu S/\ell)}_{E_{2(S-\mu S/\ell)}} ,$$

so that we obtain for dE_{20}:

$$dE_{20} = \frac{dS}{\cos\theta_1} \left\{ \prod_{i=0}^{\ell-1} \frac{p\left(\frac{dE}{dx}\right)^{[(i+1)S/\ell)}_{E_{2(iS/\ell)}}}{p\left(\frac{dE}{dx}\right)^{[(i+1)S/\ell]}_{E_{2[(i+1)S/\ell]}}} \right\} \cdot \left[\alpha \; p\left(\frac{dE}{dx}\right)^{(S)}_{E_{1S}} + \frac{\cos\theta_1}{\cos\theta_2} \, p\left(\frac{dE}{dx}\right)^{(S)}_{E_{2S}} \right] .$$

(AIII8)

Obviously, the larger ℓ is chosen to be, the more nearly equation AIII8 will approximate the actual physical situation. In the present experiment we are concerned with embedded impurity atoms whose concentration is a function of depth beneath the surface of a target which before the ion bombardment was of uniform composition, and it becomes convenient to write $_p(\frac{dE}{dx})$ in the layer between iS/ℓ and $(i+1)S/\ell$ as:

$$p\left(\frac{dE}{dx}\right)^{(i+1)S/\ell}_{E_{2(\mu S/\ell)}} = n_T^{(i+1)S/\ell} \; {}_p\epsilon_T(E_{2(\mu S/\ell)}) \; x$$

$$x\left[1 + \frac{n_I^{(i+1)S/\ell}}{n_T^{(i+1)S/\ell}} \cdot \frac{{}_p\epsilon_I(E_{2(\mu S/\ell)})}{{}_p\epsilon_T(E_{2(\mu S/\ell)})}\right], \qquad \text{(AIII9)}$$

where μ is either i or i+1, and subscripts I and T refer to the embedded impurity atoms and target atoms, respectively. If the ratio $_p\epsilon_I(E)/_p\epsilon_T(E)$ is independent of energy over the energy region of interest, then all the product terms in equation AIII8 vanish except the first and last leaving:

$$dE_{20} = \frac{dS}{\cos\theta_1} \frac{{}_p\epsilon_T(E_{20})}{{}_p\epsilon_T(E_{2S})} \; x$$

$$x\left\{\alpha\left[n_T^S \, {}_p\epsilon_T(E_{1S}) + n_I^S \, {}_p\epsilon_I(E_{1S})\right] + \frac{\cos\theta_1}{\cos\theta_2}\left[n_T^S \, {}_p\epsilon_T(E_{2S}) + n_I^S \, {}_p\epsilon_I(E_{2S})\right]\right\}. \qquad \text{(AIII10)}$$

If the target prior to the ion bombardment consisted of more than one atomic substance we would replace $n_T^S \cdot {}_p\epsilon_T(E_S)$ by $\sum_j n_{Tj}^S \, {}_p\epsilon_{Tj}(E_S)$. We can now write the thick target yield formula AIII5 in the following form which applies to a target of continuously varying composition:

$$N^{\nu} = \left(\frac{d\sigma}{d\Omega}\left(E_{1S}^{\nu}\right)\right)_L^{\nu} \Omega_L \frac{2E_{20}}{R_c} \cdot \frac{CV}{ez} \cdot \frac{{}_p\epsilon_T\left(E_{2S}^{\nu}\right)}{{}_p\epsilon_T\left(E_{20}\right)} \times$$

(AIII11)

$$\times \frac{n_{\nu}^{S}}{\left\{\alpha_{\nu}\left[n_T^S\, {}_p\epsilon_T(E_{1S}^{\nu}) + n_I^S\, {}_p\epsilon_I(E_{1S}^{\nu})\right] + \frac{\cos\theta_1}{\cos\theta_2}\left[n_T^S\, {}_p\epsilon_T(E_{2S}^{\nu}) + n_I^S\, {}_p\epsilon_I(E_{2S}^{\nu})\right]\right\}} .$$

If the scattering occurs from the embedded impurity atoms then we use ν = "I" throughout expression AIII11, whereas we use ν = "T" throughout if the scattering is from the target atoms.

It must be remembered that expression AIII11 implicitly contains the assumption that ${}_p\epsilon_I(E)/{}_p\epsilon_T(E)$ is independent of energy throughout the energy region of interest. If this assumption is not valid, then an approximate treatment based on equation AIII8 would be more appropriate.

APPENDIX IV

DETERMINATION OF INTERMEDIATE ENERGY E_p USED IN EVALUATING PROTON STOPPING CROSS SECTIONS

Let us assume that we have a homogeneous foil consisting of two atomic substances. If the stopping power of each atomic substance can be represented by $-_p(dE/dx) = kE^{-\gamma}$, then the thickness of the foil, Δx, traversed by the protons is given by

$$\Delta x = \int_{E_f}^{E_i} \frac{dE}{-_p(dE/dx)} = \int_{E_f}^{E_i} \frac{dE}{k_1/(E/E_a)^{\gamma_1} + k_2/(E/E_a)^{\gamma_2}} , \qquad \text{(AIV1)}$$

where E_i and E_f are the initial and final proton energies, and E_a is some intermediate energy $E_f < E_a < E_i$. We define E_p as the proton energy for which $(E_i-E_f)/(\Delta x)$ is actually $-_p(dE/dx)\Big|_{E_p}$. Then

$$\int_{E_f}^{E_a} \frac{dE}{k_1/(E/E_a)^{\gamma_1}+k_2/(E/E_a)^{\gamma_2}} + \int_{E_a}^{E_i} \frac{dE}{k_1/(E/E_a)^{\gamma_1}+k_2/(E/E_a)^{\gamma_2}} = \frac{E_i-E_f}{k_1/(E_p/E_a)^{\gamma_1}+k_2/(E_p/E_a)^{\gamma_2}} . \qquad \text{(AIV2)}$$

If $E_p > E_a$ and $\gamma_1 > \gamma_2$, an inequality can be established by replacing γ_1 by γ_2 in the first integral, γ_2 by γ_1 in the second integral, and γ_1 by γ_2 on the right hand side of equation AIV2 to obtain

$$\left[\frac{E_i^{\gamma_1+1}}{E_a^{\gamma_1}(\gamma_1+1)} - \frac{E_a}{\gamma_1+1} + \frac{E_a}{\gamma_2+1} - \frac{E_f^{\gamma_2+1}}{E_a^{\gamma_2}(\gamma_2+1)}\right] > \frac{(E_i-E_f)E_p^{\gamma_2}}{E_a^{\gamma_2}} . \qquad \text{(AIV3)}$$

By defining $E_a = (E_i+E_f)/2$ and $(\Delta E)_{Av} = E_i-E_f$, we can make a power series expansion in $(\Delta E)_{Av}/E_a$ to obtain

$$E_p < E_a\left\{1 + \frac{1}{8}\left(\frac{\gamma_1}{\gamma_2} - 1\right)\frac{(\Delta E)_{Av}}{E_a} + \left[\frac{\gamma_1(\gamma_1-1)+\gamma_2(\gamma_2-1)}{48\gamma_2} + \frac{1}{\gamma_2}\left(\frac{1}{\gamma_2}-1\right)\frac{(\gamma_1-\gamma_2)^2}{128}\right]\left(\frac{(\Delta E)_{Av}}{E_a}\right)^2 + \cdots\right\} \quad \text{(AIV4)}$$

If $E_p < E_a$, we can establish another inequality by replacing γ_2 by γ_1 in the first integral, γ_1 by γ_2 in the second integral, and γ_1 by γ_2 on the right hand side of equation AIV2 to obtain the same result as expression AIV3 except with the inequality sign reversed and γ_2 and γ_1 interchanged on the left hand side of the inequality. A power series expansion of the resulting expression yields

$$E_p > E_a\left\{1 - \frac{1}{8}\left(\frac{\gamma_1}{\gamma_2} - 1\right)\frac{(\Delta E)_{Av}}{E_a} + \left[\frac{\gamma_1(\gamma_1-1)+\gamma_2(\gamma_2-1)}{48\gamma_2} + \frac{1}{\gamma_2}\left(\frac{1}{\gamma_2}-1\right)\frac{(\gamma_1-\gamma_2)^2}{128}\right]\left(\frac{(\Delta E)_{Av}}{E_a}\right)^2 + \cdots\right\} \quad \text{(AIV5)}$$

Expressions AIV4 or AIV5 reduce to expression 51 of the text when $\gamma_1 = \gamma_2$. The inequalities establish limits on the intermediate proton energy E_p used in evaluating the proton stopping cross sections in equation 61 of the text. The most extreme case, that of 500 kev nitrogen in aluminum, indicated an uncertainty of $\pm$ 2.3 kev in E_a as the estimate for E_p. It is felt, however, that E_a is still a good estimate since, as has been mentioned before, the proton stopping cross section curves can be read in the vicinity of 300 kev (see Table III) only to within $\approx \pm 2$ kev.

REFERENCES

1. M. Bader, R. E. Pixley, F. S. Mozer, and W. Whaling, 1956, Phys. Rev. 103, 32.

2. R. K. Bardin, 1961, Ph. D. Thesis, California Institute of Technology.

3. D. L. Baulch and J. F. Duncan, 1957, Australian J. Chem. 10, 112.

4. H. A. Bethe, 1930, Ann. Physik, 5, 325.

5. H. Bichsel, R. F. Mozley, and W. A. Aron, 1957, Phys. Rev. 105, 1788.

6. F. Bloch, 1933, Ann. Physik, 16, 285.

7. D. Bohm, 1951, Quantum Theory (Prentice-Hall, Inc., New York), p. 506.

8. N. Bohr, 1913, Phil. Mag., 25, 10.

9. N. Bohr, 1948, Kgl. Danske Videnskab. Selskab., Mat.-fys. Medd., 18, No. 8.

10. R. O. Bondelid and C. A. Kennedy, 1959, Phys. Rev. 115, 1601.

11. A. B. Brown, C. W. Snyder, W. A. Fowler, and C. C. Lauritsen, 1951, Phys. Rev. 82, 159.

12. A. B. Chilton, J. N. Cooper, and J. C. Harris, 1954, Phys. Rev., 93, 413.

13. J. A. Davies, J. Friesen, and J. D. McIntyre, 1960a, Can. J. Chem. 38, 1526.

14. J. A. Davies, J. D. McIntyre, R. L. Cushing, and M. Lounsbury, 1960b, Can. J. Chem. 38, 1535.

15. J. A. Davies and G. A. Sims, 1961a, Can. J. Chem. 39, 601.

16. J. A. Davies, J. D. McIntyre, and G. A. Sims, 1961b, Can. J. Chem. 39, 611.

17. E. Fermi and E. Teller, 1947, Phys. Rev. 72, 399.

18. E. Fermi, 1950, Nuclear Physics, Notes compiled by J. Orear, A. H. Rosenfeld, R. A. Schluter (University of Chicago Press), p. 52.

19. M. I. Guseva, E. V. Inopin, and S. P. Tsytko, 1959, Soviet Physics JETP, 9, 1.

20. B. G. Harvey, 1960, in Annual Review of Nuclear Science, Vol. 10, p. 235.

21. H. H. Heckman, B. L. Perkins, W. G. Simon, F. M. Smith, and W. G. Barkas, 1960, Phys. Rev. 117, 544.

22. E. Jahnke and F. Emde, 1945, Tables of Functions (Dover Publications, New York), p. 6.

23. J. Knipp and E. Teller, 1941, Phys. Rev. 59, 659.

24. N. O. Lassen, 1951, Kgl. Danske Videnskab. Selskab., Mat.-fys. Medd., 26, No. 5.

25. J. Lindhard and M. Scharff, 1961a, To be published in Physical Review Letters.

26. J. Lindhard, 1961b, Private Communication.

27. C. B. Madsen and P. Venkateswarlu, 1948, Phys. Rev. 74, 1782.

28. H. S. W. Massey and E. H. S. Burhop, 1952, Electronic and Ionic Phenomena, (Oxford University Press, New York), p. 373.

29. C. Mileikowsky, 1954, Ark. Fys., 7, No. 8.

30. C. D. Moak, H. Reese, Jr., and W. M. Good, 1951, Nucleonics, 9 (3), 20.

31. K. O. Nielsen, 1956, in Electromagnetically Enriched Isotopes and Mass Spectrometry, Ed. by. M. L. Smith (Academic Press, New York), p. 68.

32. L. C. Northcliffe, 1960, Phys. Rev. 120, 1744.

33. J. C. Overley, 1961, Ph. D. Thesis, California Institute of Technology.

34. R. E. Pixley, 1957, Ph. D. Thesis, California Institute of Technology.

35. D. I. Porat and K. Ramavataram, 1960, Proc. Phys. Soc., 76, 438.

36. H. K. Reynolds, 1953, Ph. D. Thesis, California Institute of Technology.

37. S. Rubin, 1959, Nuclear Instruments and Methods, 5, 177.

38. L. I. Schiff, 1955, Quantum Mechanics (McGraw-Hill Book Co., Inc., New York), p. 281.

39. F. Seitz and J. S. Koehler, 1956, Solid State Physics, Ed. by F. Seitz and D. Turnbull (Academic Press, New York), p. 340.

40. C. W. Snyder, S. Rubin, W. A. Fowler, and C. C. Lauritsen, 1950, Rev. Sci. Inst., 21, 852.

41. S. Thulin, 1955, Ark. Fys., 9, 107.

42. E. W. Valyocsik, 1959, U. S. Atomic Energy Document, UCRL-8855.

43. W. A. Wenzel, 1952, Ph. D. Thesis, California Institute of Technology.

44. W. Whaling, 1958, in Handbuch der Physik, (J. Springer Verlag, Berlin), Vol. 34, p. 193.

TABLE I. ION BEAM DATA (See pp. 27, 42, 46, text)

Ion and target	Ion beam current (μ amp)	Total ion charge deposited** (μ coul/cm^2)	Concentration of embedded ions in target (n_I/n_T) (max)	(min)
N in Be	1.5--4.5	19,650--39,300$^+$	1/3.9	1/11
N in C	0.4--4.5	19,650--39,300$^+$	1/1.6	1/9
N in Al	(*)--1.0	23,100--46,200$^+$	1/1.6	1/10
Ne in Be	0.25-3.0	8,400--11,800	1/6.4	1/34
Ne in C	(*)--1.0	5,900--8,400	1/12	1/22
A in Be	0.4--3.0	1960	1/46	1/129
A in C	0.4--4.0	1,960--2,800	1/26	1/85
A in B^{10}	(*)--1.5	1,240--4,400	1/45	1/192
A in B	(*)--1.5	1,240--4,400	1/25	1/97
Kr in Be	(*)--1.5	350--700	1/322	1/915
Kr in Al	(*)--0.8	880--1050	1/22	1/132
Xe in Be	(*)--0.4	350--530	1/86	1/229
Xe in Al	(*)-0.25	530	1/30	1/63

* (Not measurable on meter)

$^+$ (Molecular ion beam $(NN)^+$ used for 50--200 kev; atomic ion beam $(N)^+$ used for 300--500 kev)

** (The ion charge is not necessarily deposited uniformly over the target area exposed to the ion beam. The subsequent proton bombardments (for the different ion energies) therefore encounter different concentrations of embedded atoms in the target. The maximum and minimum concentrations of embedded atoms as determined from analysis of the proton data are given in the last column of the Table.)

TABLE II. TARGET IMPURITIES

Target	Target impurity (per cent)
Beryllium	Oxygen ~ 1; Aluminum ~ 0.2
Carbon	Oxygen ~ 3; Aluminum or silicon ~ 0.5
Aluminum alloy 6061	Iron, Copper and/or Manganese ~ 2
Aluminum alloy EC1100	Iron, Copper and/or Manganese ~ 0.4
Boron 10; Natural boron	Negligible

TABLE III. DEPENDENCE OF PROTON STOPPING POWER UPON ENERGY ASSUMING $-dE/dx = k/E^{\gamma}$ BEHAVIOR

Ion and target	Proton energy region used in range and range straggling calculations (kev)	γ_I	γ_T	$\gamma_T - \gamma_I$
N in C	195--380	0.564	0.564	0
N in Be	295--470	0.618	0.582	-0.036
N in Al	225--370	0.622	0.398	-0.224
Ne in C	225--360	0.395	0.592	+0.197
Ne in Be	295--470	0.480	0.534	+0.054

Table II: Target impurities as determined by the elastic scattering of protons from the targets. The impurities listed are in reasonable agreement with the manufacturer's specifications except for aluminum alloy 6061 where the combined impurities of silicon and magnesium were listed at ~ 1.5 per cent by the manufacturer. The impurities were not seen in the elastic scattering momentum profiles. See p. 29, text.

Table III: Dependence of proton stopping power upon energy by assuming $-dE/dx = k/E^{\gamma}$ behavior for the ions and targets used in the neon and nitrogen range measurements. The second column gives the proton energy region used in the range and range straggling calculations. The values of γ_I and γ_T are obtained from Whaling's compilation of stopping cross sections (Whaling, 1958). See p. 45, text.

TABLE IV. ERRORS IN KRYPTON IN BERYLLIUM RANGE MEASUREMENTS

Possible sources of error	Amount of error (%)	% Error introduced in final value of range
E_{10} Location of peak in profile	$\pm$0.27--$\pm$1.2	$\pm$13.0--$\pm$5.54
E_{20} Spectrometer drift	$\pm$0.15	$\pm$6.6--$\pm$0.64
E_{10} Electrostatic analyser drift	< 0.15	<6.4-- 0.67
E_{10}, E_{20} Electrostatic analyser calibration	< 0.2	< 0.3
E_{10}, E_{20} Uncertainty in surface contaminant correction	$\pm$20 -- $\pm$40	$\pm$1.95--$\pm$1.3
$\cos\theta_1$ Uncertainty in θ_1	$\pm$0.88	$\pm$0.37
$\cos\theta_2$ Uncertainty in θ_2	$\pm$0.92	$\pm$0.48
p^{ϵ} Uncertainty in p^{ϵ}'s	$\pm$3.0	$\pm$3.0
α Uncertainty in θ_L	$\pm$0.42	$\pm$2.0--$\pm$0.23
Presence of impurity atoms	negligible	negligible
TOTAL PROBABLE ERROR: $\pm$17.2%--$\pm$6.6%		

Table IV: Errors in krypton in beryllium range measurements. The errors are typical of all the xenon, krypton, and argon measurements. Column 1 lists the source of error, column 2 the estimated uncertainty in the source expressed as a probable error, and column 3 the probable error introduced in the final value of the range. The values listed are for the 50- and 500-kev measurements; there is usually a decreasing per cent of error with increasing ion energy. The total probable error is obtained by taking the square root of the sum of the squares of the individual errors. See p. 57, text.

TABLE V. ERRORS IN KRYPTON IN BERYLLIUM STRAGGLING MEASUREMENT

Possible sources of error		Amount of error (%)	% Error introduced in final value of straggling
E_{10}^{LHM}	Location of lower half maximum of peak in profile	±0.21--±1.19	±15.3--±15.7
E_{10}^{UHM}	Location of upper half maximum of peak in profile	±0.27--±1.11	±20.2--±16.3
E_{10}^{LHM}, E_{10}^{UHM}	Uncertainty in σ inst	±40	±7.4--±0.13
E_{10}^{LHM}, E_{10}^{UHM}	Uncertainty in σ prot stragg	±50 -- ±30	±21.6--±3.96
E_{10}^{LHM}, E_{10}^{UHM}	Amount of impurity atoms deposited		~ 5
$_p\epsilon$	Uncertainty in $_p\epsilon$'s	±3.0	±3.0
All other sources listed in Table IV			< 1.5
TOTAL PROBABLE ERROR ASSIGNED: ±35%--±24%			

Table V: Errors in krypton in beryllium range straggling measurements. The errors are typical of all the xenon, krypton, and argon range straggling measurements. Column 1 lists the source of error, column 2 the estimated uncertainty in the source expressed as a probable error, and column 3 the probable error introduced in the final value of the range straggling. The values listed are for the 50- and 500-kev measurements; there is usually a decreasing per cent of error with increasing ion energy. The total probable error is obtained by taking the square root of the sum of the squares of the individual errors. See p. 58, text.

TABLE VI. ERRORS IN NITROGEN IN BERYLLIUM RANGE MEASUREMENTS

Possible sources of error		Amount of error (%)	% Error introduced in final value of range
E_{10}	Location of peak in profile	$\pm$0.52--$\pm$0.61	$\pm$7.6--$\pm$1.93
E_{20}	Spectrometer drift	$\pm$0.21	$\pm$2.52--$\pm$0.40
E_{10}	Electrostatic analyzer drift	0.2	2.2--$\pm$0.34
E_{10}, E_{20}	Electrostatic analyzer calibration	0.2	0.3
E_{10}, E_{20}	Uncertainty in surface contaminant correction	$\pm$ 20	$\pm$3.10--$\pm$0.84
$Cos\theta_1$	Uncertainty in θ_1	$\pm$0.88	$\pm$0.35
$Cos\theta_2$	Uncertainty in θ_2	$\pm$0.95	$\pm$0.60
$_p\epsilon$	Uncertainty in $_p\epsilon$'s	$\pm$3.0	$\pm$3.0
	Uncertainty in θ_L	$\pm$0.2	$\pm$2.74--$\pm$0.61
$E_{10}^{[1]}$	Uncertainty of incident energy at region 1 - region 2 interface	$\pm$0.21--$\pm$0.80	$\pm$0.13--$\pm$0.12
$(n_I/n_T)_{max}$	Uncertainties in $(d\sigma/d\Omega)^N$, $\Delta\Omega/R_c$, and in using $\frac{1}{2}(n_I/n_T)_{max}$ as "average" impurity concentration in region 2	$\pm$ 50	$\pm$1.65--$\pm$0.94
$(_It_T/_It_I)$	Uncertainty in $_It_I$	$\pm$ 20	$\pm$0.32--$\pm$0.20
Uncertainty in factor "$\frac{1}{2}$" used in estimating how many embedded atoms the incoming atoms see		$\pm$ 50	$\pm$0.81--$\pm$0.51
TOTAL PROBABLE ERROR: $\pm$10%--$\pm$4%			

Table VI: Errors in nitrogen in beryllium range measurements. The errors are typical of the nitrogen and neon measurements. Column 1 lists the source of error, column 2 the estimated uncertainty in the source expressed as a probable error, and column 3 the probable error introduced in the final value of the range. The values listed are for the 50- and 500-kev measurements; there is usually a decreasing per cent of error with increasing ion energy. The total probable error is obtained by taking the square root of the sum of the squares of the individual errors. See p. 59, text.

TABLE VII. ERRORS IN NITROGEN IN BERYLLIUM STRAGGLING MEASUREMENT

Possible sources of error		Amount of error (%)	% Error introduced in final value of straggling
E_{10}^{LHM}	Location of lower half maximum in profile	±0.21--±0.80	±8.78--±24.8
E_{10}^{UHM}	Location of upper half maximum in profile	±0.26--±0.61	±9.27--±17.7
E_{10}^{LHM}, E_{10}^{UHM}	Uncertainty in σ_{inst}	± 35	±1.93--±0.74
E_{10}^{LHM}, E_{10}^{UHM}	Uncertainty in σ prot stragg	± 50--± 30	±7.5--±12.9
$_p\epsilon$	Uncertainty in $_p\epsilon$'s	±3.0	±3.0
$(n_I/n_T)_{max}$	Uncertainties in $(d\sigma/d\Omega)^N$, $\Delta\Omega/R_c$, and in using $3/4 \cdot (n_I/n_T)_{max}$ as "average" impurity concentration in region 3	± 33	±5.4--±8.48
$(_It_T/_It_I)$	Uncertainty in $_It_I$	± 20	±1.10--±2.40
Uncertainty in factor "$\frac{1}{2}$" used in estimating how many embedded atoms the incoming atoms see		± 50	±2.74--±6.02
All other sources listed in Table VI.			< 3.0

TOTAL PROBABLE ERROR ASSIGNED: ±16.7%--±35.0%

Table VII: Errors in nitrogen in beryllium range straggling measurements. The errors are typical of all nitrogen and neon range straggling measurements. Column 1 lists the source of error, column 2 the estimated uncertainty in the source expressed as a probable error, and column 3 the probable error introduced in the final value of the range straggling. The values listed are for the 50- and 500-kev measurements; there is usually a decreasing per cent of error with increasing ion energy. The total probable error is obtained by taking the square root of the sum of the squares of the individual errors. See p. 59, text.

TABLE VIII. EXPERIMENTAL RANGE AND RANGE STRAGGLING MEASUREMENTS

Ion and Target	Ion Energy (kev)	Range (μ gm/cm^2)	Range Straggling (μ gm/cm^2)
Xe in Be	32.4 ± 9.4	4.3 ± 1.2	4.4 ± 1.1
	100.3	9.4 ∓ 1.0	6.0 ∓ 1.1
	200.5	17.3 ± 1.2	10.1 ± 1.3
	300.8	24.0 ∓ 1.8	12.1 ∓ 1.7
	401.0	32.0 ∓ 2.0	21.3 ∓ 1.8
	501.3	41.1 ∓ 5.1	19.3 ∓ 1.9
Xe in Al	50.1	4.3 ± 0.9	4.4 ± 1.5
	100.3	7.7 ∓ 1.4	11.3 ± 1.5
	200.5	15.2 ± 2.0	17.7 ∓ 2.0
	300.8	22.8 ∓ 2.8	30.9 ∓ 3.3
	401.0	36.6 ∓ 3.3	33.7 ∓ 3.2
	501.3	43.7 ∓ 4.9	30.3 ∓ 6.0
Kr in Be	45.9 ± 3.0	5.8 ± 1.0	3.9 ± 1.3
	96.0 ∓ 3.2	10.6 ± 1.5	8.7 ∓ 1.1
	196.2 ± 3.6	23.4 ∓ 2.3	16.6 ± 2.0
	295.6 ∓ 4.2	35.5 ∓ 3.7	21.1 ∓ 3.4
	395.6 ∓ 5.0	48.2 ∓ 4.4	28.4 ∓ 4.6
	495.6 ∓ 5.8	60.7 ∓ 4.0	26.4 ∓ 6.2
Kr in Al	50.1	5.0 ± 1.4	6.9 ± 2.1
	100.3	9.1 ∓ 2.2	15.3 ± 1.8
	200.5	19.2 ± 1.7	19.0 ∓ 3.1
	300.8	35.2 ∓ 4.0	28.5 ∓ 3.9
	401.0	47.4 ∓ 6.4	38.9 ∓ 6.5
	501.3	56.1 ∓ 7.6	45.2 ∓ 8.9
A in Be	48.5 ± 1.0	8.7 ± 2.2	8.2 ± 1.2
	98.6 ∓ 1.4	18.5 ± 2.0	14.2 ± 1.7
	198.8 ± 2.1	36.0 ∓ 3.3	21.0 ∓ 2.5
	298.0 ∓ 3.3	56.7 ∓ 4.0	25.7 ∓ 3.7
	396.9 ∓ 4.3	72.8 ∓ 5.0	30.9 ∓ 4.5
	500.2	97.3 ∓ 6.5	37.8 ∓ 5.0
A in B^{10}	44.7 ± 3.0	8.2 ± 1.0	3.0 ± 1.4
	99.6 ∓ 1.1	15.9 ± 2.0	12.4 ± 2.4
	300.2	50.0 ∓ 3.9	22.9 ∓ 2.7
	500.2	82.4 ∓ 7.3	26.7 ∓ 8.7

Table VIII: The table gives the experimental range and range straggling measurements in μ gm/cm^2. The range straggling given in the table is the full width at half maximum of the impurity atom distributions based on the calculations of Sections III. E and III. H. All errors quoted are probable errors, and where no errors are indicated on the ion energies, it is implicitly assumed that the ion energy uncertainty is ≤ 1 per cent. See p. 62, text.

TABLE VIII (cont'd.). EXPERIMENTAL RANGE AND RANGE STRAGGLING MEASUREMENTS

Ion and Target	Ion Energy (kev)	Range (μgm/cm^2)	Range Straggling (μgm/cm^2)
A in B	49.6 ± 0.6	9.2 ± 0.9	3.6 ± 1.7
	100.2	19.0 ± 1.7	11.4 ± 1.4
	249.5	44.6 ± 2.8	17.2 ± 2.5
	300.0	55.6 ± 3.9	26.1 ± 3.3
	500.3	86.6 ± 5.8	22.9 ± 8.0
A in C	49.9	10.4 ± 2.7	7.5 ± 1.5
	100.0	18.1 ± 2.6	13.4 ± 1.5
	201.0	36.7 ± 4.1	19.6 ± 2.2
	300.0	49.2 ± 4.0	20.0 ± 4.4
	400.0	64.6 ± 7.4	28.9 ± 8.1
	500.0	86.0 ± 5.9	27.2 ± 5.6
Ne in Be	45.2 ± 2.7	14.1 ± 2.9	12.3 ± 2.1
	95.7 ± 2.5	41.7 ± 3.4	19.8 ± 3.0
	194.6 ± 3.5	72.7 ± 6.5	33.9 ± 3.9
	296.6 ± 3.6	108.9 ± 4.2	
	393.7 ± 5.5	134.1 ± 10.7	41.9 ± 9.9
	490.5 ± 7.4	155.1 ± 9.9	42.0 ± 6.7
Ne in C	50.1	17.9 ± 2.1	17.4 ± 2.9
	99.6 ± 1.1	38.3 ± 2.7	15.4 ± 4.7
	200.2	75.2 ± 4.1	24.2 ± 6.8
	299.7	100.4 ± 7.0	30.2 ± 12.5
	400.5	127.3 ± 8.2	40.3 ± 10.8
	500.6	143.7 ± 9.5	31.1 ± 10.7
N in Be	48.3 ± 1.3	23.8 ± 2.3	11.0 ± 1.8
	97.5 ± 1.9	40.9 ± 2.6	12.5 ± 3.5
	195.5 ± 3.6	76.5 ± 4.5	23.2 ± 5.6
	291.3 ± 6.3	103.1 ± 5.8	23.1 ± 5.5
	385.9 ± 9.6	127.6 ± 5.3	23.7 ± 6.2
	492.3 ± 7.6	151.2 ± 6.1	17.0 ± 5.7
N in C	49.9	24.0 ± 3.6	14.3 ± 3.9
	99.7 ± 1.1	43.4 ± 3.2	20.9 ± 6.0
	199.6	75.7 ± 6.7	31.5 ± 11.4
	300.0	100.9 ± 5.8	30.1 ± 12.2
N in Al	46.7 ± 2.1	30.8 ± 10.0	39.9 ± 10.8
	100.1	74.0 ± 8.3	22.2 ± 10.1
	200.2	114.1 ± 12.8	44.1 ± 12.5
	296.2 ± 3.6	156.1 ± 14.2	62.9 ± 16.0
	400.5	198.7 ± 15.1	42.8 ± 14.6
	497.4 ± 5.4	218.5 ± 16.8	57.2 ± 16.8

TABLE IX. RANGES OF RECOIL IONS IN GASES

Ion, energy, and gas	Equation 26 + projection correction equation 39 (μ gm/cm^2)	Lindhard-Scharff nuclear + electron stopping + projection correction (equation 39) (μ gm/cm^2)	Experiment (μ gm/cm^2)	Reference
116 kev Tl^{208} in H_2	3.84	≈ 4.1	5.03	(Baulch, 1957)
116 kev Tl^{208} in Air	8.57	≈ 8.9	8.66	(Baulch, 1957)
116 kev Tl^{208} in A	10.86	≈ 11.0	10.5	(Baulch, 1957)
101 kev Po^{218} in Air	7.25	≈ 7.8	8.27	(Baulch, 1957)
96.8 kev Ra^{224} in H_2	3.02	≈ 3.6	3.9 ± 0.1	(Valyocsik, 1959)
96.8 kev Ra^{224} in D_2	6.06	≈ 7.0	6.6 ± 0.1	(Valyocsik, 1959)
96.8 kev Ra^{224} in He	6.20	≈ 6.6	6.6 ± 0.2	(Valyocsik, 1959)
96.8 kev Ra^{224} in N_2	6.67	≈ 7.5	7.0 ± 0.3	(Valyocsik, 1959)
96.8 kev Ra^{224} in Ne	6.94	≈ 7.8	7.3 ± 0.4	(Valyocsik, 1959)
96.8 kev Ra^{224} in A	8.48	≈ 9.5	9.4 ± 0.6	(Valyocsik, 1959)
725 kev Th^{226} in D_2	44.8	34.2	32.0 ± 1.0	(Valyocsik, 1959)
725 kev Th^{226} in He	45.5	34.7	30 ± 2.2	(Valyocsik, 1959)
725 kev Th^{226} in N_2	49.1	37.8	38 ± 3.7	(Valyocsik, 1959)
725 kev Th^{226} in A	62.4	48.3	40 ± 2.3	(Valyocsik, 1959)

Table IX: Comparison between the experimental measurements of the range of recoil ions in gases of Baulch (Baulch, 1957) and of Valyocsik (Valyocsik, 1959) is made with the theory of Section II. Column 2 gives the theoretical prediction of equation 26 modified by the projection correction of equation 39. Column 3 gives the theoretical prediction of Lindhard and Scharff (Lindhard, 1961b) including electron stopping and the projection correction of equation 39. See p. 66, text.

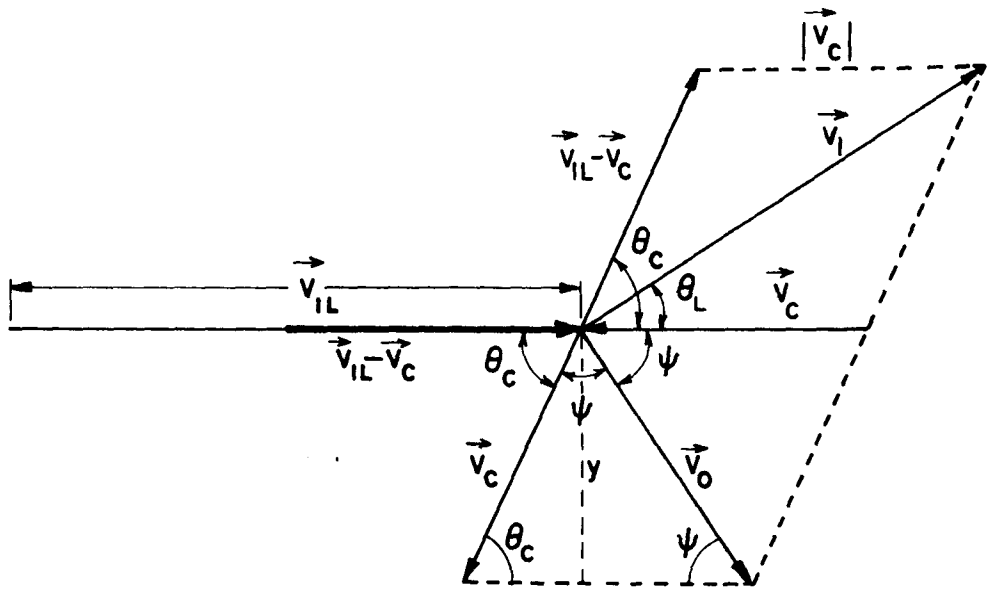

DETERMINATION OF LABORATORY VELOCITIES $\vec{V}_1$ AND $\vec{V}_0$ FROM CENTER OF MASS VELOCITY $\vec{V}_c$

Figure 1: The determination of laboratory velocities $\vec{v}_1$ and $\vec{v}_0$ from the center of mass velocity $\vec{v}_c$. The velocity of the incident atom is v_{1L}. θ_L and θ_c are the laboratory and center of mass angles, respectively, of the scattered atom. ψ is the laboratory angle with respect to the incident beam direction through which the "stationary atom" recoils. See p. 9, text.

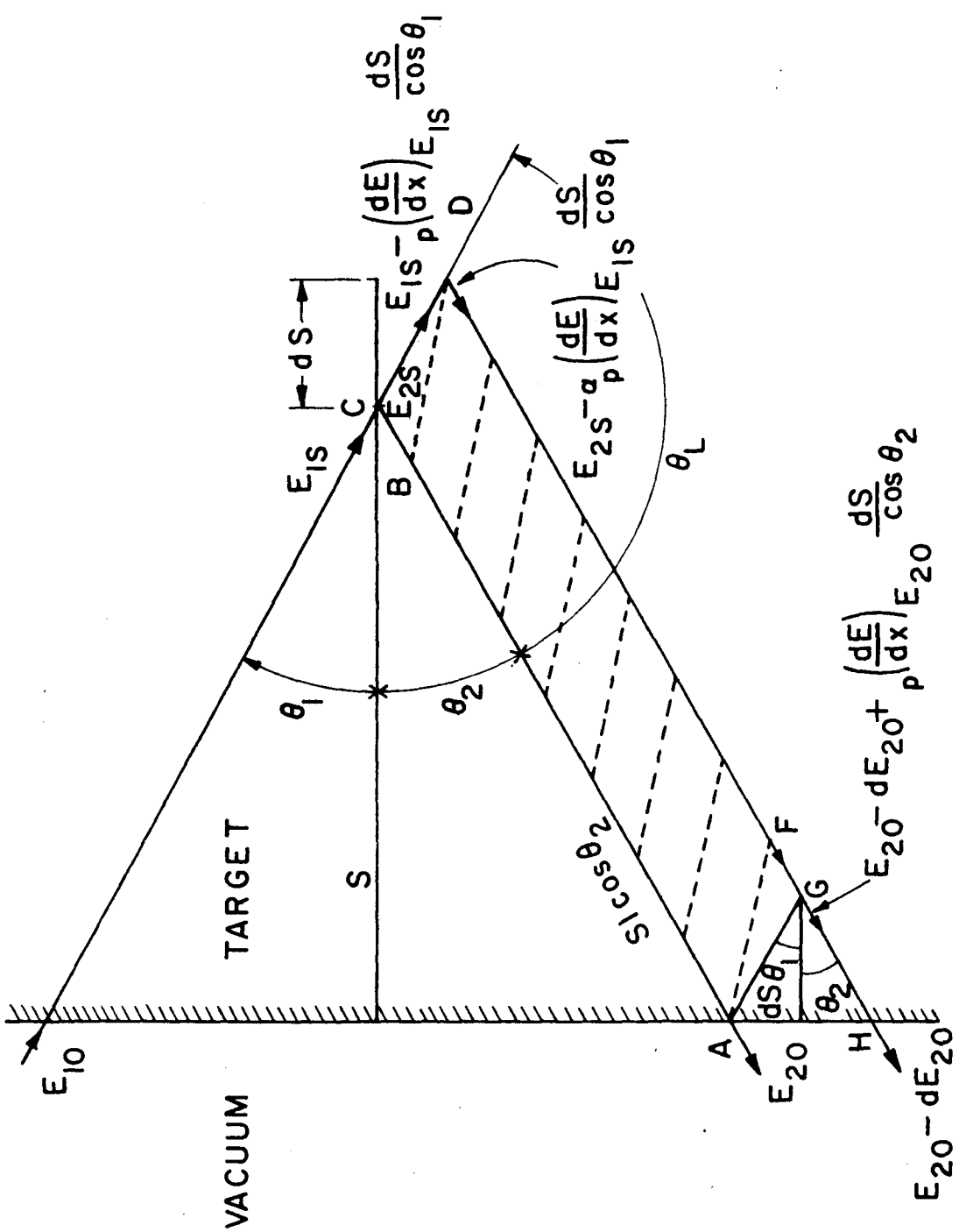

ENERGY RELATIONS IN TARGET

Figure 2: Energy relations in the target. E_{10} represents the bombarding proton energy. E_{1S} and E_{2S} are the incident and scattered proton energies, respectively, at a distance S beneath the surface. $E_{1S} - {}_p(dE/dx)_{E_{1S}} \cdot (dS/\cos\theta_1)$ and $E_{2S} - \alpha \cdot {}_p(dE/dx)_{E_{1S}} \cdot (dS/\cos\theta_1)$ are the incident and scattered energies, respectively, at a distance S+dS beneath the surface. Protons which scatter at C (i.e., a distance S beneath the surface) emerge from the target at A with energy E_{20}. Protons which scatter at D (i.e., a distance S+dS beneath the surface) emerge from the target at H with energy $E_{20} - dE_{20}$. The parallel dashed lines represent lines of equal energy. θ_L is the laboratory scattering angle, and θ_1 and θ_2 are the target orientation angles. See pp. 30, 32, 73, 74, text.

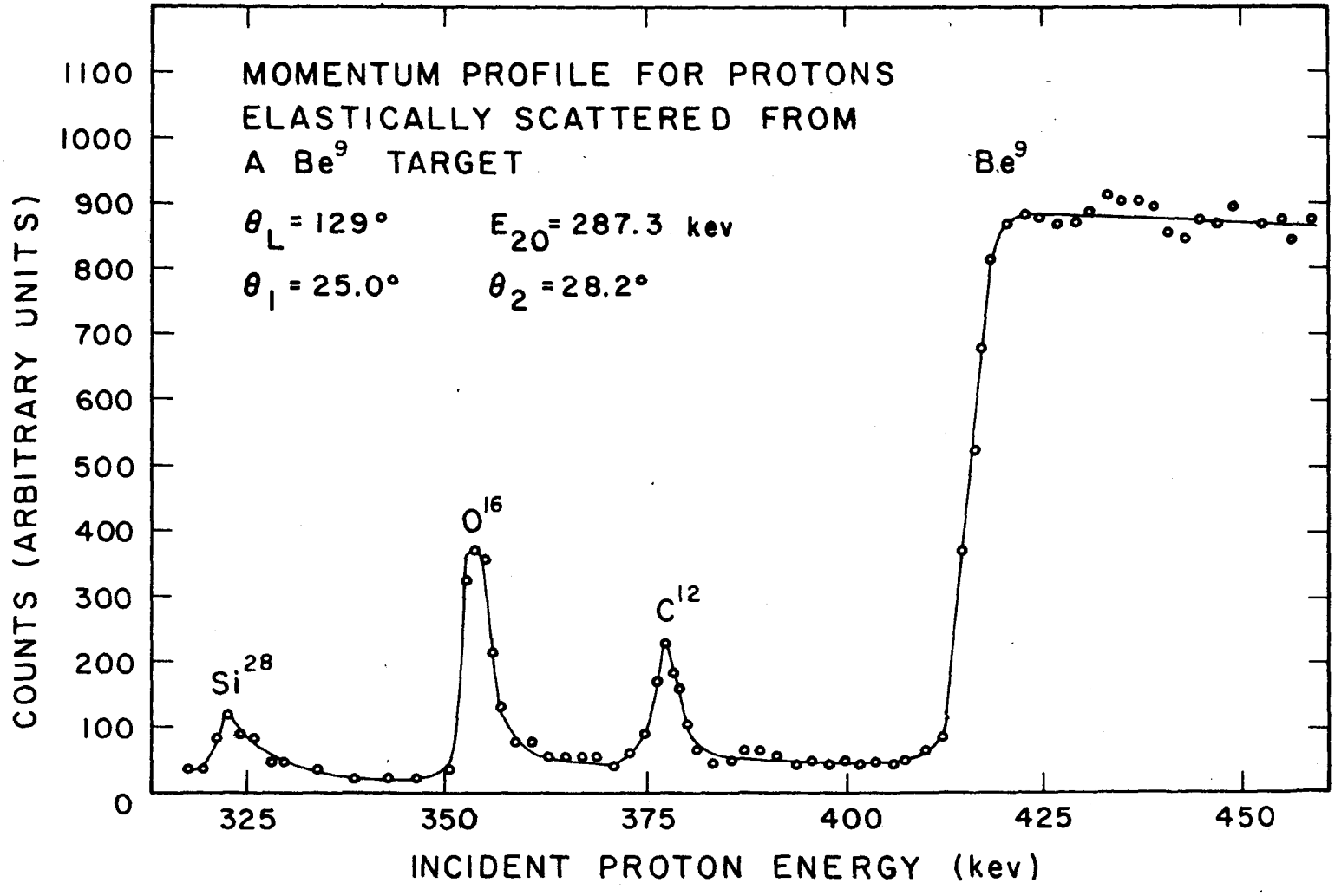
MOMENTUM PROFILE FOR PROTONS
ELASTICALLY SCATTERED FROM
A Be9 TARGET
θL = 129°
E20 = 287.3 kev
θ1 = 25.0°
θ2 = 28.2°
Be9
O16
C12
Si28
COUNTS (ARBITRARY UNITS)
INCIDENT PROTON ENERGY (kev)
0
100
200
300
400
500
600
700
800
900
1000
1100
325
350
375
400
425
450

Figure 3: Momentum profile for protons elastically scattered from a clean Be^9 target. The scattered proton energy E_{20} is fixed by the spectrometer; the number of counts observed in the detector is plotted as a function of the incident proton energy E_{10}. Surface layers of Si, O, and C at 322, 354, and 377 kev are identified with equations 46 and 48 with S = 0 and M_0 = 28, 16, and 12, respectively. The continuum beginning at E_{10} = 415 kev indicates a distribution of nuclei with mass nine beginning at S = 0 and extending into the target. See p. 32, text.

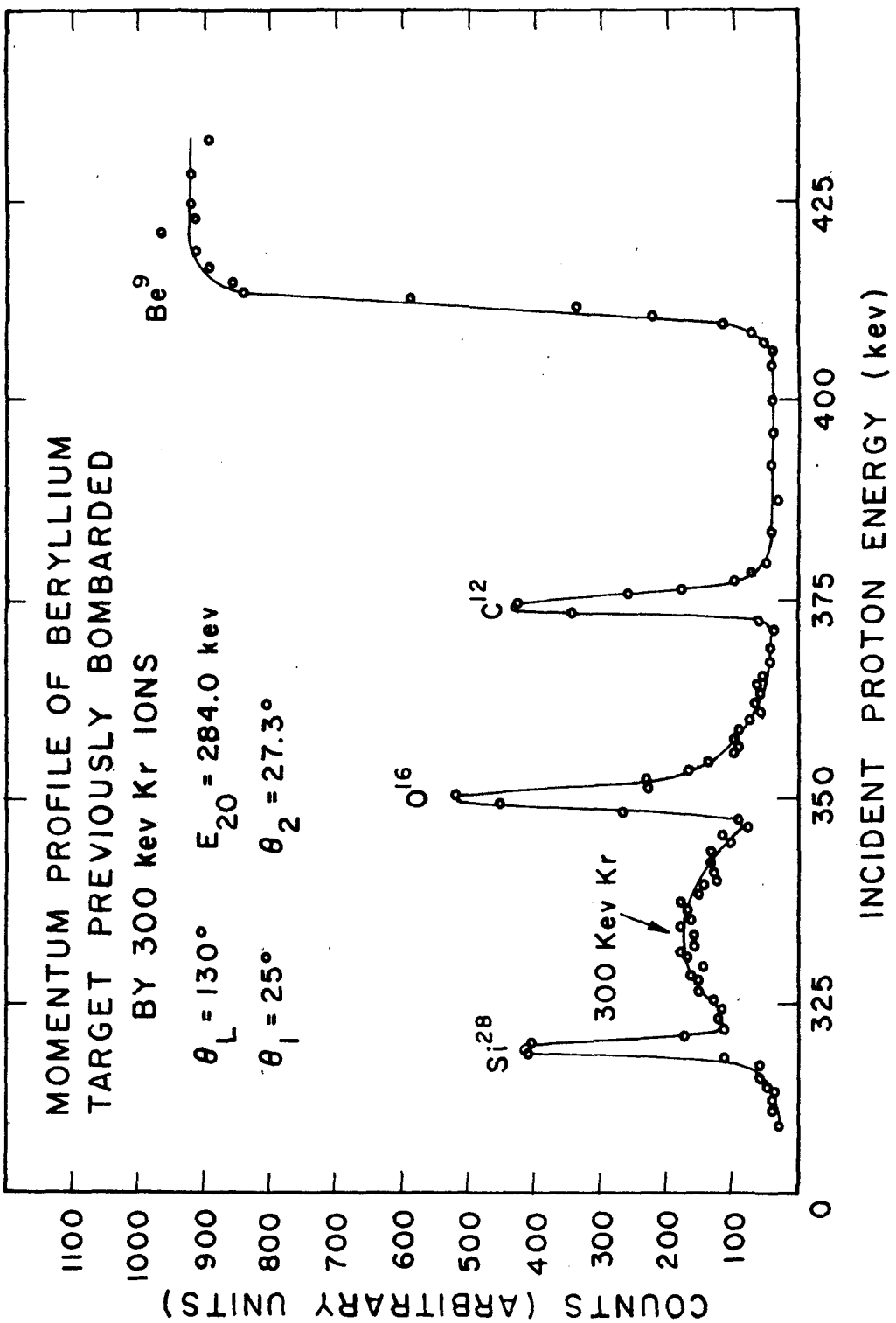
MOMENTUM PROFILE OF BERYLLIUM
TARGET PREVIOUSLY BOMBARDED
BY 300 kev Kr IONS
$\theta_L = 130°$ $E_{20} = 284.0$ kev
$\theta_1 = 25°$ $\theta_2 = 27.3°$
Be^9
C^{12}
O^{16}
Si^{28}
300 Kev Kr
COUNTS (ARBITRARY UNITS)
INCIDENT PROTON ENERGY (kev)
0
100
200
300
400
500
600
700
800
900
1000
1100
325
350
375
400
425

Figure 4: Momentum profile for protons elastically scattered from a Be^9 target previously bombarded by 300-kev krypton ions. The Si, O, and C peaks along with the beryllium step are identified as in fig. 3. The broad peak at 334 kev could be identified with S = 0 and mass $M_0 = 21.2$ or with $M_0 = 83.8$ and S = 35.5 $\mu gm/cm^2$. The latter choice is the reasonable one since the broad peak was not observed when protons were scattered from the target prior to the krypton bombardment. See pp. 32, 33, 35, 53, text.

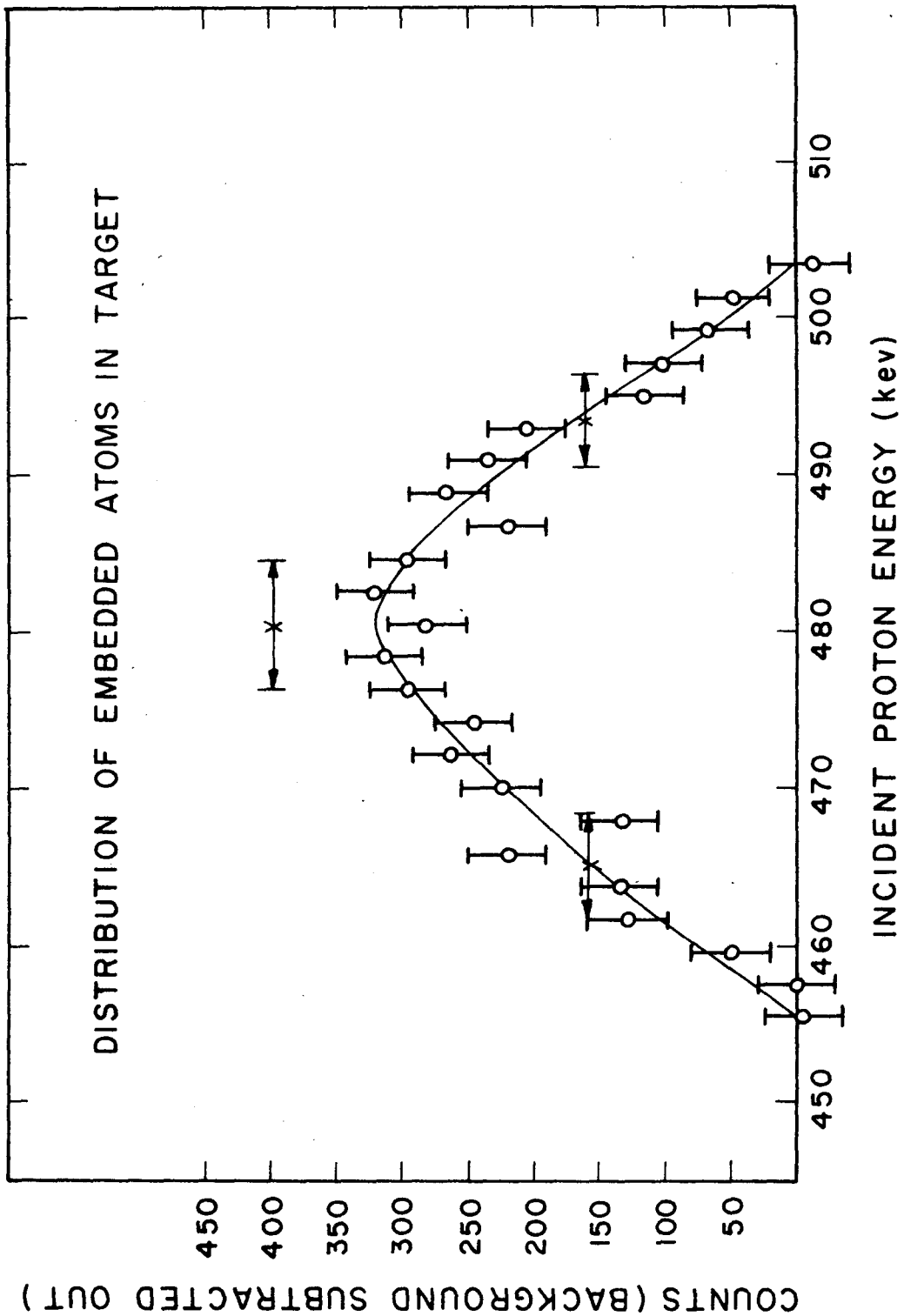
DISTRIBUTION OF EMBEDDED ATOMS IN TARGET
COUNTS (BACKGROUND SUBTRACTED OUT)
450
400
350
300
250
200
150
100
50
450
460
470
480
490
500
510
INCIDENT PROTON ENERGY (kev)

Figure 5: Distribution of embedded atoms in the target obtained by subtracting a clean target profile from the bombarded profile for 291 kev N in Be. Error bars on the ordinates are probable errors in the counting statistics. A smooth curve was drawn by eye through the observed points. Uncertainties in energies at maximum and half-maximum points resulting from uncertainty in the actual shape of the curve drawn through the observed points are indicated. See p. 33, 35, text.

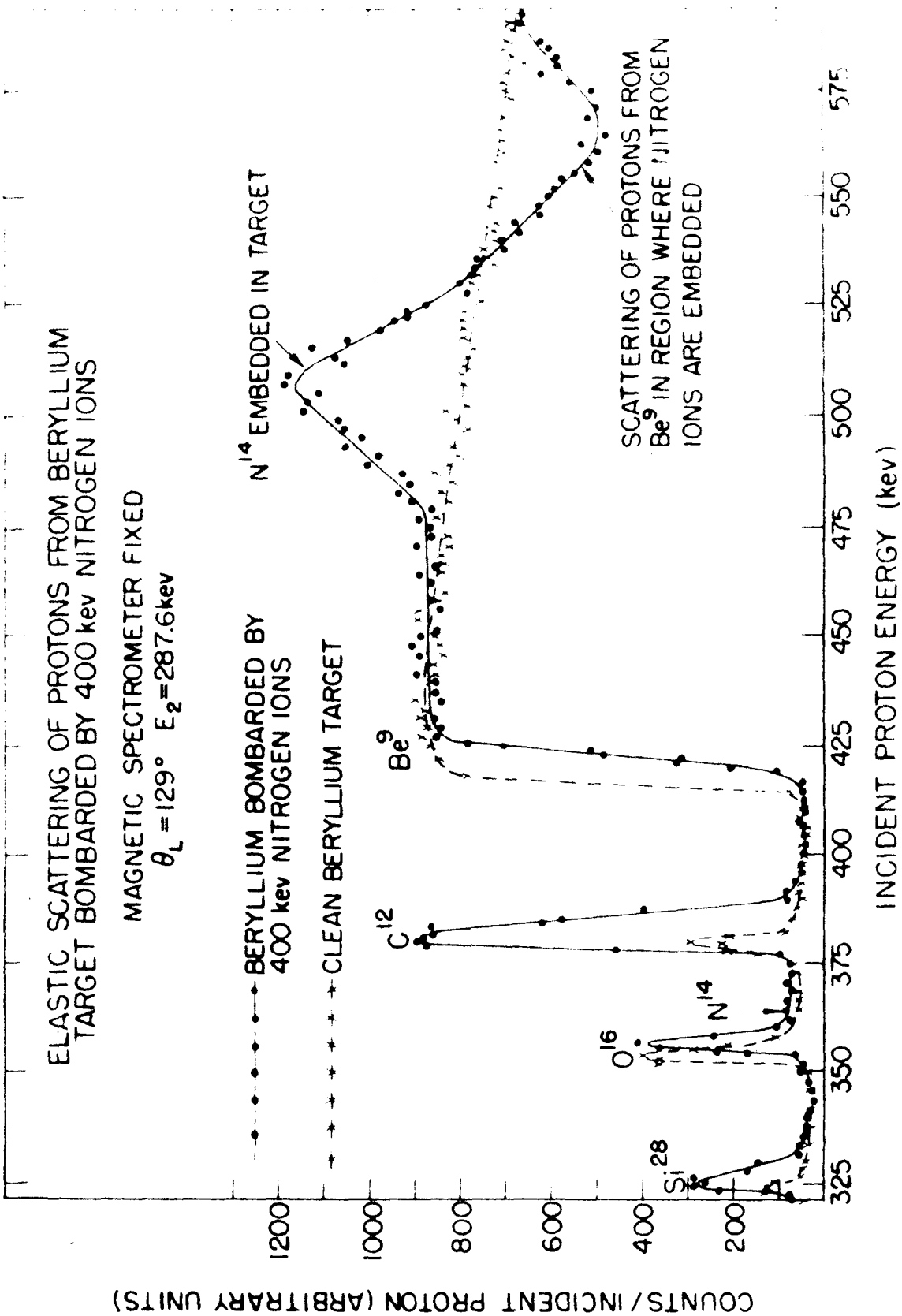
ELASTIC SCATTERING OF PROTONS FROM BERYLLIUM TARGET BOMBARDED BY 400 kev NITROGEN IONS
MAGNETIC SPECTROMETER FIXED
$\theta_L = 129°$ $E_2 = 287.6$kev
BERYLLIUM BOMBARDED BY 400 kev NITROGEN IONS
CLEAN BERYLLIUM TARGET
N^{14} EMBEDDED IN TARGET
SCATTERING OF PROTONS FROM Be^9 IN REGION WHERE NITROGEN IONS ARE EMBEDDED
Si^{28}
O^{16}
N^{14}
C^{12}
Be^9
COUNTS / INCIDENT PROTON (ARBITRARY UNITS)
INCIDENT PROTON ENERGY (kev)
200
400
600
800
1000
1200
325
350
375
400
425
450
475
500
525
550
575

Figure 6: An example of a profile where both peak and dip are present. The peak is due to protons elastically scattered from the N atoms embedded in the target; the dip is due to protons elastically scattered from Be atoms in the region where the N atoms are present. The displacement of the Be step is due to the increased proton energy required to penetrate the surface layers of C and Si built up during the long ionic bombardment. See p. 42, text.

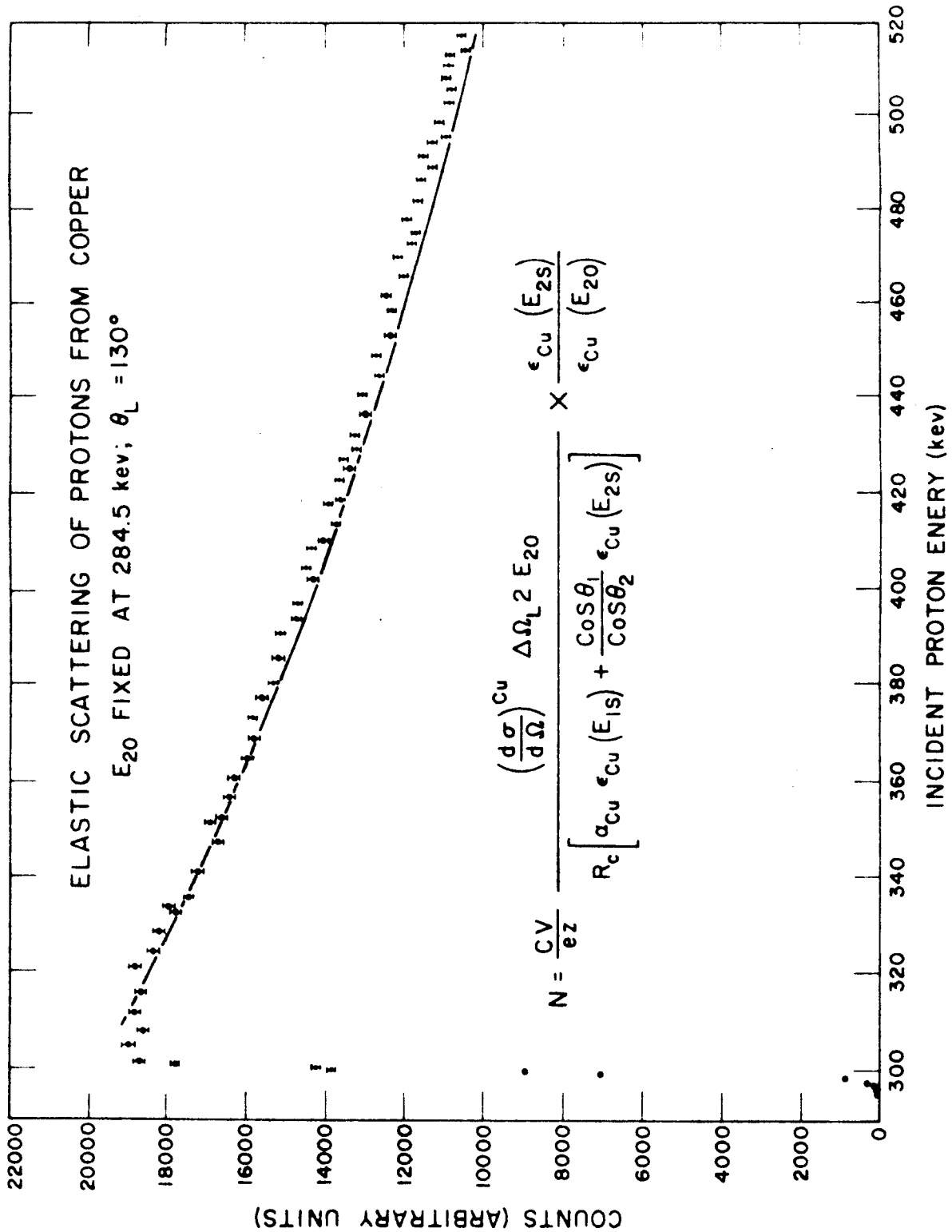
ELASTIC SCATTERING OF PROTONS FROM COPPER
E_{20} FIXED AT 284.5 kev; $\theta_L = 130°$
$N = \frac{CV}{ez} \left(\frac{d\sigma}{d\Omega}\right)^{Cu} \Delta\Omega_L 2 E_{20} \Big/ R_c \left[\alpha_{Cu}\, \epsilon_{Cu}(E_{1S}) + \frac{\cos\theta_1}{\cos\theta_2}\, \epsilon_{Cu}(E_{2S})\right] \times \frac{\epsilon_{Cu}(E_{2S})}{\epsilon_{Cu}(E_{20})}$
COUNTS (ARBITRARY UNITS)
INCIDENT PROTON ENERY (kev)
0
2000
4000
6000
8000
10000
12000
14000
16000
18000
20000
22000
300
320
340
360
380
400
420
440
460
480
500
520

Figure 7: Elastic scattering of protons from a copper target to test the validity of formula AIII5 of Appendix III. The solid curve is the predicted yield of formula AIII5, where the proton scattering has been assumed to be Rutherford except for a multiplicative screening factor of magnitude $(1 - 32.6\ Z_{Cu}/E_{1S}(ev))$. The scattering seems to indicate a 3 per cent discrepancy between the experimental scattering yield and the predicted scattering yield. The discrepancy may be due to the $\pm$ 3 per cent uncertainty in the proton stopping cross sections of copper. See p. 43, text.

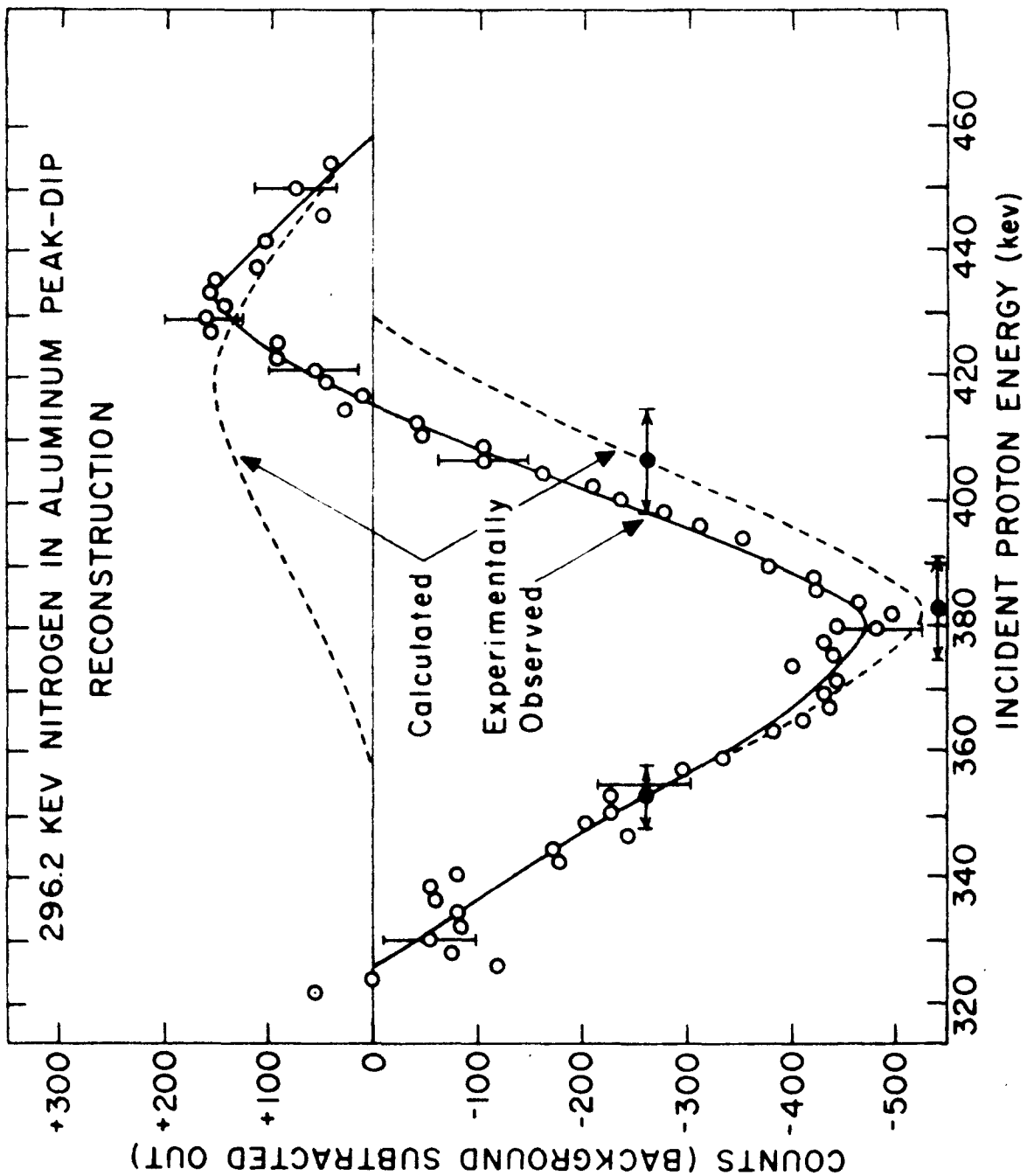
296.2 KEV NITROGEN IN ALUMINUM PEAK-DIP
RECONSTRUCTION
Calculated
Experimentally
Observed
COUNTS (BACKGROUND SUBTRACTED OUT)
+300
+200
+100
0
-100
-200
-300
-400
-500
320
340
360
380
400
420
440
460
INCIDENT PROTON ENERGY (kev)

Figure 8: Nitrogen in aluminum peak-dip reconstruction. The dotted curves are calculated with the aid of the thick target yield formulas of Appendix III by the procedure of Section III. F, and represent the shape of the peak and dip in the absence of interference. It is seen that the penetration depth and range straggling are greater using the reconstructed data than they would be if the uncorrected data were used. See p. 44, text.

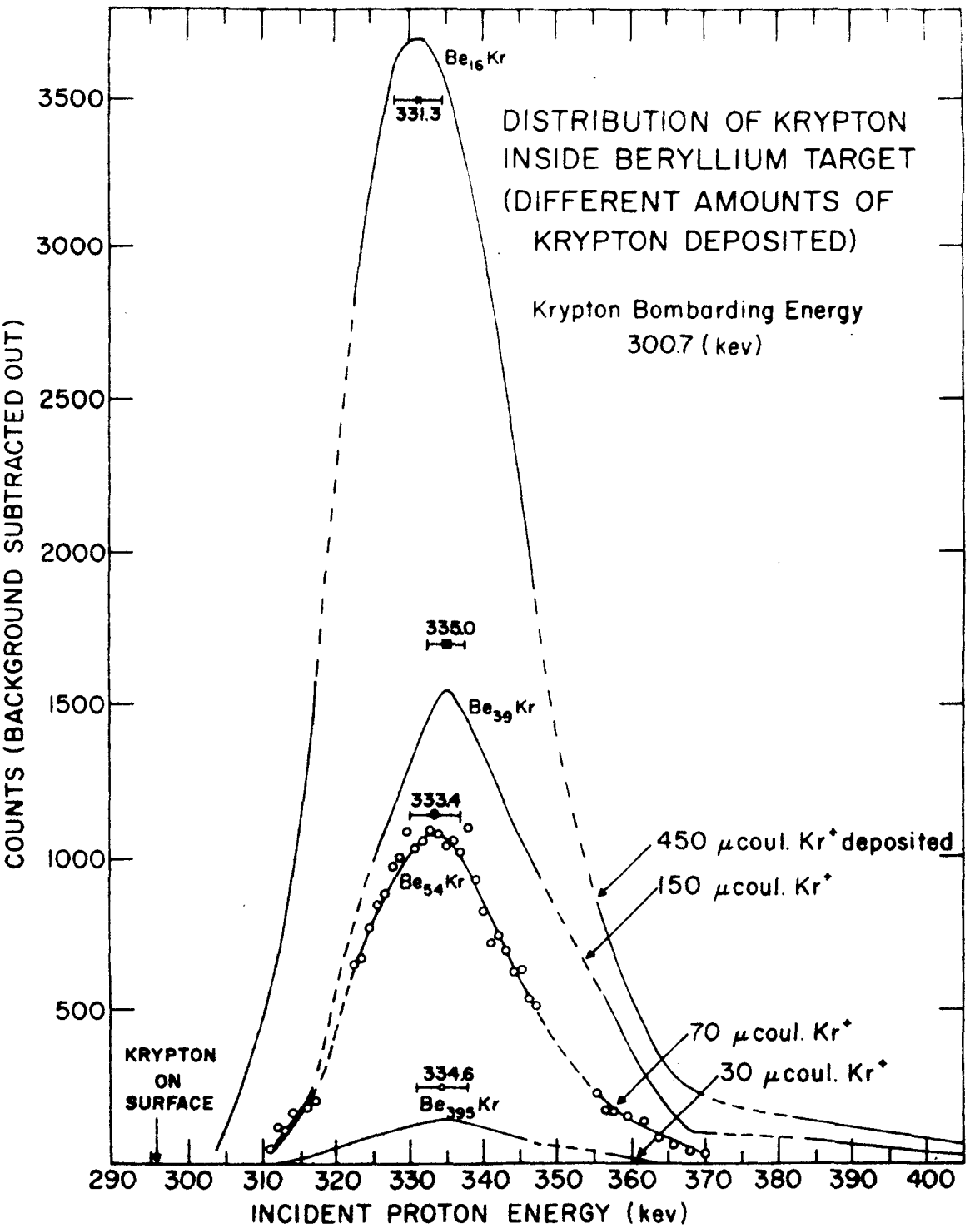
DISTRIBUTION OF KRYPTON
INSIDE BERYLLIUM TARGET
(DIFFERENT AMOUNTS OF
KRYPTON DEPOSITED)
Krypton Bombarding Energy
300.7 (kev)
Be16Kr
331.3
335.0
Be39Kr
333.4
Be54Kr
334.6
Be395Kr
450 μcoul. Kr+ deposited
150 μcoul. Kr+
70 μcoul. Kr+
30 μcoul. Kr+
KRYPTON
ON
SURFACE
COUNTS (BACKGROUND SUBTRACTED OUT)
INCIDENT PROTON ENERGY (kev)
3500
3000
2500
2000
1500
1000
500
290
300
310
320
330
340
350
360
370
380
390
400

Figure 9: Distribution of krypton in beryllium target as a function of the amount of krypton ion deposited. The maximum concentration of Kr in each bombardment is expressed as an effective molecular composition. Protons scattered from the three lesser concentrations of krypton indicate that the embedded atoms have no effect on the range measurement greater than the experimental uncertainty. Concentrations greater than one krypton atom per ($\approx$ 30) beryllium atoms introduce a noticeable shift in the peak. See p. 46, text.

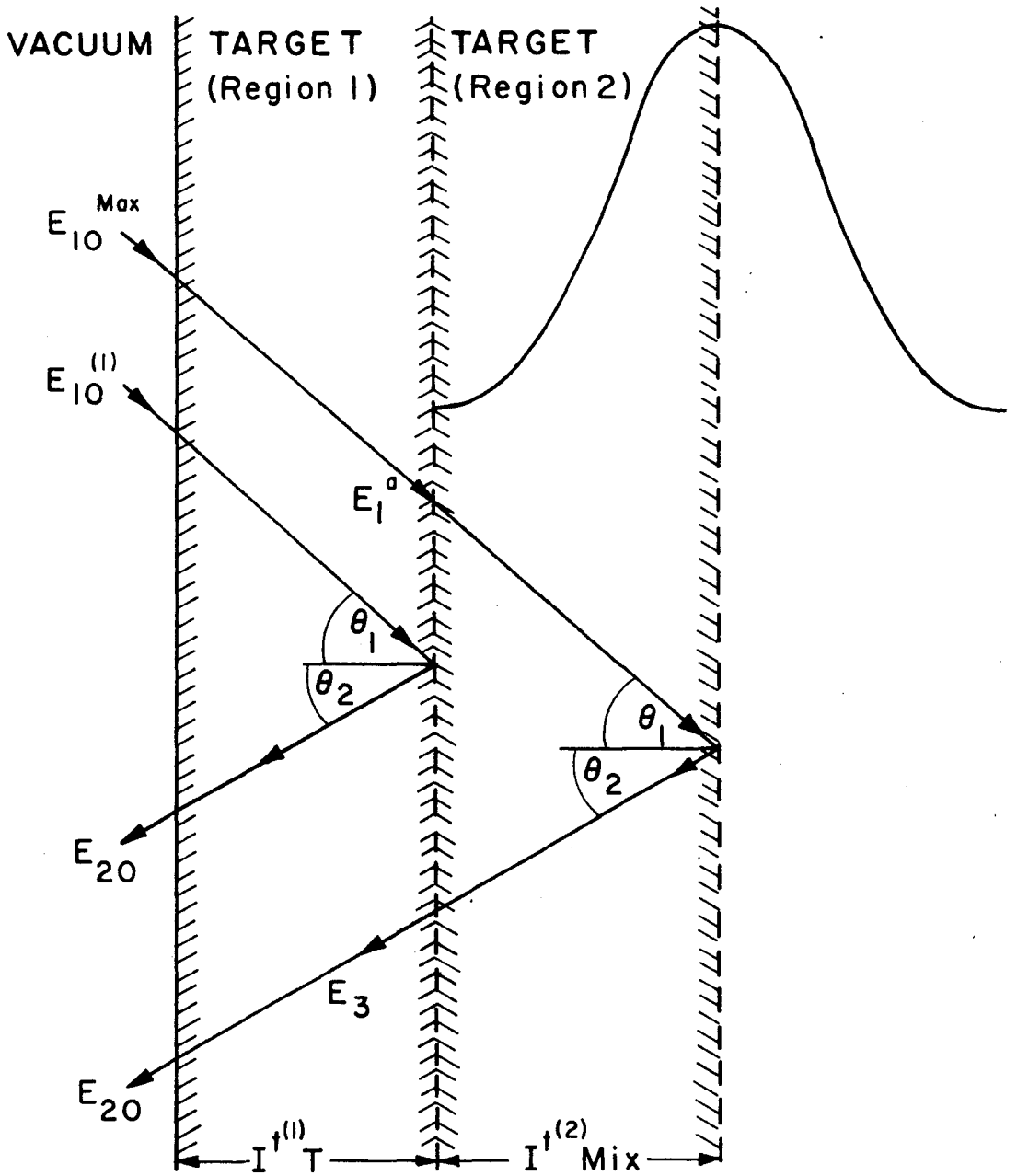

DIVISION OF TARGET INTO TWO REGIONS
TO CALCULATE NEON AND NITROGEN RANGES

Figure 10: Division of target into two regions to calculate neon and nitrogen ranges. Region 1 represents a layer of pure target atoms. Region 2 represents a layer consisting of a mixture of target and impurity atoms; the impurity atom concentration increases with depth. Proton energy $E_{10}^{(1)}$ is required to scatter from the region 1 - region 2 interface, and proton energy E_{10}^{max} is required to scatter from the layer of atoms having the maximum impurity atom concentration. See p. 48, text.

Figure 11

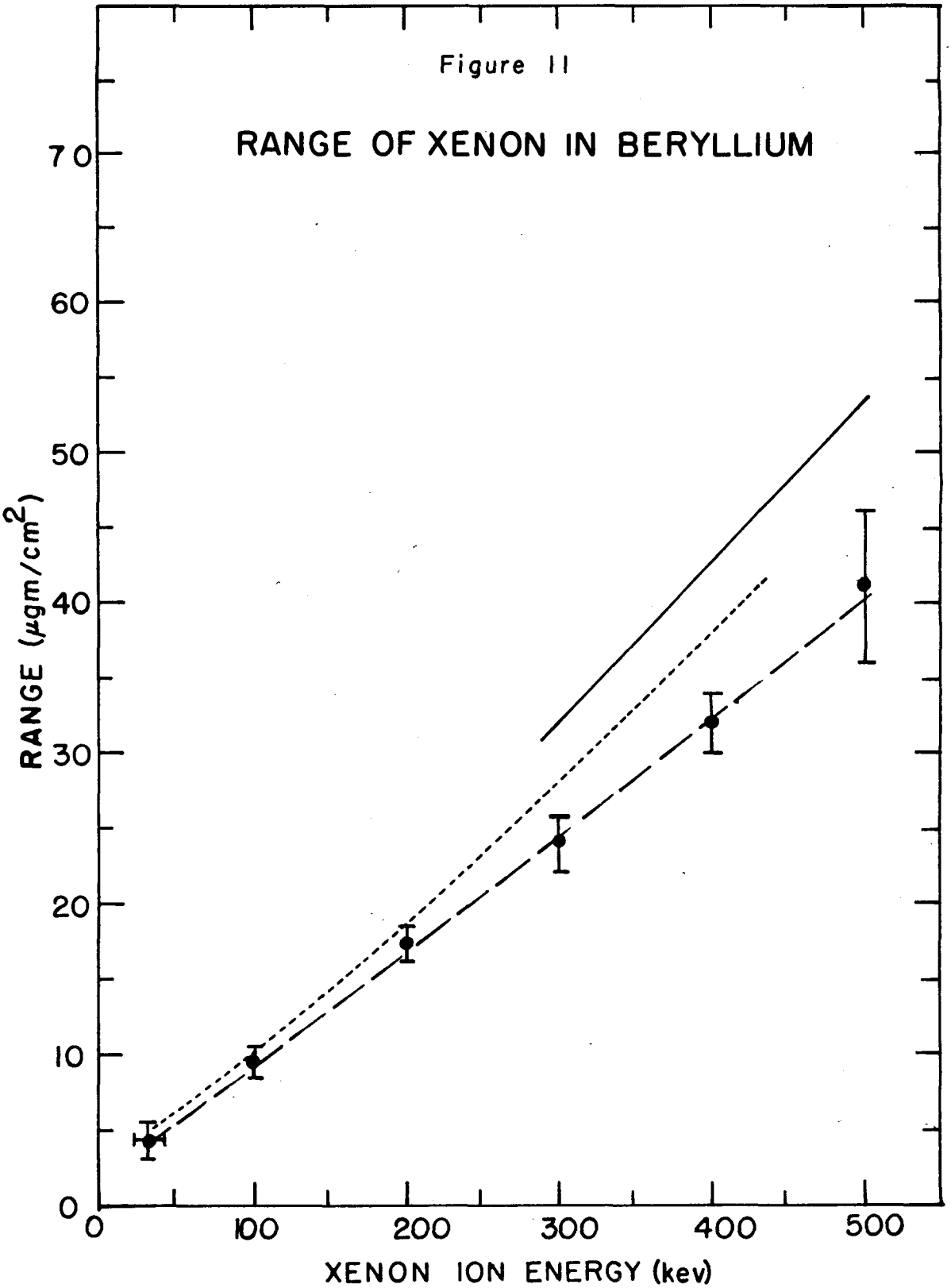
RANGE OF XENON IN BERYLLIUM
RANGE (μgm/cm²)
XENON ION ENERGY (kev)
0
10
20
30
40
50
60
70
0
100
200
300
400
500

Figures 11 - 18: The range of xenon, krypton, and argon in various targets is plotted as a function of the ion bombarding energy. The solid curve in each figure is the theoretical prediction of equation 26 for the range modified by the projection correction of equation 36. The curve is drawn over the region of validity of the r^{-2} potential mentioned in Section II. D . The dotted curve in each figure is the theoretical prediction of Lindhard and Scharff (Lindhard, 1961a) neglecting electron excitation, but including projection correction (equation 39). The dashed curve is the theoretical prediction of Lindhard and Scharff (Lindhard, 1961b) including both projection correction and electron excitation. See pp. 62-65, text.

Figure 12

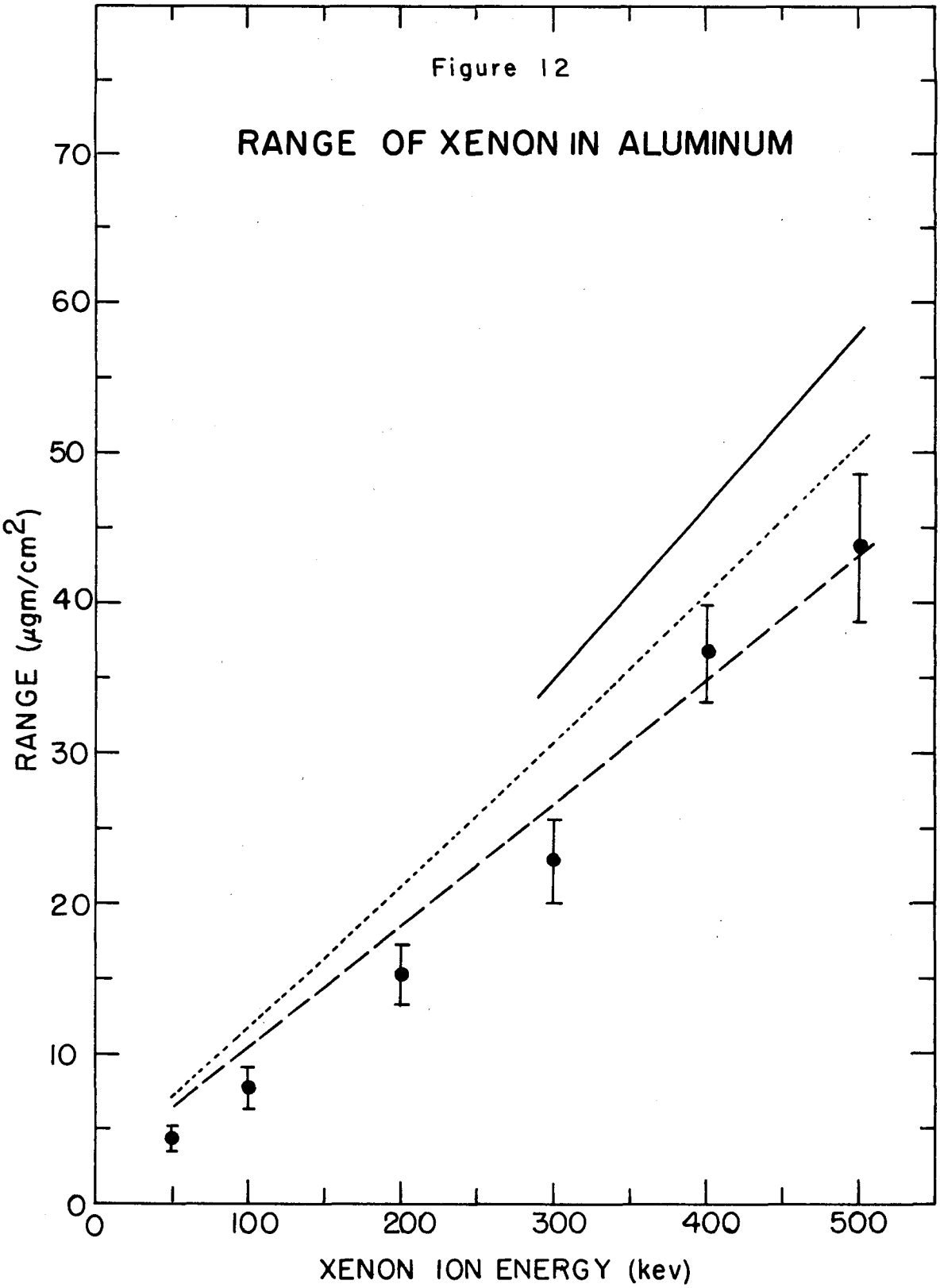
RANGE OF XENON IN ALUMINUM
RANGE (μgm/cm²)
XENON ION ENERGY (kev)
0
10
20
30
40
50
60
70
0
100
200
300
400
500

Figure 13

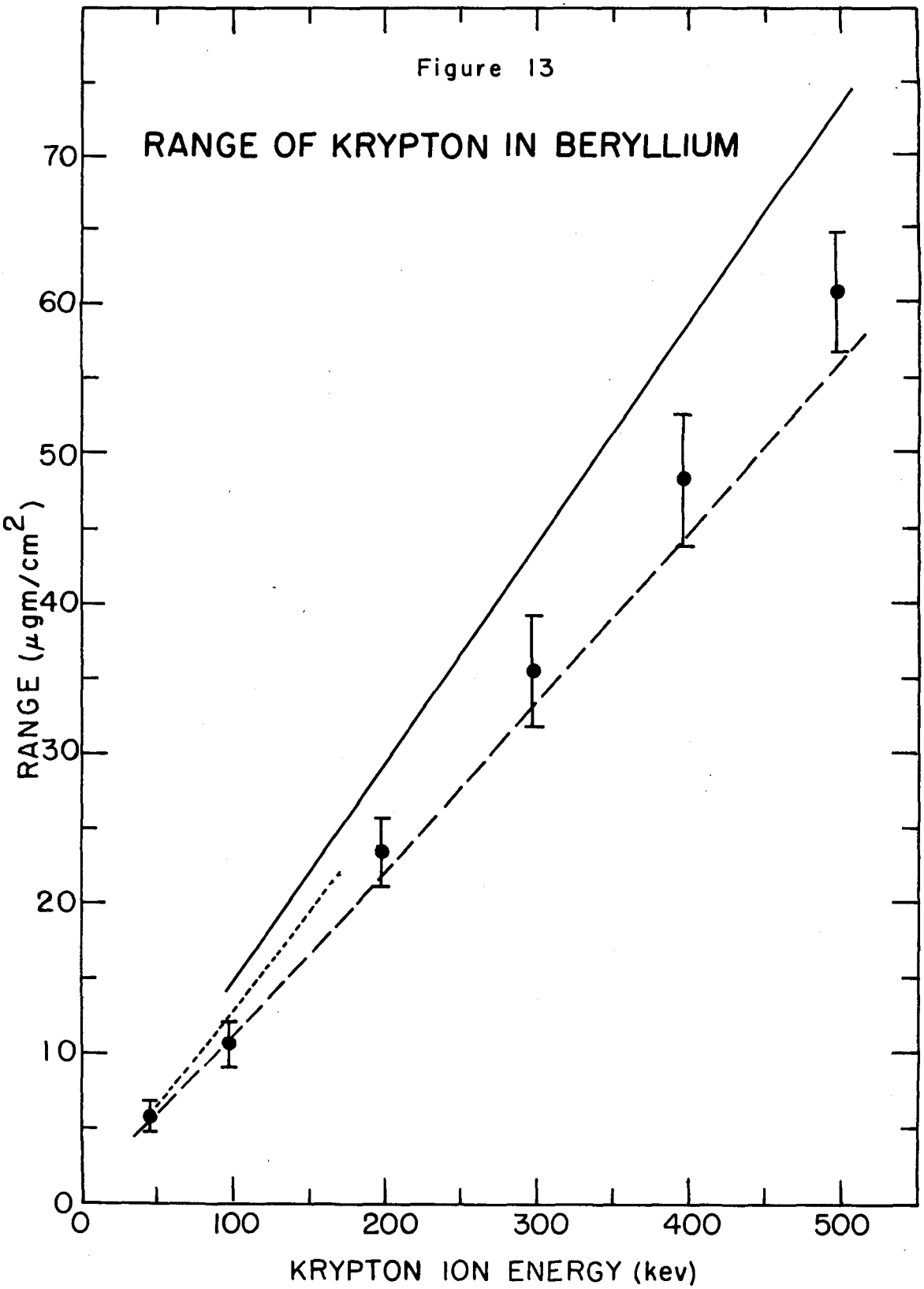
RANGE OF KRYPTON IN BERYLLIUM
RANGE (μgm/cm²)
KRYPTON ION ENERGY (kev)
0
10
20
30
40
50
60
70
0
100
200
300
400
500

Figure 14

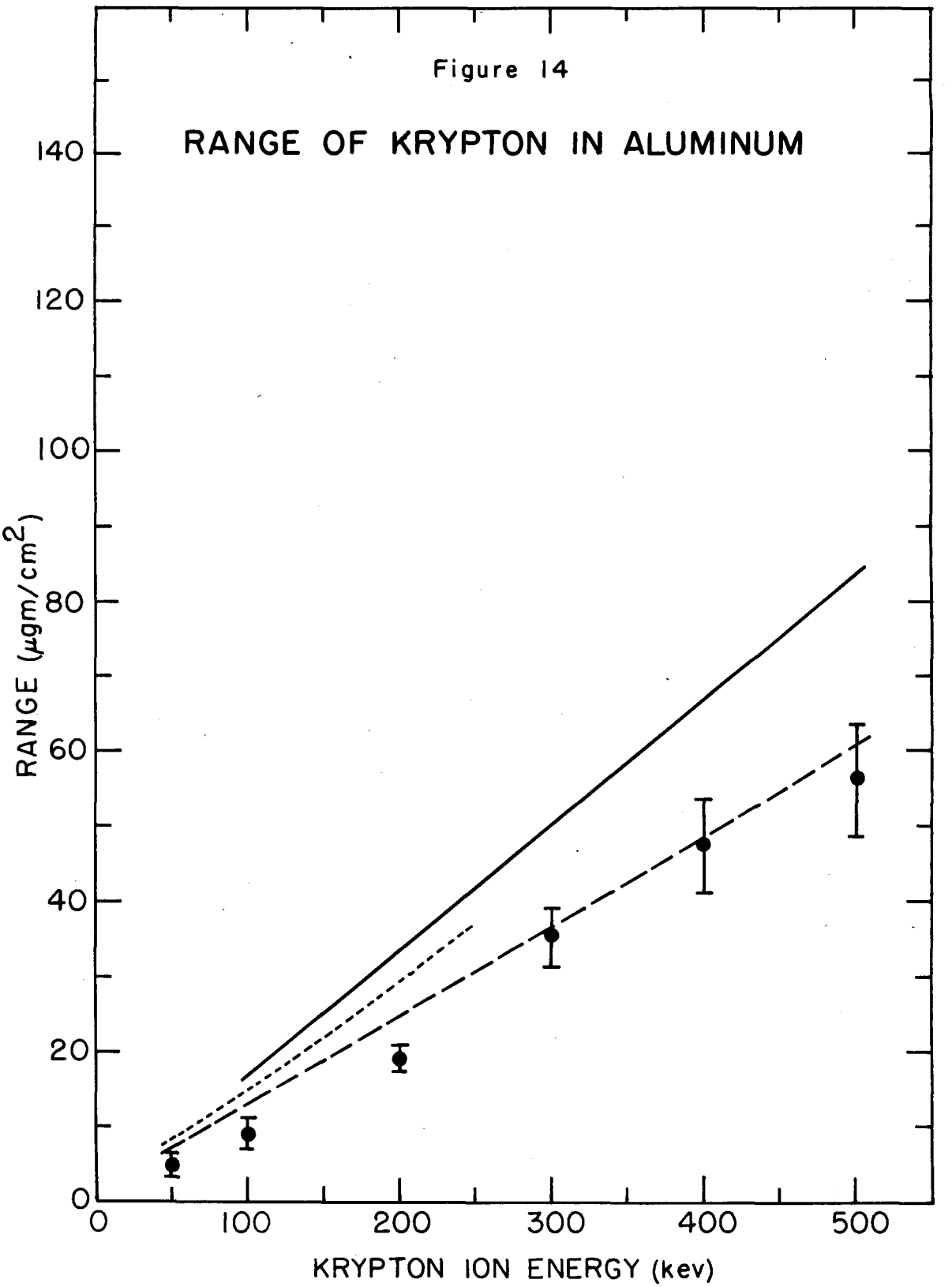
RANGE OF KRYPTON IN ALUMINUM
RANGE (μgm/cm²)
KRYPTON ION ENERGY (kev)
0
20
40
60
80
100
120
140
0
100
200
300
400
500

Figure 15

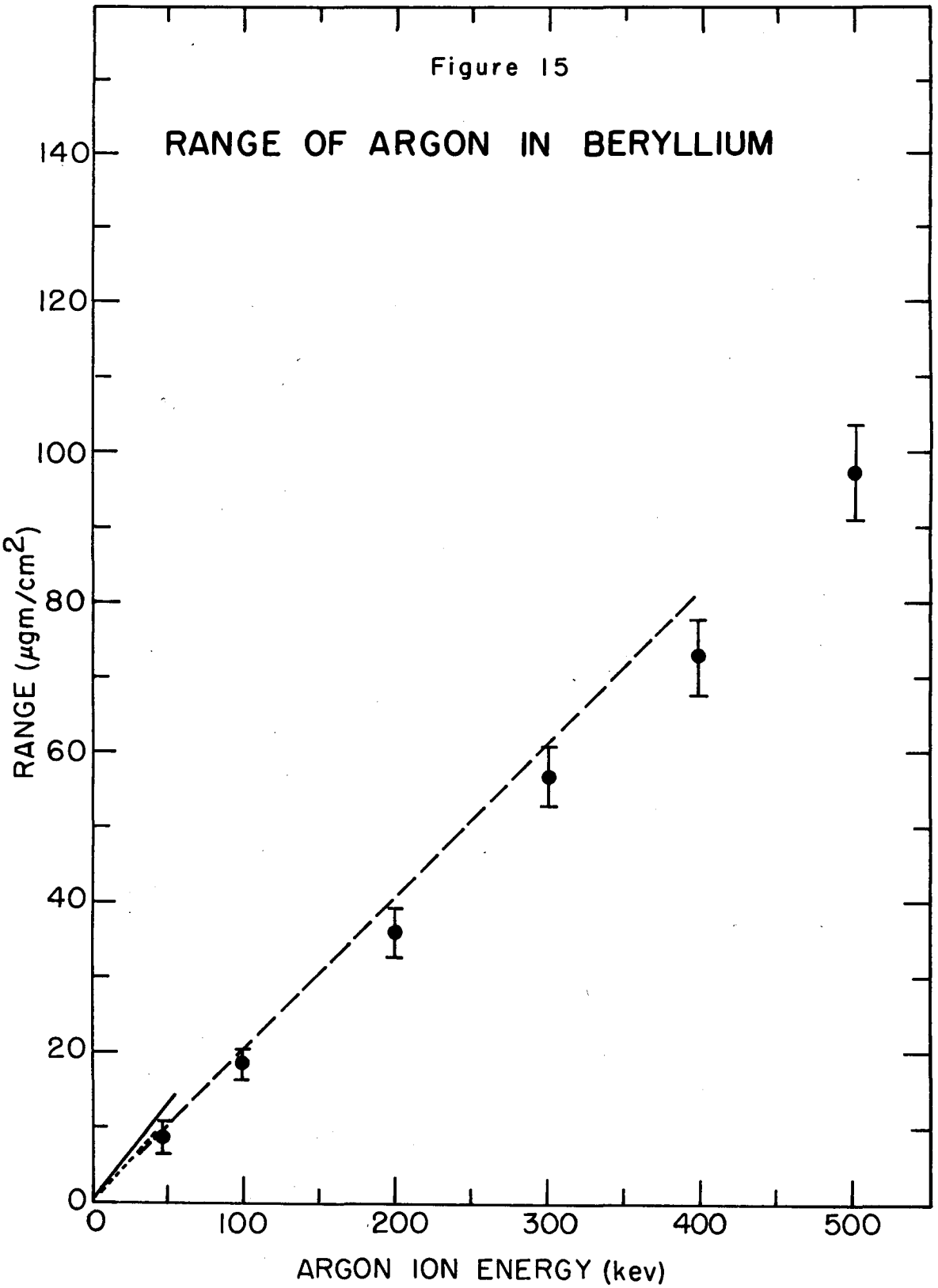
RANGE OF ARGON IN BERYLLIUM
RANGE (μgm/cm²)
ARGON ION ENERGY (kev)
0
20
40
60
80
100
120
140
0
100
200
300
400
500

Figure 16

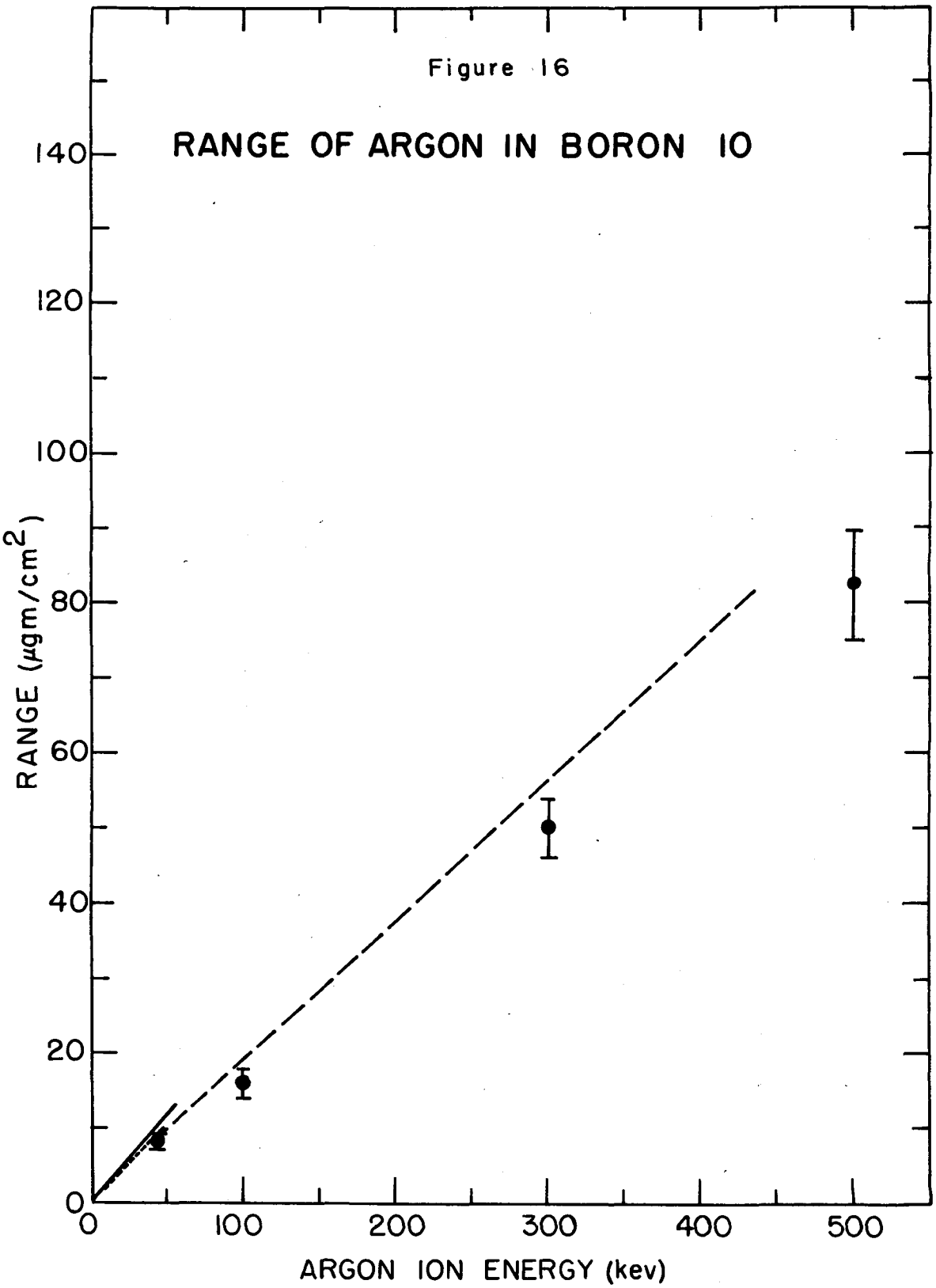
RANGE OF ARGON IN BORON 10
RANGE (μgm/cm²)
ARGON ION ENERGY (kev)
0
20
40
60
80
100
120
140
0
100
200
300
400
500

Figure 17

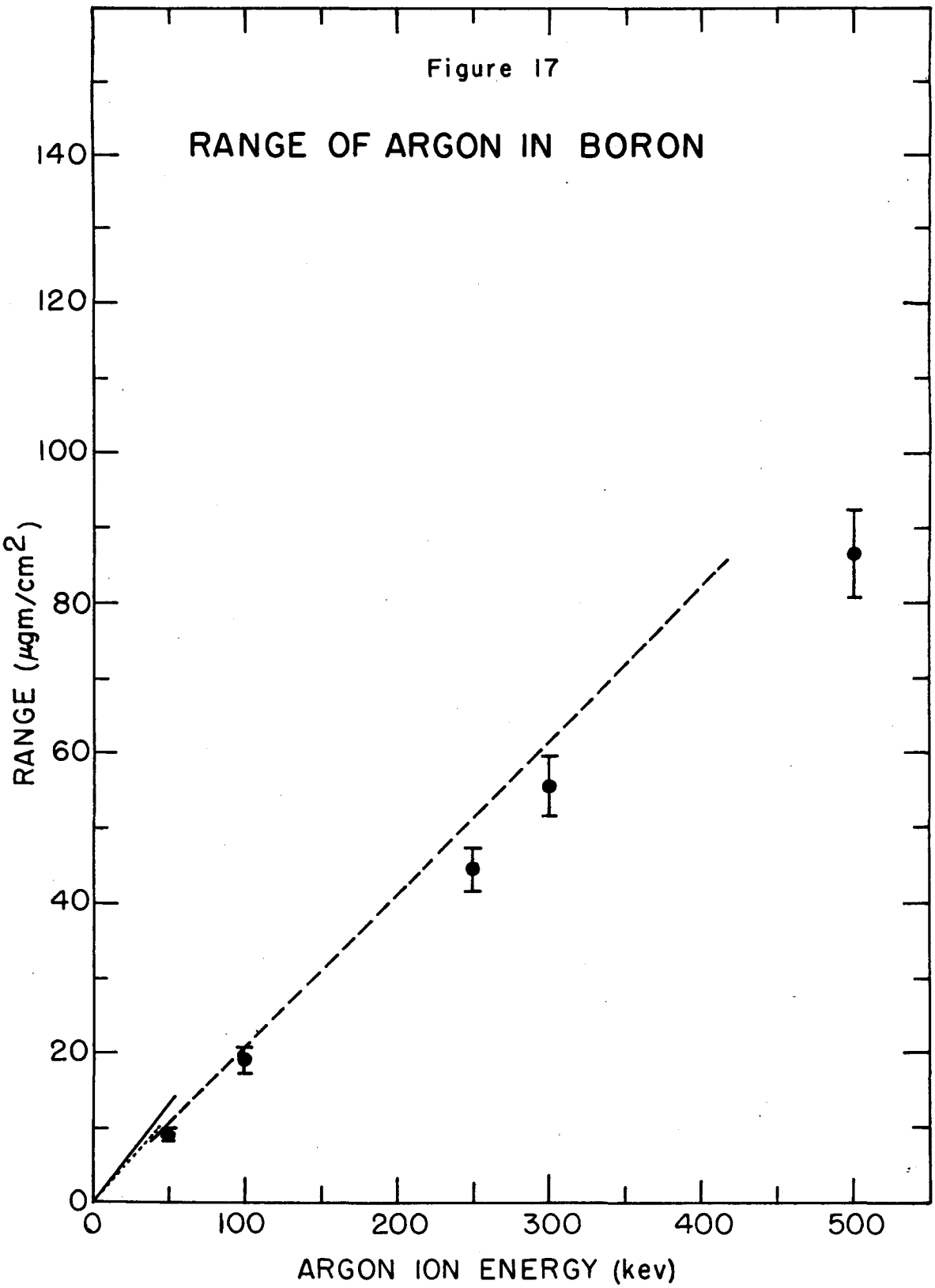
RANGE OF ARGON IN BORON
RANGE (μgm/cm²)
ARGON ION ENERGY (kev)
0
20
40
60
80
100
120
140
0
100
200
300
400
500

Figure 18

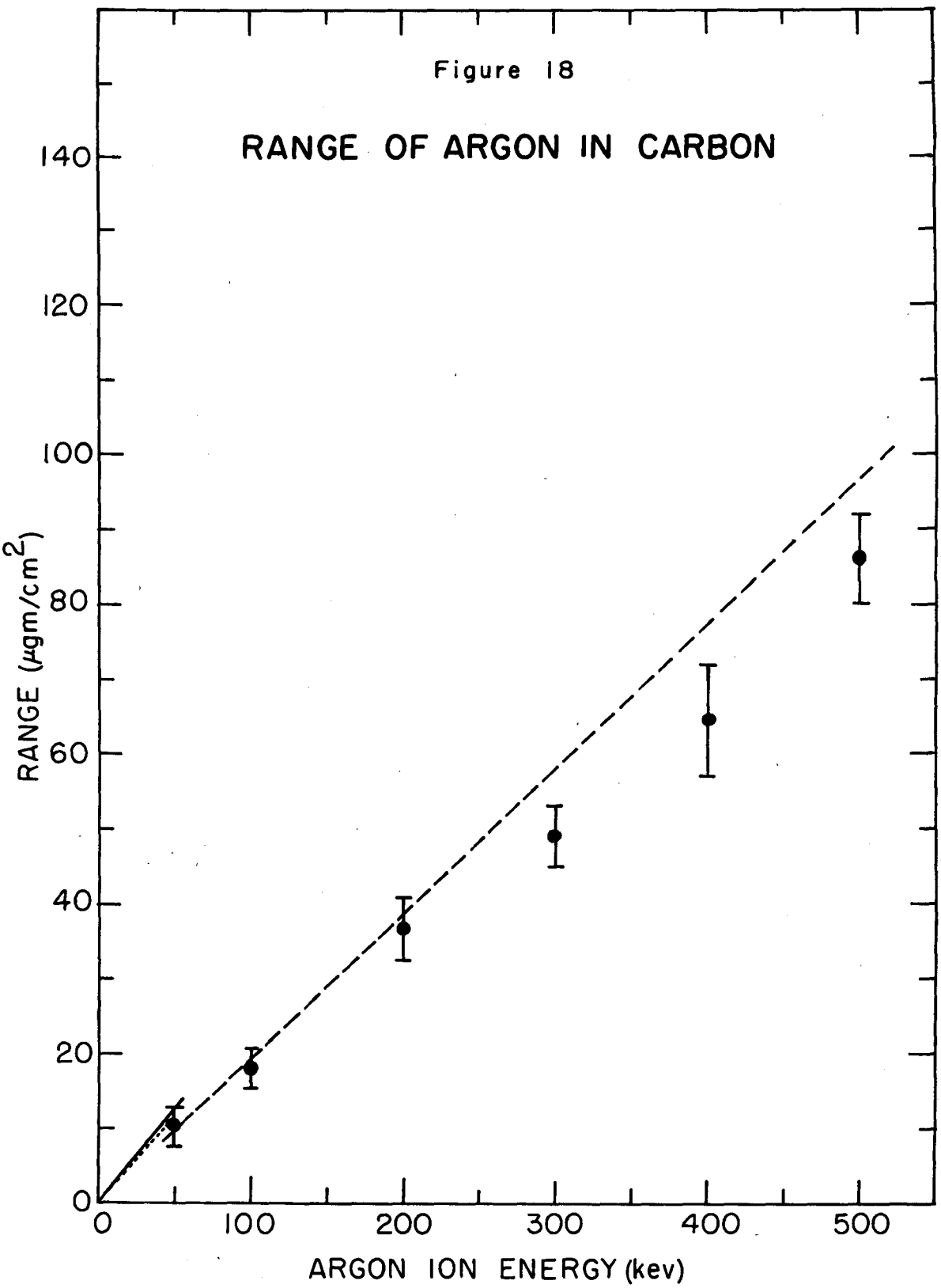
RANGE OF ARGON IN CARBON
RANGE (μgm/cm²)
ARGON ION ENERGY (kev)
0
20
40
60
80
100
120
140
0
100
200
300
400
500

Figure 19

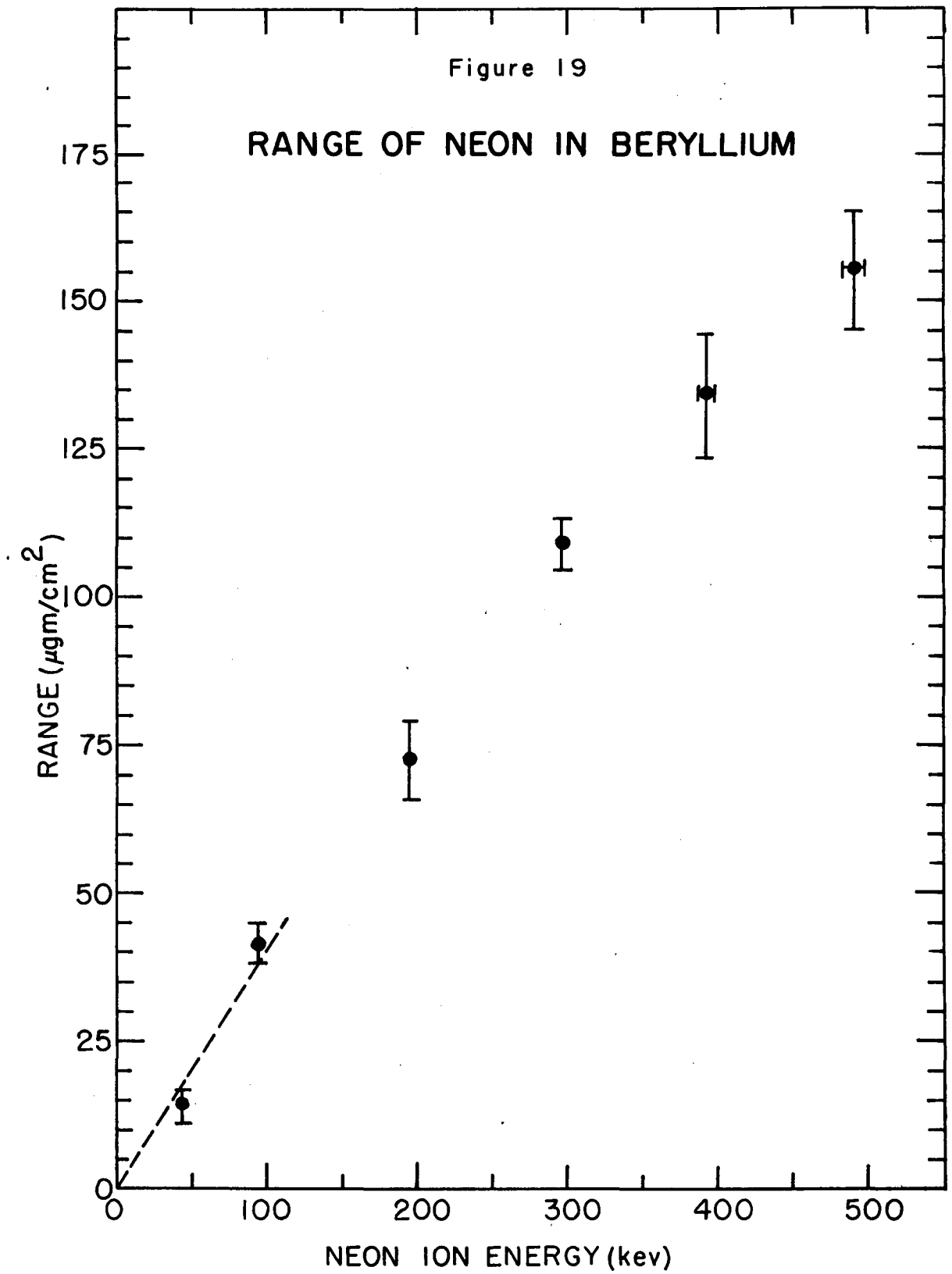
RANGE OF NEON IN BERYLLIUM
RANGE (μgm/cm²)
NEON ION ENERGY (kev)
0
25
50
75
100
125
150
175
0
100
200
300
400
500

Figures 19 - 23: The range of neon and nitrogen in various targets is plotted as a function of the ion bombarding energy. The dashed curve in each figure is the theoretical prediction of Lindhard and Scharff (Lindhard, 1961b) including electron excitation but neglecting projection correction. See p. 62, 65, text.

Figure 20

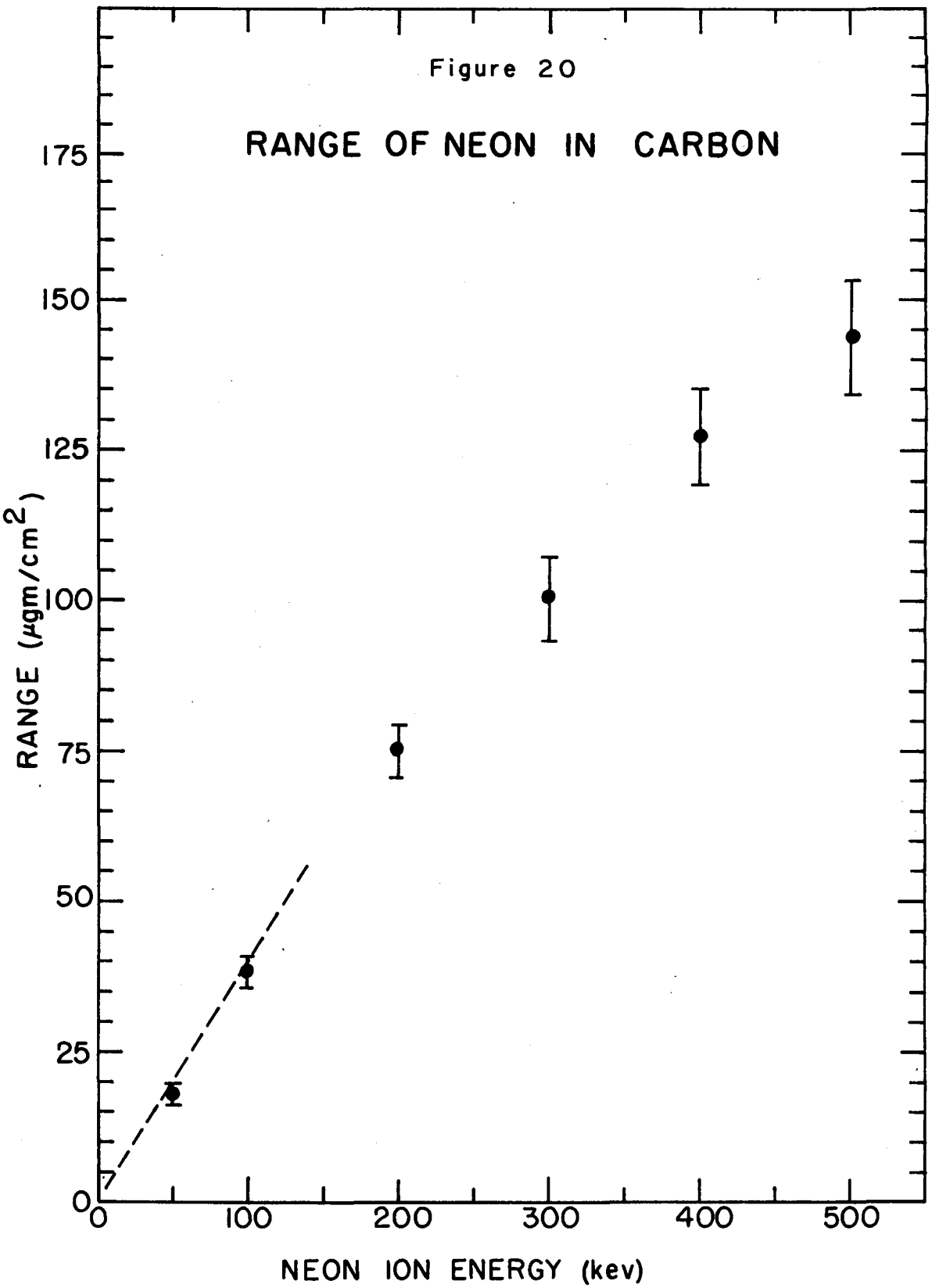
RANGE OF NEON IN CARBON
RANGE (μgm/cm²)
NEON ION ENERGY (kev)
0
25
50
75
100
125
150
175
0
100
200
300
400
500

Figure 21

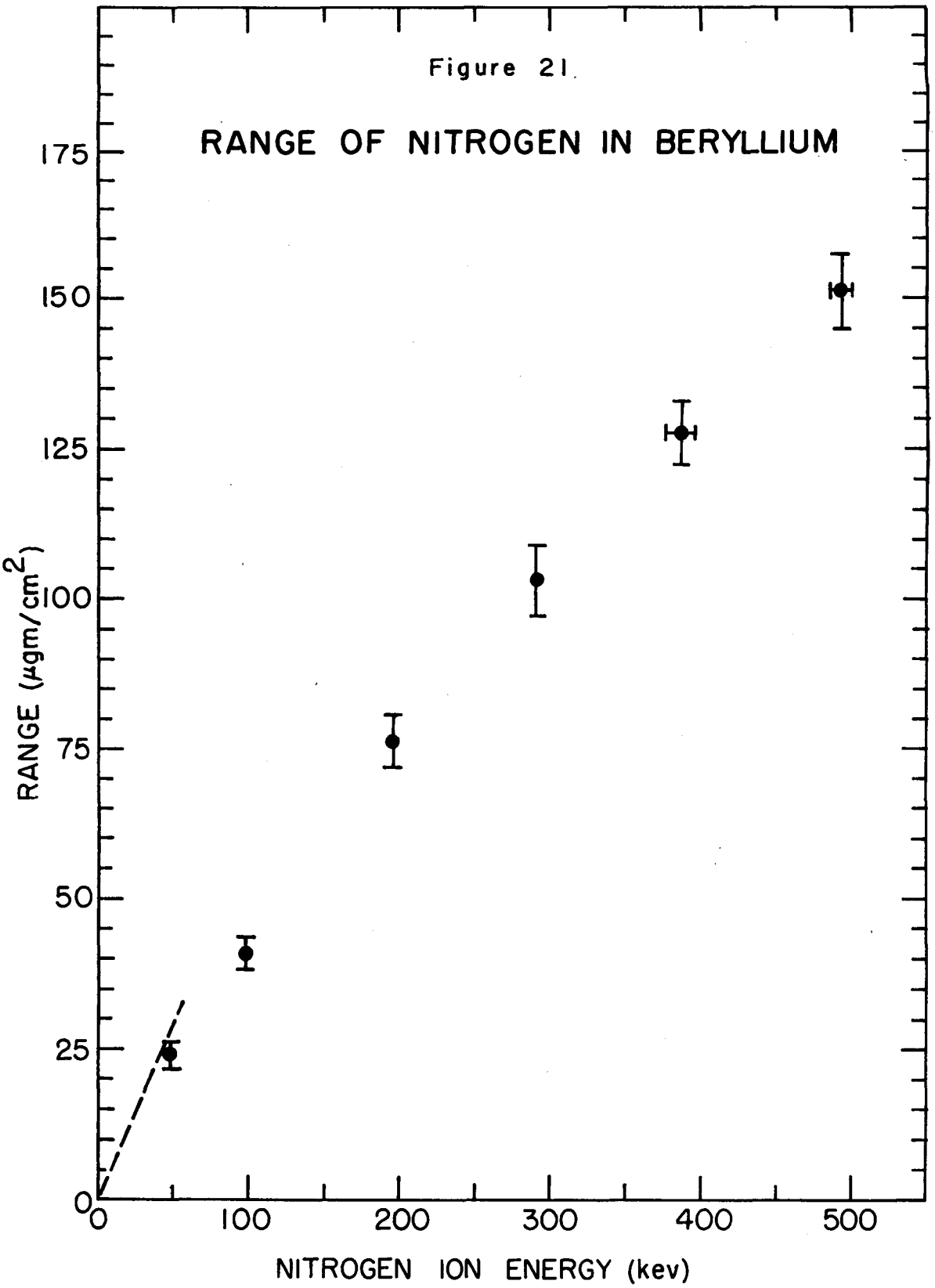
RANGE OF NITROGEN IN BERYLLIUM
RANGE (μgm/cm²)
0
25
50
75
100
125
150
175
0
100
200
300
400
500
NITROGEN ION ENERGY (kev)

Figure 22

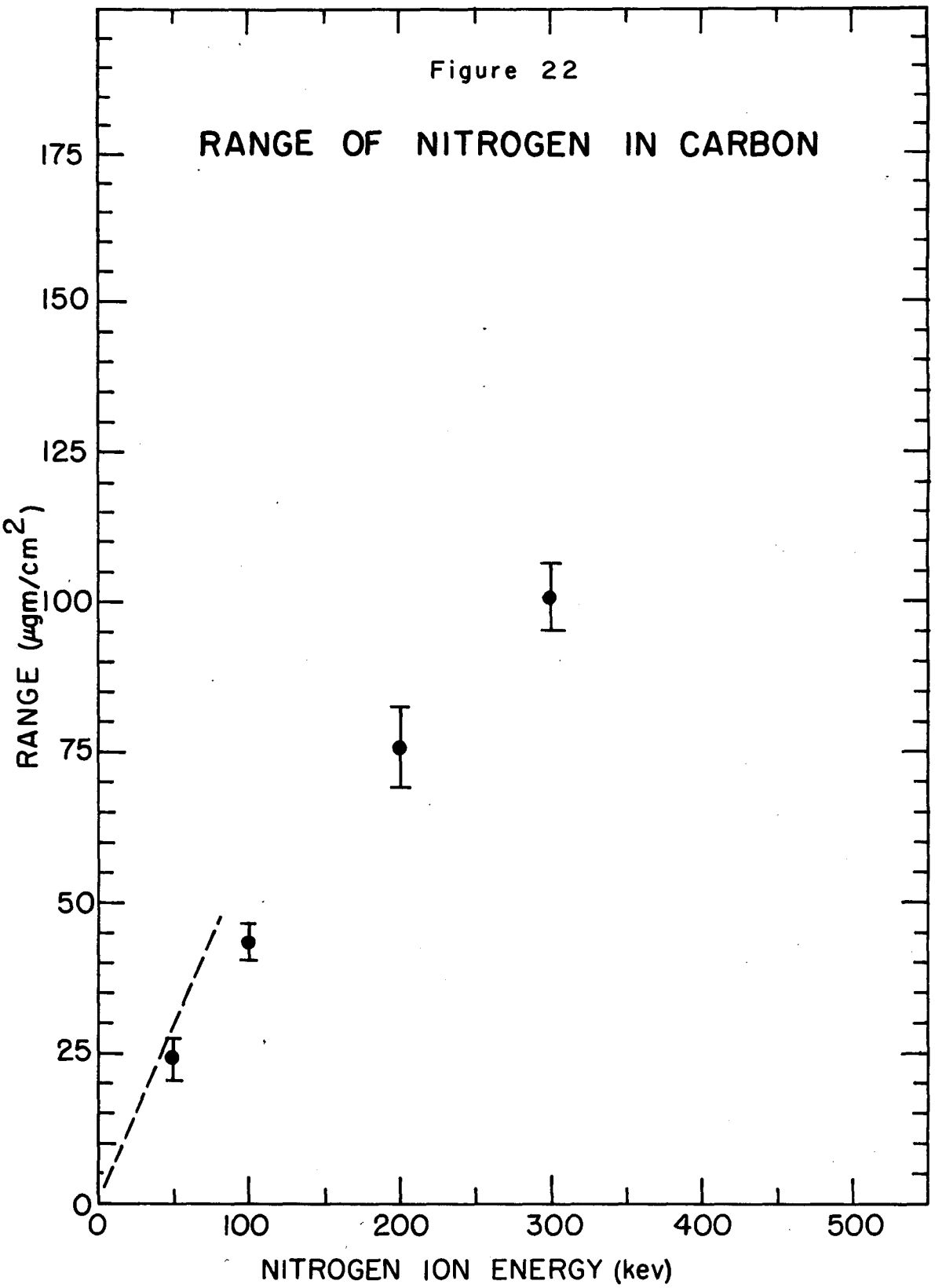
RANGE OF NITROGEN IN CARBON
RANGE (μgm/cm²)
0
25
50
75
100
125
150
175
0
100
200
300
400
500
NITROGEN ION ENERGY (kev)

Figure 23

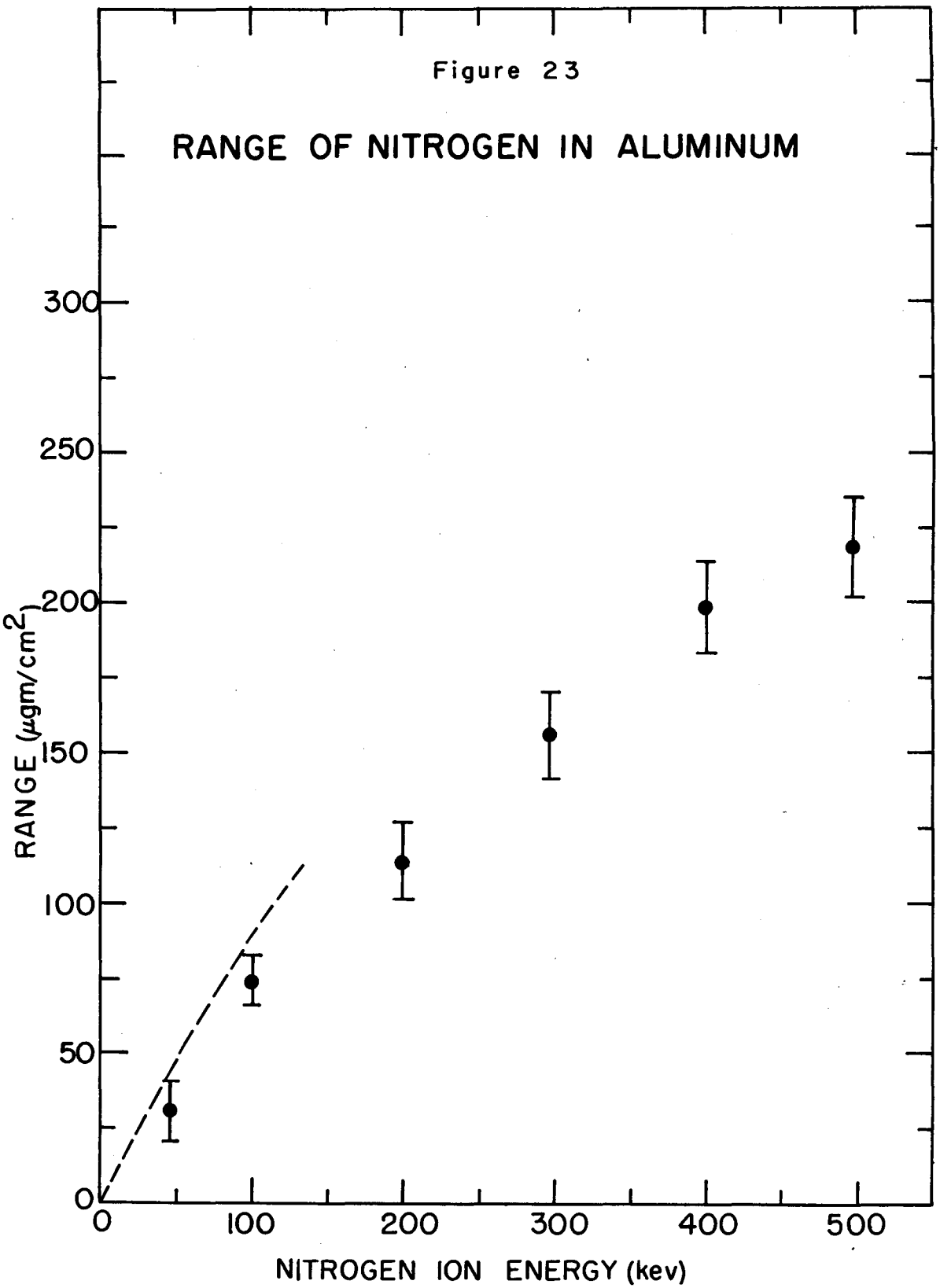
RANGE OF NITROGEN IN ALUMINUM
RANGE (μgm/cm²)
0
50
100
150
200
250
300
0
100
200
300
400
500
NITROGEN ION ENERGY (kev)

Figure 24

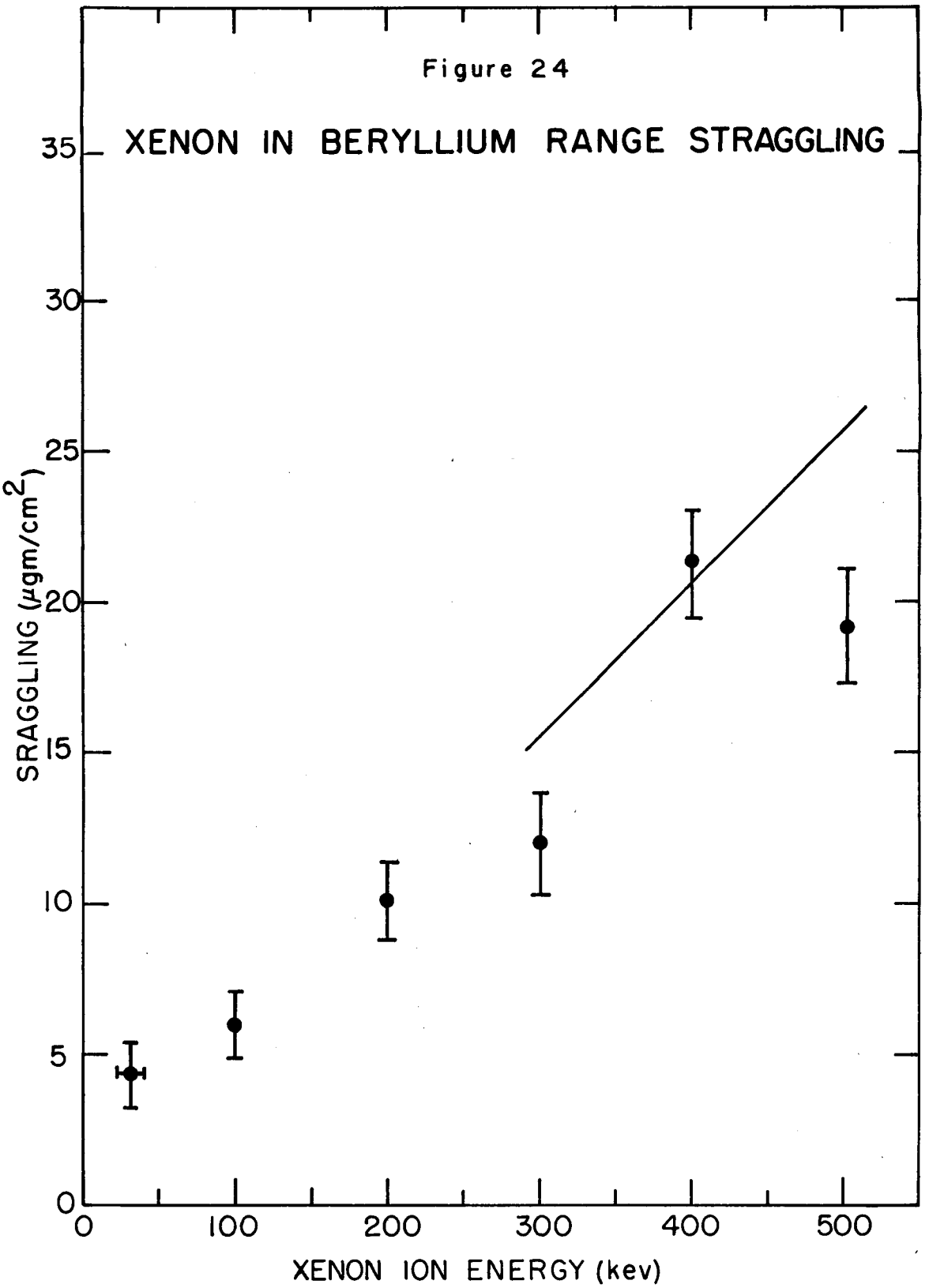
XENON IN BERYLLIUM RANGE STRAGGLING
SRAGGLING (μgm/cm²)
XENON ION ENERGY (kev)
0
5
10
15
20
25
30
35
0
100
200
300
400
500

Figures 24 - 31: Range straggling of xenon, krypton, and argon in various targets is plotted as a function of the ion bombarding energy. The solid curve in each figure represents the full width at half maximum predicted by equation 29, $2\sqrt{(2 \ln 2)\ \Omega^2(R)}$. No consideration is given for $\Omega^2(R_p)$ in terms of $\Omega^2(R)$. See p. 63, text.

Figure 25

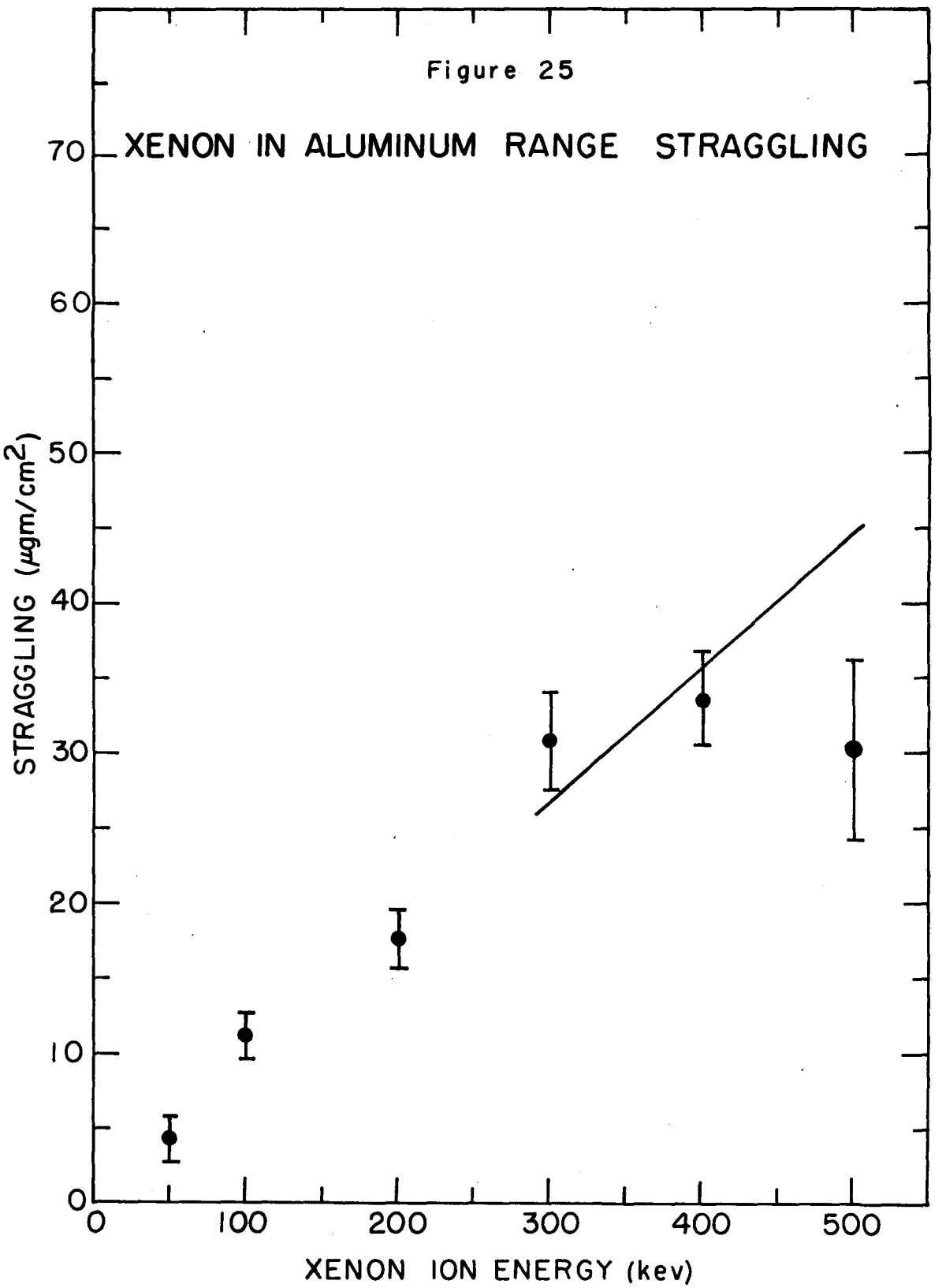
XENON IN ALUMINUM RANGE STRAGGLING
STRAGGLING (μgm/cm²)
0
10
20
30
40
50
60
70
0
100
200
300
400
500
XENON ION ENERGY (kev)

Figure 26

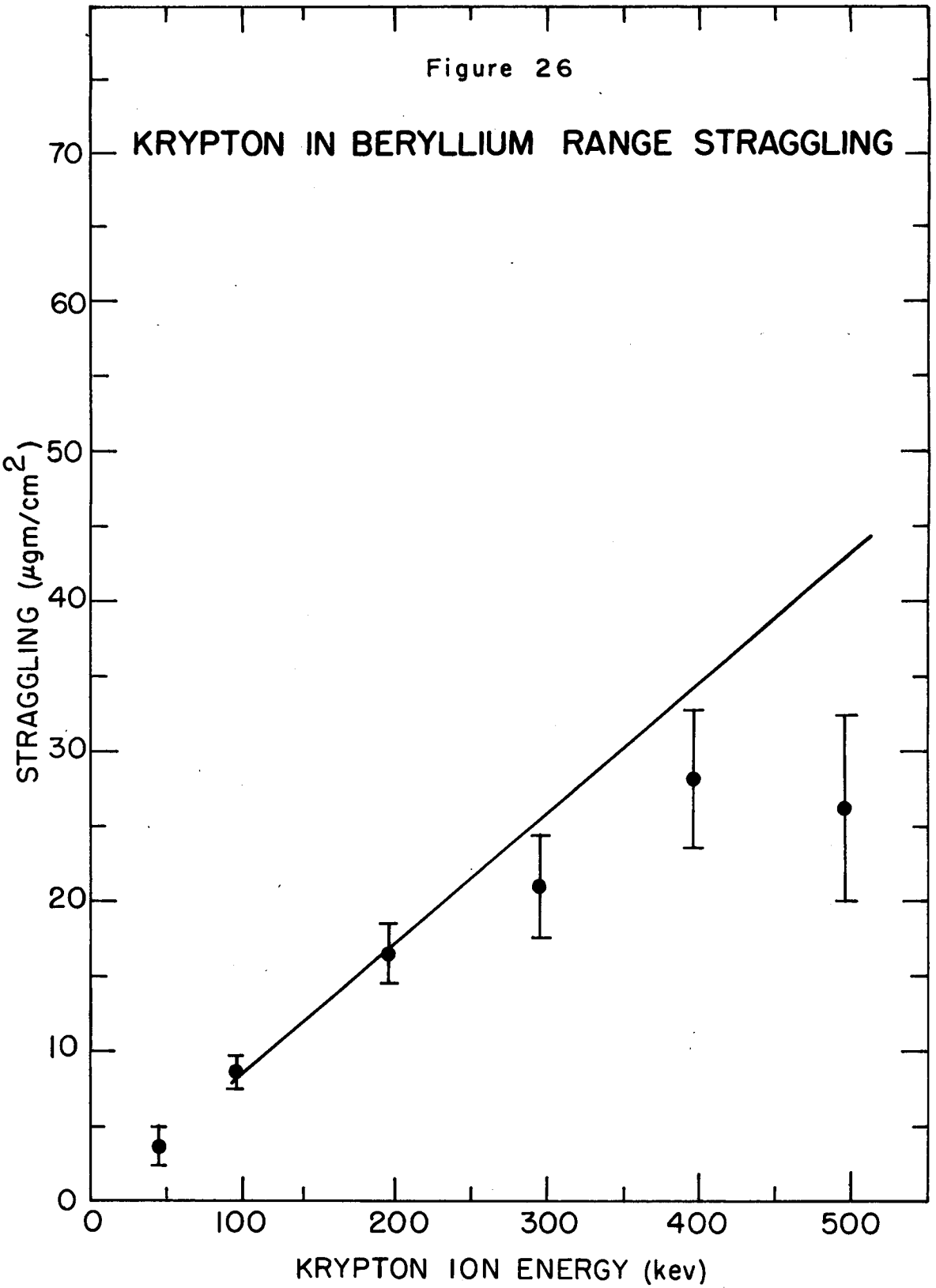
KRYPTON IN BERYLLIUM RANGE STRAGGLING
STRAGGLING (μgm/cm²)
KRYPTON ION ENERGY (kev)
0
10
20
30
40
50
60
70
0
100
200
300
400
500

Figure 27

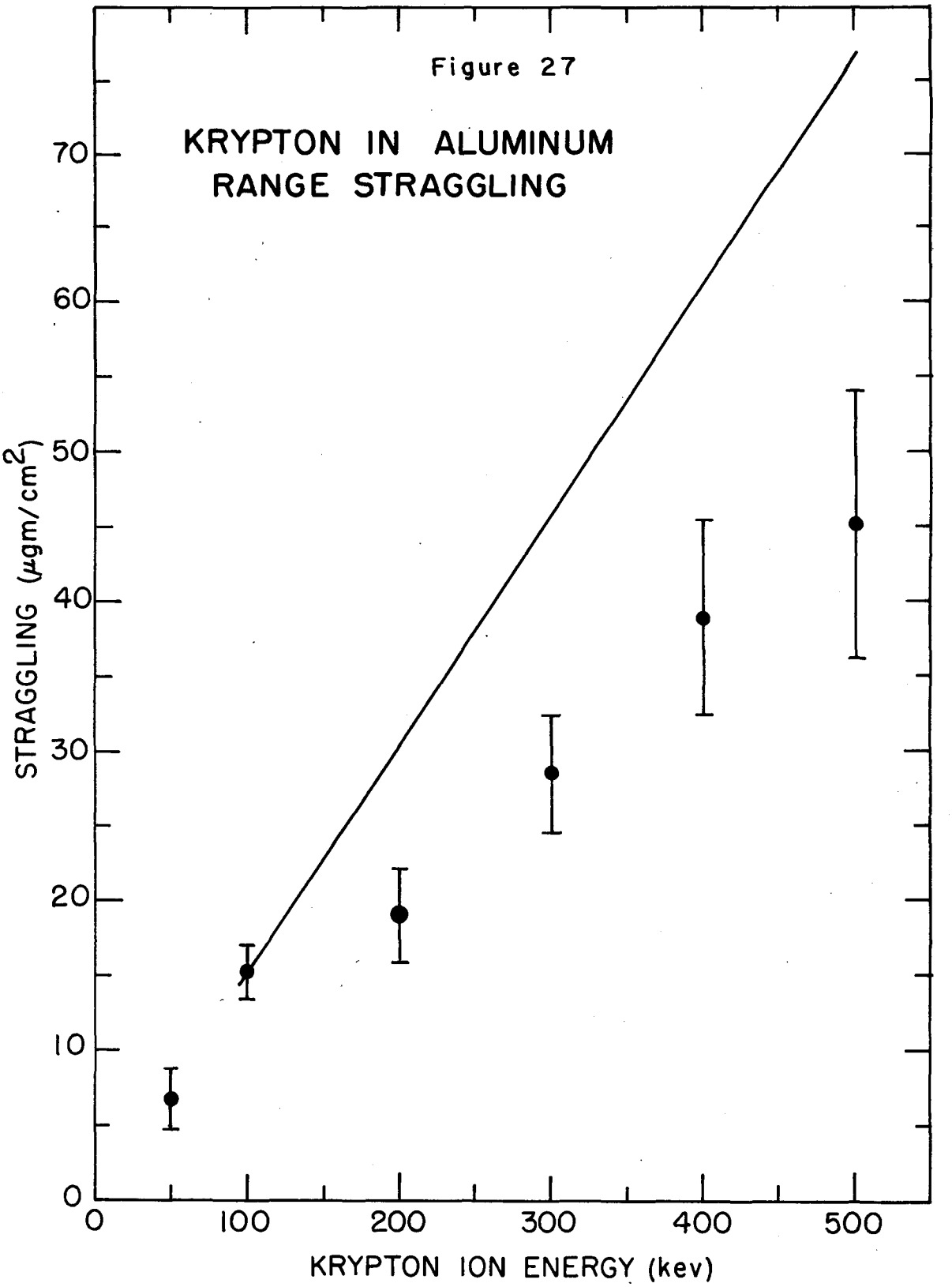
KRYPTON IN ALUMINUM
RANGE STRAGGLING
STRAGGLING (μgm/cm²)
KRYPTON ION ENERGY (kev)
0
10
20
30
40
50
60
70
0
100
200
300
400
500

Figure 28

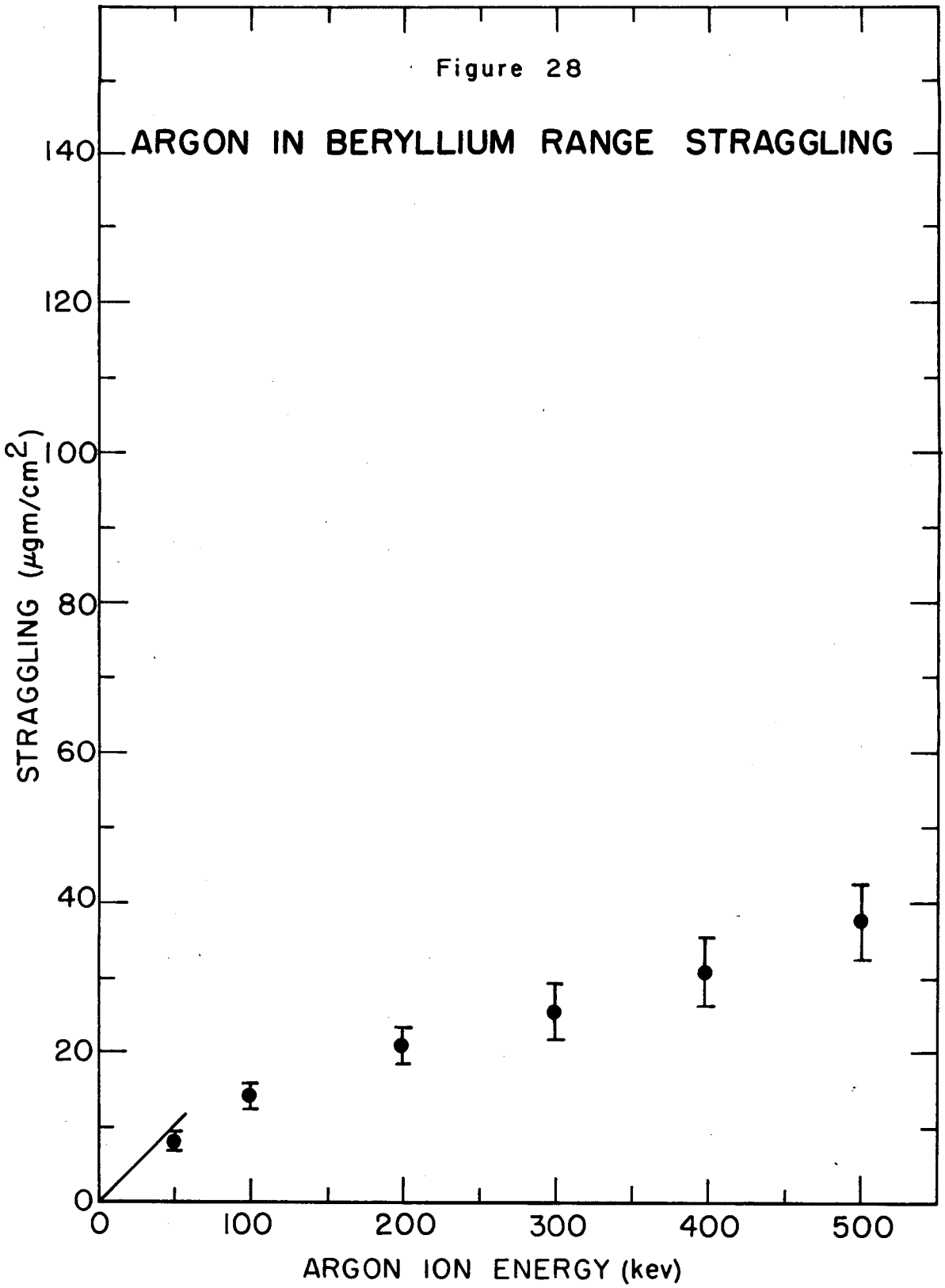
ARGON IN BERYLLIUM RANGE STRAGGLING
STRAGGLING (μgm/cm²)
0
20
40
60
80
100
120
140
0
100
200
300
400
500
ARGON ION ENERGY (kev)

Figure 29

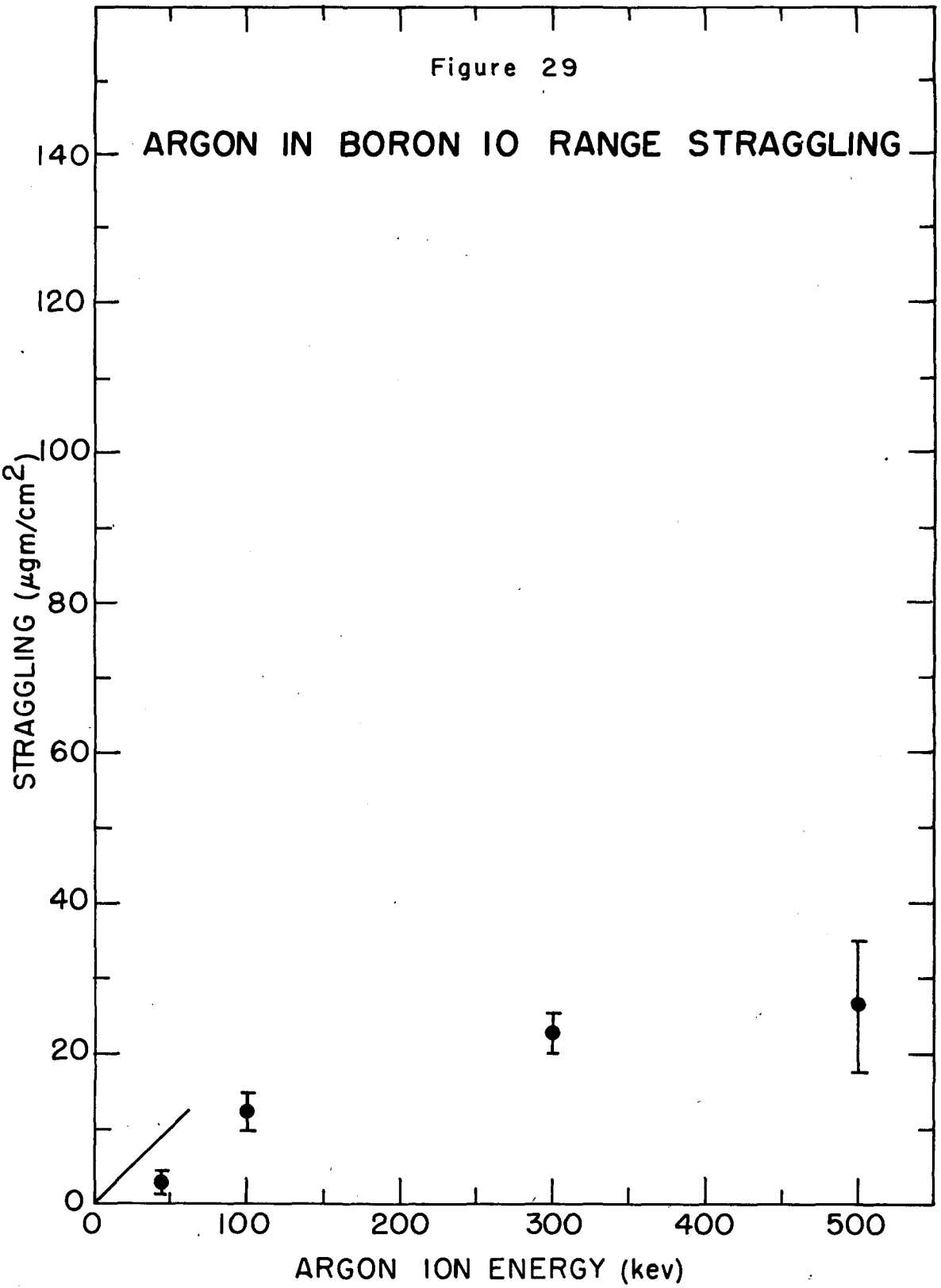
ARGON IN BORON 10 RANGE STRAGGLING
STRAGGLING (μgm/cm²)
0
20
40
60
80
100
120
140
0
100
200
300
400
500
ARGON ION ENERGY (kev)

Figure 30

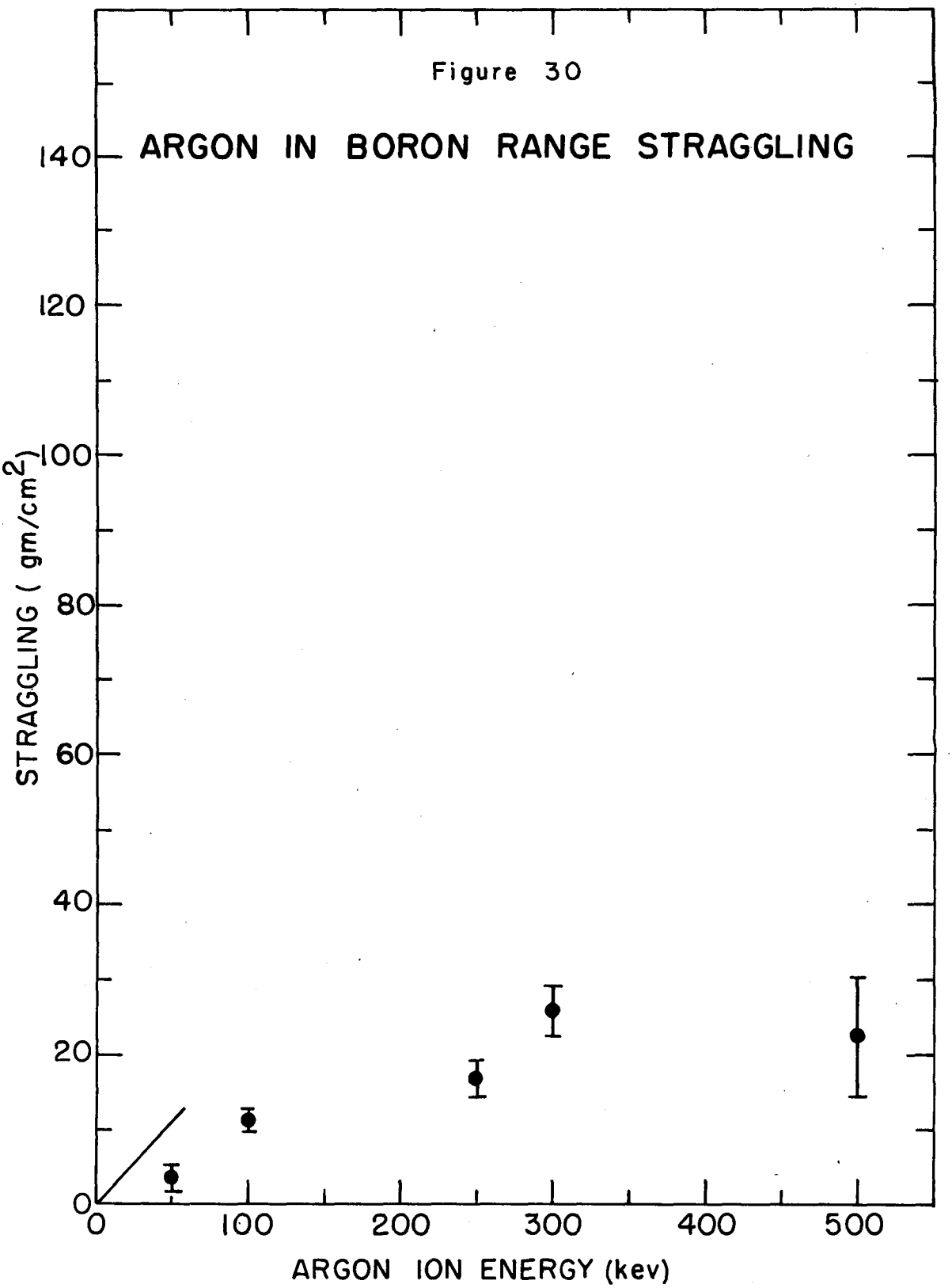
ARGON IN BORON RANGE STRAGGLING
STRAGGLING (gm/cm2)
0
20
40
60
80
100
120
140
0
100
200
300
400
500
ARGON ION ENERGY (kev)

Figure 31

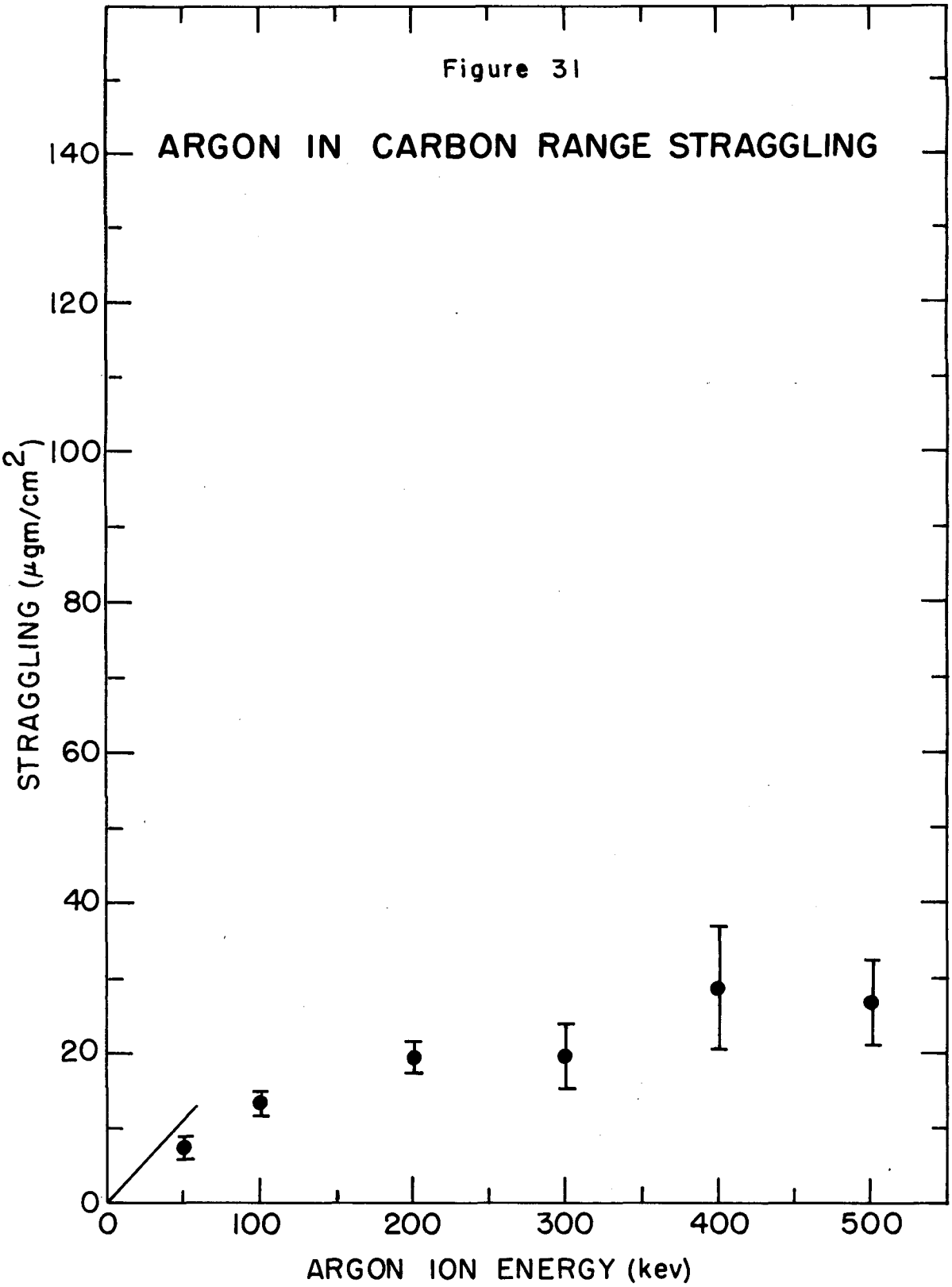
ARGON IN CARBON RANGE STRAGGLING
STRAGGLING (μgm/cm²)
0
20
40
60
80
100
120
140
0
100
200
300
400
500
ARGON ION ENERGY (kev)

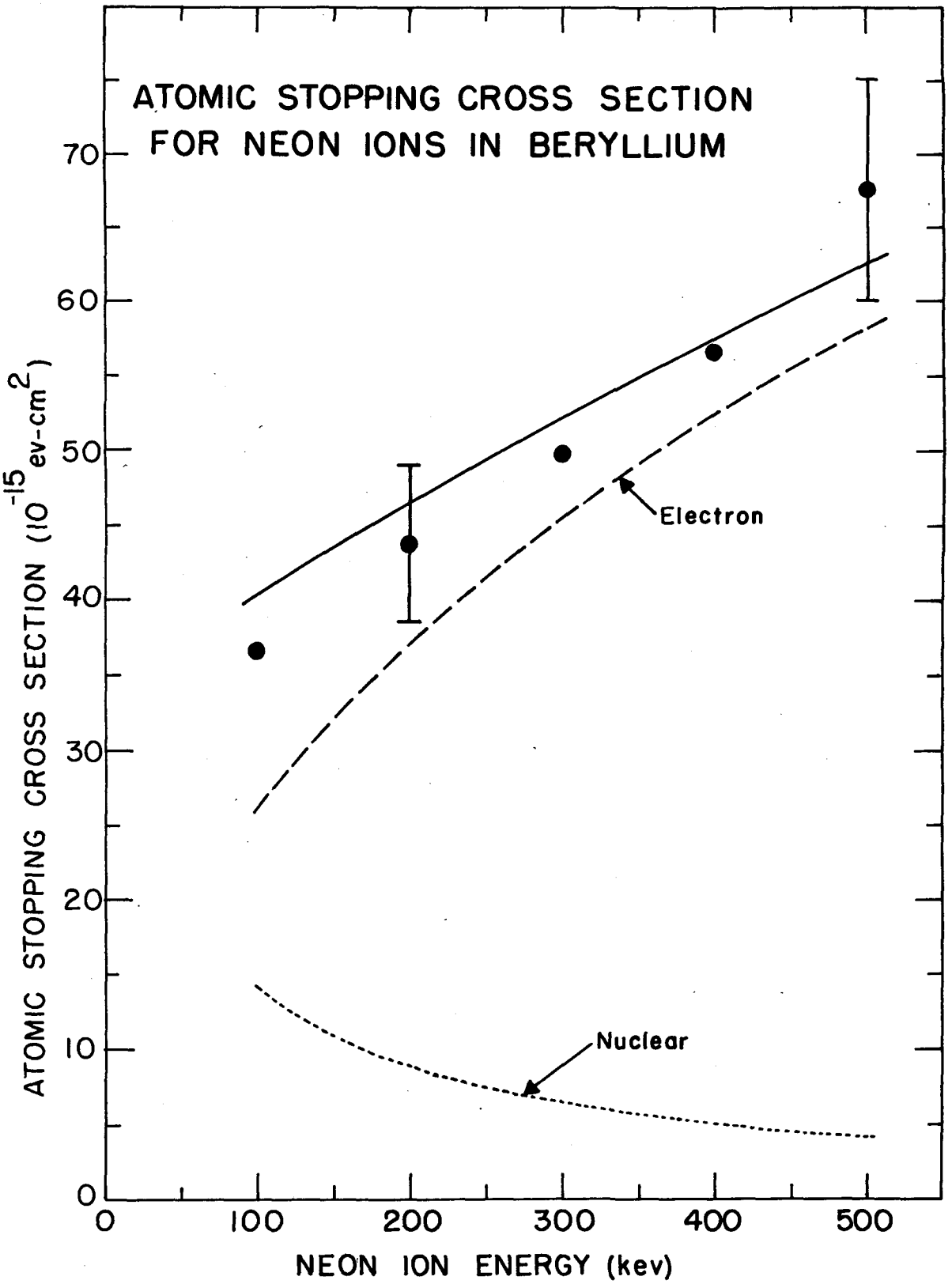
ATOMIC STOPPING CROSS SECTION
FOR NEON IONS IN BERYLLIUM
ATOMIC STOPPING CROSS SECTION (10^{-15} ev-cm^2)
NEON ION ENERGY (kev)
Electron
Nuclear
0
10
20
30
40
50
60
70
0
100
200
300
400
500

Figure 32: The dotted curve represents the contribution to the stopping cross section (dE/NdR) due to elastic nuclear collisions (equation 43, text). The dashed curve gives the contribution to the stopping cross section due to electron excitation based on Lindhard and Scharff's estimate (equation 44). The solid curve is the linear sum of these contributions, and the dark circles are the experimental points obtained by differentiating a smooth curve drawn through the points of fig. 19. See p. 65, text.

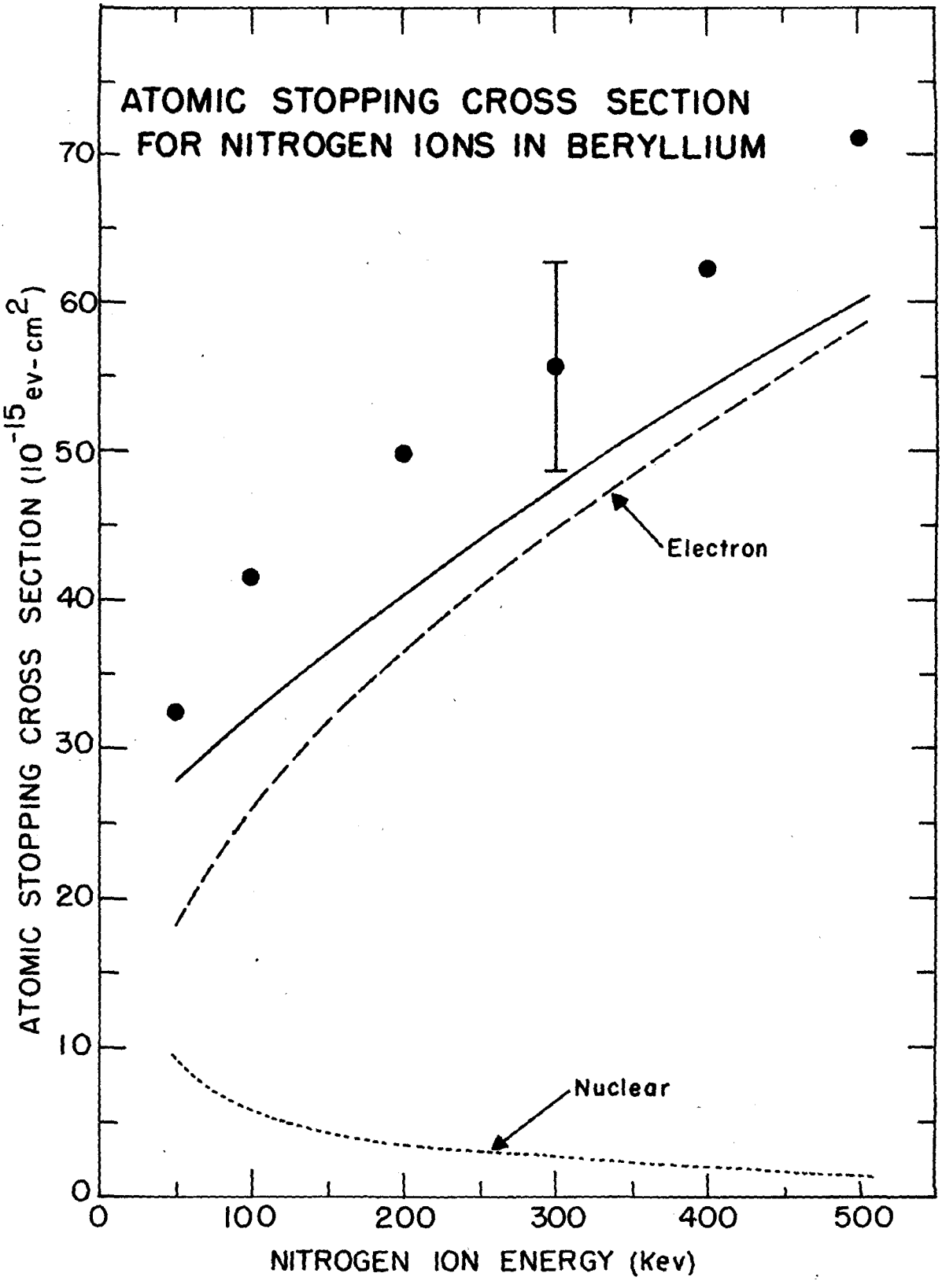
ATOMIC STOPPING CROSS SECTION
FOR NITROGEN IONS IN BERYLLIUM
ATOMIC STOPPING CROSS SECTION (10^{-15} ev-cm^2)
0
10
20
30
40
50
60
70
0
100
200
300
400
500
NITROGEN ION ENERGY (Kev)
Electron
Nuclear

Figure 33: The dotted curve represents the contribution to the stopping cross section (dE/NdR) due to elastic nuclear collisions (equation 43, text). The dashed curve gives the contribution to the stopping cross section due to electron excitation based on Lindhard and Scharff's estimate (equation 44). The solid curve is the linear sum of these contributions, and the dark circles are the experimental points obtained by differentiating a smooth curve drawn through the points of fig. 21. See p. 65, text.